Howdle, David A. (2012) *Measurement of polarisation observables using linearly polarised photons with the crystal ball at MAMI.*

PhD thesis

http://theses.gla.ac.uk/3219/

Copyright and moral rights for this thesis are retained by the author

A copy can be downloaded for personal non-commercial research or study, without prior permission or charge

This thesis cannot be reproduced or quoted extensively from without first obtaining permission in writing from the Author

The content must not be changed in any way or sold commercially in any format or medium without the formal permission of the Author

When referring to this work, full bibliographic details including the author, title, awarding institution and date of the thesis must be given

Glasgow Theses Service
http://theses.gla.ac.uk/
theses@gla.ac.uk

Measurement of Polarisation Observables using Linearly Polarised Photons with the Crystal Ball at MAMI

David A. Howdle

Presented as a Thesis for the Degree of Doctor of Philosophy

Nuclear Physics Group

School of Physics and Astronomy

University of Glasgow

© D. Howdle 2012

For Erin

Abstract

In order to further study and expand the kinematic coverage of polarisation observables in pseudoscalar meson photoproduction, a measurement of polarisation observables has been performed at the MAMI facility in Mainz, Germany. The measurement used a beam of linearly polarised photons using the coherent bremsstrahlung method and the Glasgow Tagged Photon Spectrometer. The photon beam was incident on an lH_2 target in order to produce the meson photoproduction reaction $\gamma p \rightarrow \pi^0 p$. This target was housed in the centre of the Crystal Ball detector which was used to detect the reaction products. A carbon polarimeter was used to measure the polarisation of the recoiling proton through secondary scattering. The polarisation observables for pseudoscalar meson photoproduction which were measured included: Σ, the modulation induced in the reaction products by the linearly polarised photon beam; O_x, the transfer of linear polarisation from the beam to the recoiling proton; and T, the polarisation inherent in the target proton. These measurements were performed over a wide kinematic range in both photon energy and polar angle in the centre of mass system, and were compared to three partial wave analyses, SAID, MAID and Bonn-Gatchina. The results contribute to the ongoing search for a complete understanding of the nucleon's excitation spectrum, and significantly enhance the world dataset for these polarisation observables.

Declaration

The work in this thesis is based on research carried out at the Nuclear Physics Experimental Research Group, School of Physics & Astronomy, University of Glasgow, Scotland. No part of this thesis has been submitted elsewhere for any other degree or qualification and it is all my own work unless referenced to the contrary in the text.

David A. Howdle

December 2011

Acknowledgements

There are so many people to thank that it would not be possible to include everyone here, so I will start by thanking the NPE group for the time I have spent here. In particular I would like to thank Dr. Ken Livingston and Dr. Douglas MacGregor for their supervision. I would also like to thank Prof. Guenther Rosner and Prof. Dave Ireland for their roll in having me in the group. I would also thank Dr. Derek Glazier and Dr. Dan Watts for giving me the chance to have such an interesting thesis.

From the students, I would like to make special mention of my comrade Stuart "Monkey" Fegan who struggled along with me through the years of the PhD. In addition, I extend thanks to the Mainzers, in particular Jamie Robinson and Tom Jude. I give special thanks to Mark "BigDood" Sikora and Joe "Mr. Pepe" Mancell who I work alongside closely.

I thank my fiancé Erin whom helped my through final dark hours of the thesis, and I hope I can do the same for her. I also thank the rest of my family for their tolerance and support.

Finally, there are two acknowledgements that this thesis would incomplete without. First of all, Dr. David "Magnum" Hamilton, whose help on my work was outstanding, and without it this thesis would never have happened. Secondly I would like to thank The Three Judges, where the Var Vikings were born, and its bar staff who supported David and myself in drinking extremely irresponsibly on many of the nights of my PhD.

Thank you all.

Contents

List of Figures

List of Tables

Chapter 1

Introduction

The work in this thesis presents an analysis of the beam polarisation observable Σ and a preliminary measurement of the beam-recoil double plolarisation observable O_x on the reaction $\gamma p \rightarrow \pi^0 p$. The analysis of the beam-recoil observable also allowed the extraction of the target polarisation observable T, using a new method of extraction via secondary scattering. This chapter will discuss the motivation behind the measurement of these polarisation observables and introduce the background concepts associated with this process.

1.1 Motivation

The characterisation of nucleon resonances, in particular the measurement of their masses and quantum numbers is important for the constraint of models that are concerned with nucleon structure. Different quark models based on the degrees of freedom within the nucleon predict differing sets of resonant states of the nucleon. For example, in the symmetric quark model, a large number of resonant states appear from calculations that have yet to be observed or thoroughly measured. This becomes a problem when establishing robust calculations as to how quarks interact within the nucleon.

While studies of higher mass meson photoproduction are currently underway, no-

tably so with the exploration of the N^* program at the Jefferson Laboratory in Virginia [1] (especially with the study of reactions involving $K\Lambda$ and $K\Sigma$ final states), it is important to gain further insight into the studies of the π meson photoproduction states. As described in section 1.1.4 sixteen polarisation observables in pseudoscalar meson production are defined from the helicity amplitudes which describe this process. It is clear from figure 1.1 that resonances are broad and over lapping and cross section measurements alone are not sufficient to disentangle the contributions to these resonances. A far greater sensitivity can be gained by measuring the polarisation observables [2]. In recent years, an effort to measure the double-polarisation states has been underway, and an ongoing mapping of the single observables is crucial, especially at lower energies.

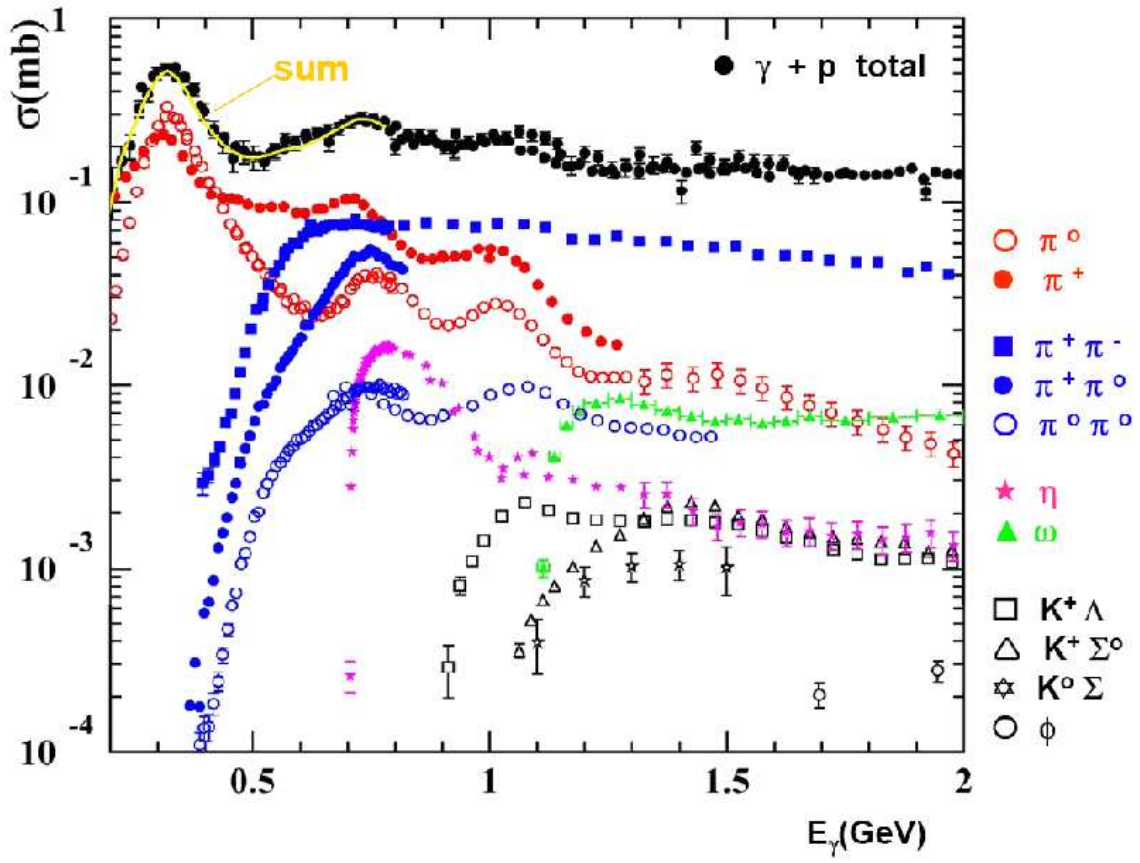

Figure 1.1: The photoproduction cross-section on the proton from $200 < E_\gamma < 2000$ MeV. Resonant structures can be seen over a wide range of energies, however several regions are unclear due to broad overlapping resonances in the total cross-section [3].

With the MAMI-C facility (Section 3.1) it is possible to measure with high statistics

the single beam polarisation observable Σ, which has not been previously measured to high statistical accuracy, or with such a broad kinematic coverage in this energy range. It is also possible to make a first preliminary measurement with a new analysis technique and a carbon recoil polarimeter to make a preliminary study of the beam-recoil observable O_x. With the addition of beam-target asymmetries, it will be possible to measure four single and eight double observables and provide constraints on the helicity amplitudes.

1.1.1 Quantum Chromodynamics

Hadron spectroscopy is a very important tool in the exploration of the nature of strongly interacting particles. These strong interactions are described by the theoretical model of Quantum Chromodynamics (QCD). QCD theorizes colour charge of the quarks, broken into six unique flavors: up, down, strange, charm, top and bottom. QCD describes the strong interaction in the Standard Model of Particle Physics [4], and gives a range of particles built up by different combinations of colour charged quarks. These particles are known as hadrons. QCD also accounts for numerous hadronic states arising from the various quantum numbers introduced into the Standard Model.

Attempts to organize the various hadronic states into sets based on new quantum numbers and symmetries gave rise to the so called "Eightfold Way", coined so by Gell-Mann and Ne'eman [5]. The Eightfold Way organized baryons of similar masses by order of the charge and strangeness quantum numbers. Figure 1.2 shows graphically this organization, and figure 1.3 shows the higher order spin baryons. The Eightfold Way eventually led to the prediction of the Ω^- baryon, which was subsequently discovered in 1964 [6]. The discovery of this baryon with three strange quarks showed the success of the Eightfold Way, and an excellent consolidation of experimental observation and theoretical prediction. With the formation of new hadrons, it was proposed that they were not in fact fundamental particles but rather built out of fundamental particles, named quarks. Initially it was thought that there were three possible flavors of quark: up, down and strange. Further development of

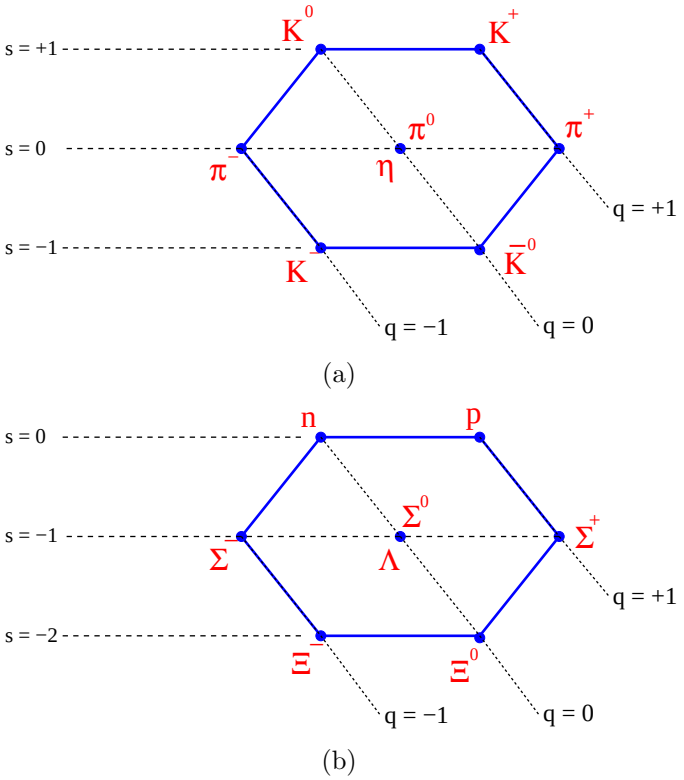

Figure 1.2: (a) The meson octet showing the grouping of pseudoscalar mesons with respect to their charge and strangeness quantum numbers and similarly (b) the baryon octet of spin-$\frac{1}{2}$ baryons.

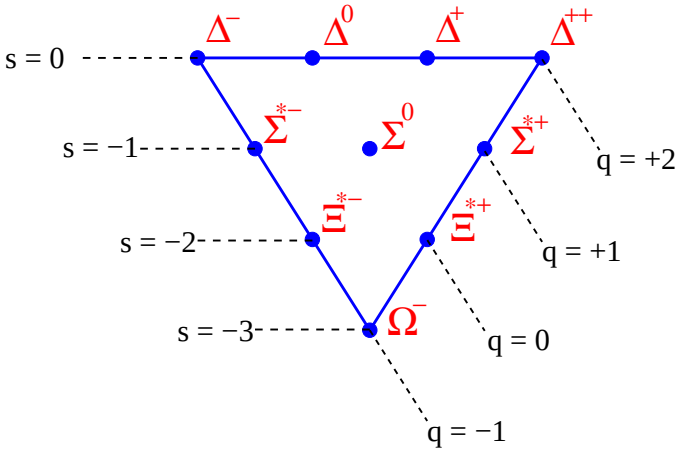

Figure 1.3: The baryon decuplet showing spin-$\frac{3}{2}$ baryons.

the model along with the experimental discovery of new hadronic states extended the description with three heavy quarks: charm, top and bottom. These conserved the quantum numbers that were used in the postulation of these hadronic states.

The introduction of the Δ^{++} caused problems with the Pauli exclusion principle,

which in terms of quarks forbids the Δ^{++} with three up quarks with parallel spins. In order to account for the existence of the Δ^{++}, a new quantum number was introduced called colour charge. Colour charge of each quark in a baryon or meson gave them a new state of either red, green or blue (as well as an associated anti-colour for anti-quarks). Following this, only colourless groups of quarks could make up a hadronic state, and as such each quark in a baryon would be made up of a unique colour charge, thus preserving the Pauli exclusion principle.

Two further notable features of QCD are colour confinement and asymptotic freedom. Individual quarks have never been experimentally observed due to colour confinement. The force between two quarks does not decrease with distance, so it is impossible to separate a quark from a nucleon without physically creating a quark-antiquark pair. Asymptotic freedom means that at higher energies the strong interaction becomes easier to calculate due to a weakening state. This is due to the decreasing of the QCD coupling constant as energy increases [7].

At high enough energies, QCD can be analogous to Quantum Electrodynamics (QED) where perturbation theory can be used to describe the interactions within the nucleon for QCD theory, much like the photon and electron describe the interactions in QED. However, QCD suffers at low energies where the perturbation approach cannot be used due to the coupling constant of QCD being close to one. There is no robust numerical solution for QCD in this non-perterbative region. Due to this, simpler models are used to support the study of nucleon excitation (Section 1.1.2). Attempts at a numerical solution of QCD at non-perterbative ranges (Lattice QCD [8,9]) have recently yielded results similar to those of the phenomenological quark models, producing similar resonance spectra. However such calculations involve unphysical high quark masses, and thus unphysical masses of well measured particles [10]. This attempt is still not robust enough to describe the baryon resonance spectrum.

1.1.2 Quark Models

At energies below ∼1 GeV QCD cannot be solved numerically [11]. As a result, simpler QCD-inspired quark models are used for the prediction of baryon resonant states. These quark models simplify the nucleon to three valence quarks in order to describe the resonance spectrum. These quarks are the effective degrees of freedom used to predict the possible excited states of the baryon (Figure 1.4).

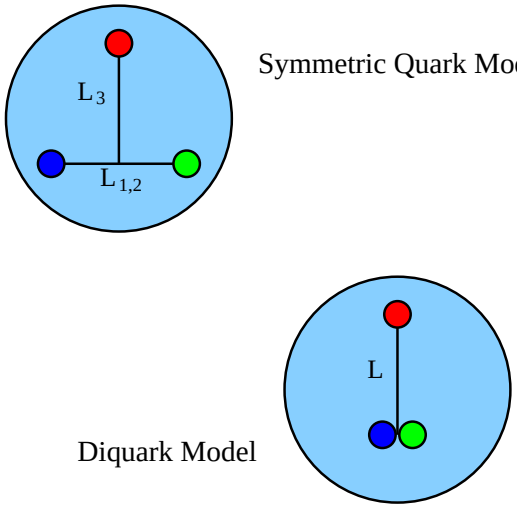

Figure 1.4: Graphical representations of both the Symmetric Quark Model (top) and the Diquark Model (bottom)

A symmetric approach where there are three bound quarks predicts a multitude of states not yet observed experimentally. This was dubbed the "Missing Resonance" problem (Section 1.1.3). Resonances are rated by the Particle Data Group [12] with a number of stars based on how well they have been observed experimentally, with table 1.1 showing their ratings (four stars denotes a well measured resonance). It is clear that many predicted resonances have little or no experimental evidence, denoted below two stars.

Another approach is made with the coupling of two of the valence quarks into a diquark system, called the diquark model [13]. This tighter bound system predicts far fewer states than its symmetric counter part, and thus fewer poorly, or unobserved resonance states. The diquark model could be seen as more concise as the symmetric quark model predicts more poorly experimentally observed states. However,

evidence from partial-wave analysis [14] suggests that there may not be sufficient force between quarks to form the diquark. On top of this, new experimental findings suggest the presence of a missing resonant state of the nucleon [15] predicted by the symmetric quark model, but not expected form the diquark model.

1.1.3 Missing Resonances

There is currently a worldwide effort into solving what is known as the "Missing Resonance Problem", including laboratories at Mainz, Bonn and notably the Jefferson Lab N^* programme [1]. Table 1.1 shows the status of resonances rated by the Particle Data Group. These have a star rating based on their observation in experiment, rating from four stars signifying a resonance that has been measured at multiple laboratories and is considered well understood to one or no stars indicating little to no experimental finding of the predicted resonance.

Most of the world data on baryon resonances is from πN scattering, and does not show many missing predicted states [16]. As such, the use of newer more sensitive methods of searching for missing resonances is required. Meson photoproduction provides a new valuable tool for the field of both polarisation observables and missing resonances. The use of an electromagnetic probe over that of a hadronic probe is beneficial, as it is based on the well understood process of QED. In addition to this, it gives access to polarized probes which in turn can access polarisation information and provide more insight and sensitivity to resonances. This is the proposed method with which to resolve the "Missing Resonance Problem" [2]

While the work presented in the thesis is in the first resonance region, and there are no predicted missing states at the energy of the $\Delta(1232)$ and $N(1440)$ (Table 1.1), it is important to map the polarisation observables at all energies and supply a more complete picture.

N^*	L_{2J2I}	Status	Δ^*	L_{2J2I}	Status
p	P_{11}	****	$\Delta(1232)$	P_{33}	****
n	P_{11}	****	$\Delta(1600)$	P_{33}	***
$N(1440)$	P_{11}	****	$\Delta(1620)$	S_{31}	****
$N(1520)$	D_{13}	****	$\Delta(1700)$	D_{33}	****
$N(1535)$	S_{11}	****	$\Delta(1750)$	P_{31}	*
$N(1650)$	S_{11}	****	$\Delta(1900)$	S_{31}	**
$N(1675)$	D_{15}	****	$\Delta(1905)$	F_{35}	****
$N(1680)$	F_{15}	****	$\Delta(1910)$	P_{31}	****
$N(1700)$	D_{13}	***	$\Delta(1920)$	P_{33}	***
$N(1710)$	P_{11}	***	$\Delta(1930)$	D_{35}	***
$N(1880)$	P_{11}				
$N(1975)$	P_{11}				
$N(1720)$	P_{13}	****	$\Delta(1940)$	D_{33}	*
$N(1900)$	P_{13}	**	$\Delta(1950)$	F_{37}	****
$N(1910)$	P_{13}		$\Delta(1950)$	P_{33}	
$N(1900)$	F_{15}	***	$\Delta(2000)$	F_{35}	**
$N(1990)$	F_{17}	**	$\Delta(2150)$	S_{31}	*
$N(2080)$	D_{13}	**	$\Delta(2200)$	G_{37}	*
$N(2090)$	S_{11}	*	$\Delta(2300)$	H_{39}	**
$N(2100)$	P_{11}	*	$\Delta(2350)$	D_{35}	*
$N(2190)$	G_{17}	****	$\Delta(2390)$	F_{37}	*
$N(2200)$	D_{15}	**	$\Delta(2400)$	G_{39}	**
$N(2220)$	H_{19}	****	$\Delta(2420)$	$H_{3,11}$	****
$N(2250)$	G_{19}	****	$\Delta(2750)$	$I_{3,13}$	**
$N(2600)$	$I_{1,11}$	***	$\Delta(2950)$	$K_{3,15}$	**
$N(2700)$	$K_{1,13}$	**			

Table 1.1: The Particle Data Group resonance table [12]. Showing the N^* and Δ^* states

1.1.4 Polarisation Observables in Meson Photoproduction

Meson photoproduction is governed by the electromagnetic interaction, which is a well understood process. This makes it ideal for the study of nucleon excitations. In this thesis, the mechanism in which a photon probes a nucleon into a resonant state, which then decays into a nucleon-meson pair is of most interest. There is however an associated set of background mechanisms, which will be introduced here, and accounted for later in chapter 6.

Four helicity amplitudes arise from the helicity states of the nucleon and the photon, S_1, S_2, N and D. These correspond to two single, one non and one double helicity

spin-flip state respectively [17]. The differential cross-section can be given from these four helicity amplitudes:

$$\frac{d\sigma}{d\Omega} = |S_1|^2 + |S_2|^2 + |D|^2 + |N|^2 \tag{1.1}$$

Additionally, four transversity amplitudes, b_1, b_2, b_3 and b_4, can be expressed as combinations of the helicity amplitudes:

$$\begin{aligned} b_1 &= \frac{1}{2}[(S_1 + S_2) + i(N - D)], \qquad b_2 = \frac{1}{2}[(S_1 + S_2) - i(N - D)], \\ b_3 &= \frac{1}{2}[(S_1 - S_2) - i(N + D)], \qquad b_4 = \frac{1}{2}[(S_1 - S_2) + i(N + D)] \end{aligned} \tag{1.2}$$

Taking combinations of these amplitudes and their complex conjugates gives sixteen possible quantities. These quantities are all real and measurable. These are the sixteen observables, divided into four categories; single observables, beam-target observables, beam-recoil observables and target-recoil observables. These are shown in table 1.2, with the transversity amplitude combinations and applicable polarisation states. It is worth noting that the observables in table 1.2 can also be expressed in terms of their helicity amplitude combinations.

The three single polarisation observables (not including the unpolarised cross-section in the sixteen observables) are dependent on the knowledge of either the polarisation of the beam, target, or nucleon in the final state. The three remaining groups of four require combinations of polarised beams (linear and circular), two target states (longitudinal and transverse) and the ability to determine the polarisation in the final state of the recoiling nucleon.

1.1.5 The Complete Measurement

Complete measurements in polarisation observables require a measurement of at least eight of the sixteen observables due to the non-independence of the different groups [17]. Many of these selected amplitudes must be from the three groups of double observables. This presents a significant challenge to the experimental work,

Observable	Transversity Representation	Polarisation	Observable Type
$\frac{d\sigma}{dt}$	$\|b_1\|^2 + \|b_2\|^2 + \|b_3\|^2 + \|b_4\|^2$	(0, 0, 0)	Single
Σ	$\|b_1\|^2 + \|b_2\|^2 - \|b_3\|^2 - \|b_4\|^2$	(γ_L, 0, 0)	
T	$\|b_1\|^2 - \|b_2\|^2 - \|b_3\|^2 + \|b_4\|^2$	(0, y, 0)	
P	$\|b_1\|^2 - \|b_2\|^2 + \|b_3\|^2 - \|b_4\|^2$	(0, 0, y)	
G	$2Im(b_1 b_3^* + b_2 b_4^*)$	(γ_L, z, 0)	Beam-Target
H	$-2Re(b_1 b_3^* - b_2 b_4^*)$	(γ_L, x, 0)	
E	$-2Re(b_1 b_3^* + b_2 b_4^*)$	(γ_C, z, 0)	
F	$2Im(b_1 b_3^* - b_2 b_4^*)$	(γ_C, x, 0)	
O_x	$-2Re(b_1 b_4^* - b_2 b_3^*)$	(γ_L, 0, x')	Beam-Recoil
O_z	$-2Im(b_1 b_4^* + b_2 b_3^*)$	(γ_L, 0, z')	
C_x	$2Im(b_1 b_4^* - b_2 b_3^*)$	(γ_C, 0, x')	
C_z	$-2Re(b_1 b_4^* + b_2 b_3^*)$	(γ_C, 0, z')	
T_x	$2Re(b_1 b_2^* - b_3 b_4^*)$	(0, x, x')	Target-Recoil
T_z	$2Im(b_1 b_2^* - b_3 b_4^*)$	(0, x, z')	
L_x	$2Im(b_1 b_2^* + b_3 b_4^*)$	(0, z, x')	
L_z	$2Re(b_1 b_2^* + b_3 b_4^*)$	(0, z, z')	

Table 1.2: List of the psuedoscalar meson polarisation observables with their transversity amplitude representations [17]. The notation of (γ, t, r) represents the necessary polarisation required to extract the observables, where γ is the beam, t is the target and r is the recoil

while single polarisation observables are relatively well measured (see section 2.2). In the case of the beam-recoil set, the polarisation transfer to the recoiling nucleon must be extractable. This is normally done using a secondary scattering medium after the target, which leads to large losses in efficiency. Beam-target states require a target which has a reliable and steadily held polarisation, many of which have been developed in recent years.

This thesis focuses on the measurement of the Σ observable, or beam asymmetry, from the single polarisation observable set. This is a direct measure of the polarisation induced in the system from the linearly polarised beam. However, with the presence of the recoil polarimeter in the experimental setup, it was also possible to make a preliminary measurement of the O_x observable with the MAMI setup. Details of the analysis can be found in chapters 4 and 5. Chapters 2 and 3 describe the experiments used previously for measurement of observables and the experiment used in this thesis. Chapter 6 will present and discuss the results extracted for this thesis.

Chapter 2

Model Predictions and Previous Measurements

This chapter gives a brief introduction to the most significant models used in this field, and presents previous measurements of the relevant polarisation observables from different laboratories.

2.1 Model Predictions

2.1.1 MAID model

MAID is a unitary isobar model [18], which approximates the resonant spectrum from a collection of known resonances based on the PDG [12] resonances seen in table 1.1, and selects only those with a four star rating from experimental observation. When calculations are performed certain resonances may be carefully selected to produce a calculation of any of the sixteen polarisation observables in meson photoproduction. The MAID model only considers reactions arising on pion-nucleon final states, and folds its background from t-channel mixing from meson exchange as well as coupled channels between pseudoscalar and pseudovector reactions [19]. The fitting procedure considers all chosen resonant contributions allowing MAID to

produce individual results for the overall fit with each different known contribution considered, or excluded.

2.1.2 SAID model

The SAID model, unlike the MAID isobar analysis, is a partial wave analysis which makes no assumption to the resonances present [20]. Rather than using all present resonances with four star ratings from the PDG collection, SAID is constrained based on the world data set for pion-nucleon scattering, and some meson photoproduction data. A Transition Matrix is formed with a considered background contribution on similar final states. A simplified view can be written as:

$$T_{\gamma N} = I(1 + iT_{\pi N}) + RT_{\pi N} \tag{2.1}$$

The background term, I, is taken from Born terms on pseudoscalar mesons, as well as the exchange of vector mesons at higher energies. R, the resonance term of the fit is calculated based on the momentum of the incident photon in $T_{\gamma N}$ and the pion momentum in $T_{\pi N}$. Parameters determined from this calculation are used to produce a fit of the resonant structure.

2.1.3 Bonn-Gatchina model

The Bonn-Gatchina (BoGa) model [21], similar to the SAID model, involves a partial wave analysis solution constrained to world data. However, the Bonn-Gatchina model is not entirely based on pion-nucleon scattering, but rather uses a multitude of different reaction processes, including meson photoproduction. The basis of the BoGa model is pion-nucleon scattering, mainly on the body of work produced by SAID. BoGa does consider other scattering reactions when performing their calculations, and a key difference is their selectivity in the experimental information used to constraint their fitted prediction for any particular observable and channel. Selections are made based on experimental consistency at particular angles

and energies between measurements. In particular, on the $\gamma p \to \pi^0 p$ reaction, constraints are based on select experiments from TAPS@MAMI [22], GDH-A2 [23, 24], GRAAL [25], CB-ELSA [26, 27] and CLAS [28].

2.2 Previous Measurements

In the early 1960's the $\gamma p \to \pi^0 p$ reaction was investigated mainly with cross-section measurements. Recent developments in the prediction of resonances and the use of polarised probes has led to the study of polarisation observables. Over a number of years, these observables have been studied, however there remains gaps in the fields of study, as well as only more recently the ability to study more complex observables such as those requiring the measurement of recoil polarisation and polarised targets.

2.2.1 Σ Measurements

There have been several previous measurements of Σ over a wide range of energies on the $\gamma p \to \pi^0 p$ channel, such as the measurements by Beck [29, 30] at low energies ($240 < E_\gamma < 440$ MeV) with good kinematic coverage using the Crystal Ball, as well as Elsner and Sparks [31, 32] at higher energies ($767 < E_\gamma < 1680$ MeV) with the Bonn setup. The GRAAL and Yerevan measurements [25, 33] also cover high energies with good kinematic coverage (with respect to the measurement presented in this thesis), and overlap with the energy range for Σ presented in this thesis.

The Yerevan Measurement

The Yerevan synchrotron facility was a *bremsstrahlung* experimental facility [33]. The facility used the Yerevan spectrometer setup in order to detect charged and neutral particles from reactions of $500 < E_\gamma < 1075$ MeV. The coherent *bremsstrahlung* beam was generated via the scattering of an electron beam from the Yerevan synchrotron on a diamond radiator, similar to that discussed a later section 3.2.1.

This produced a high luminosity photon beam, however the degree of the linear polarisation is more complicated to determine compared to that of a Compton back-scattering beam, such as used in the GRAAL experiment. The Yerevan Spectrometer consisted of a magnetic spectrometer, tracking chambers and a Čerenkov detector in order to separate final state particles. The measurement of the Σ observable at Yerevan was early in the development of polarisation observables. The facility measured a relatively large range of energies over a good kinematic range ($85^\circ < \theta^{\pi_0}_{CM} < 125^\circ$). The results of the Yerevan measurement are shown in figures 2.1, 2.2 and 2.3.

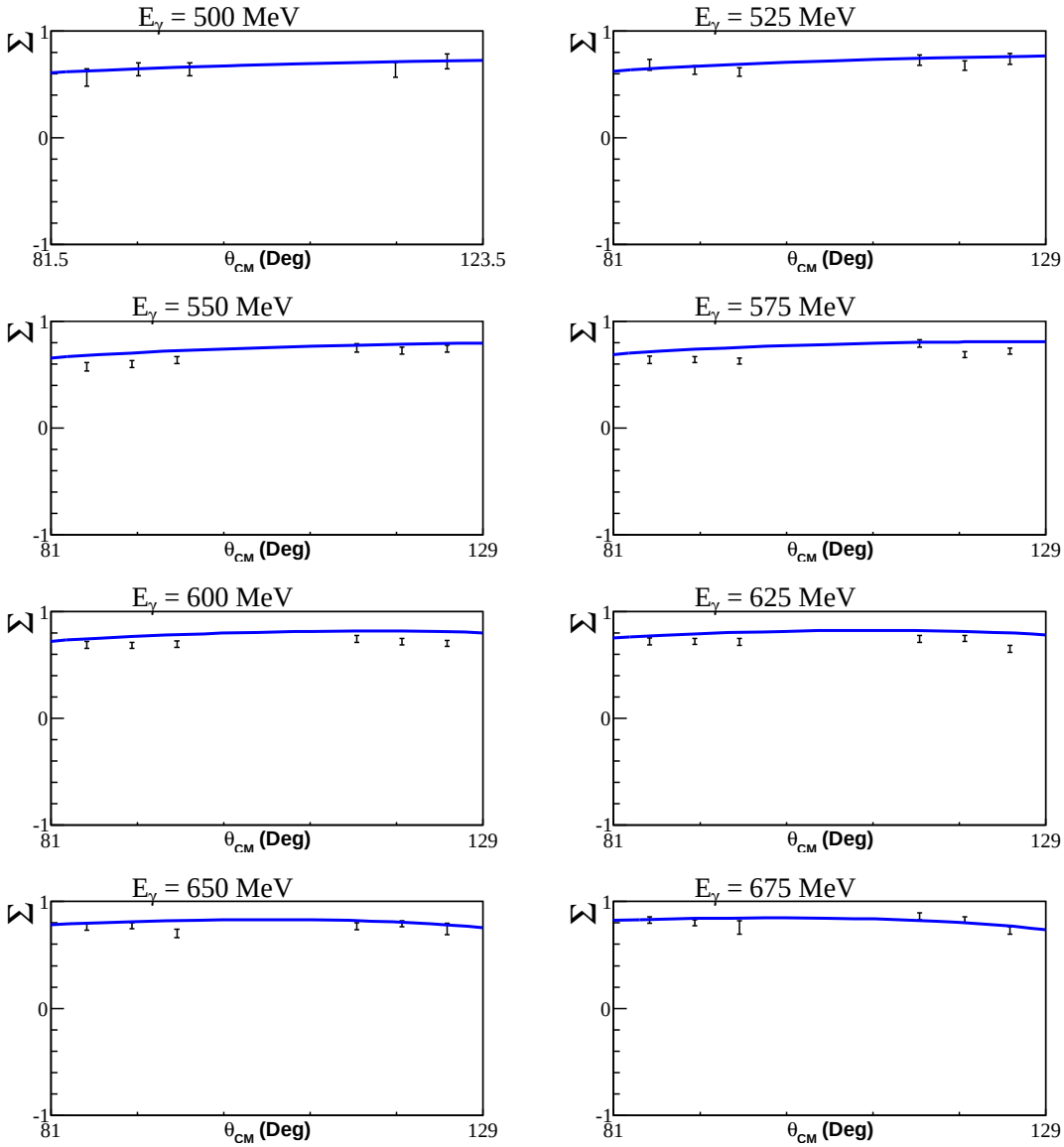

Figure 2.1: Measurement of the Σ observable performed at the Yerevan Synchrotron for $500 < E_\gamma < 675$ MeV. The blue line shows the SAID model prediction. The θ angles are from the π^0 in the centre of mass.

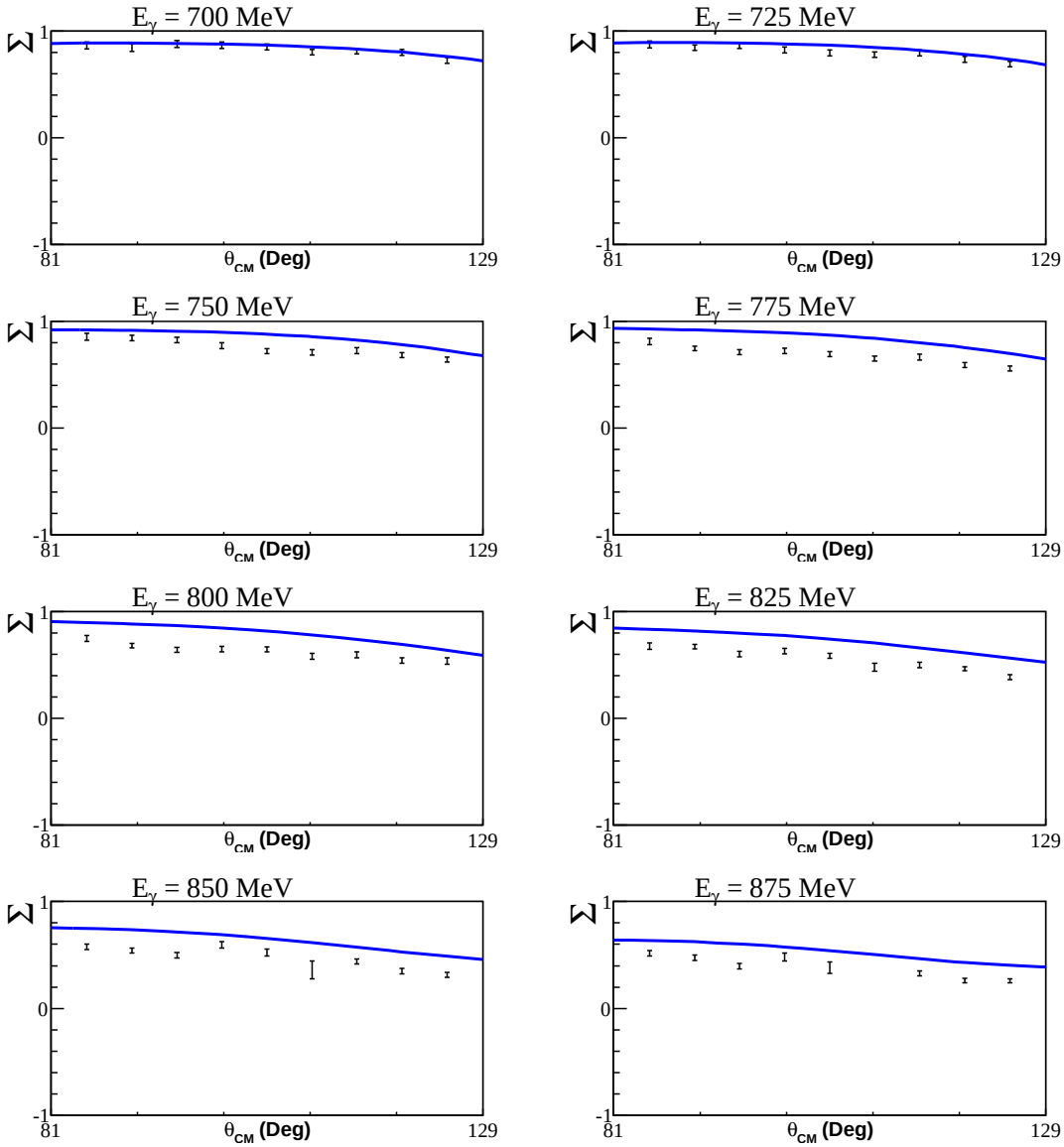

Figure 2.2: Measurement of the Σ observable performed at the Yerevan Synchrotron for $700 < E_\gamma < 875$ MeV. The blue line shows the SAID model prediction. The θ angles are from the π^0 in the centre of mass.

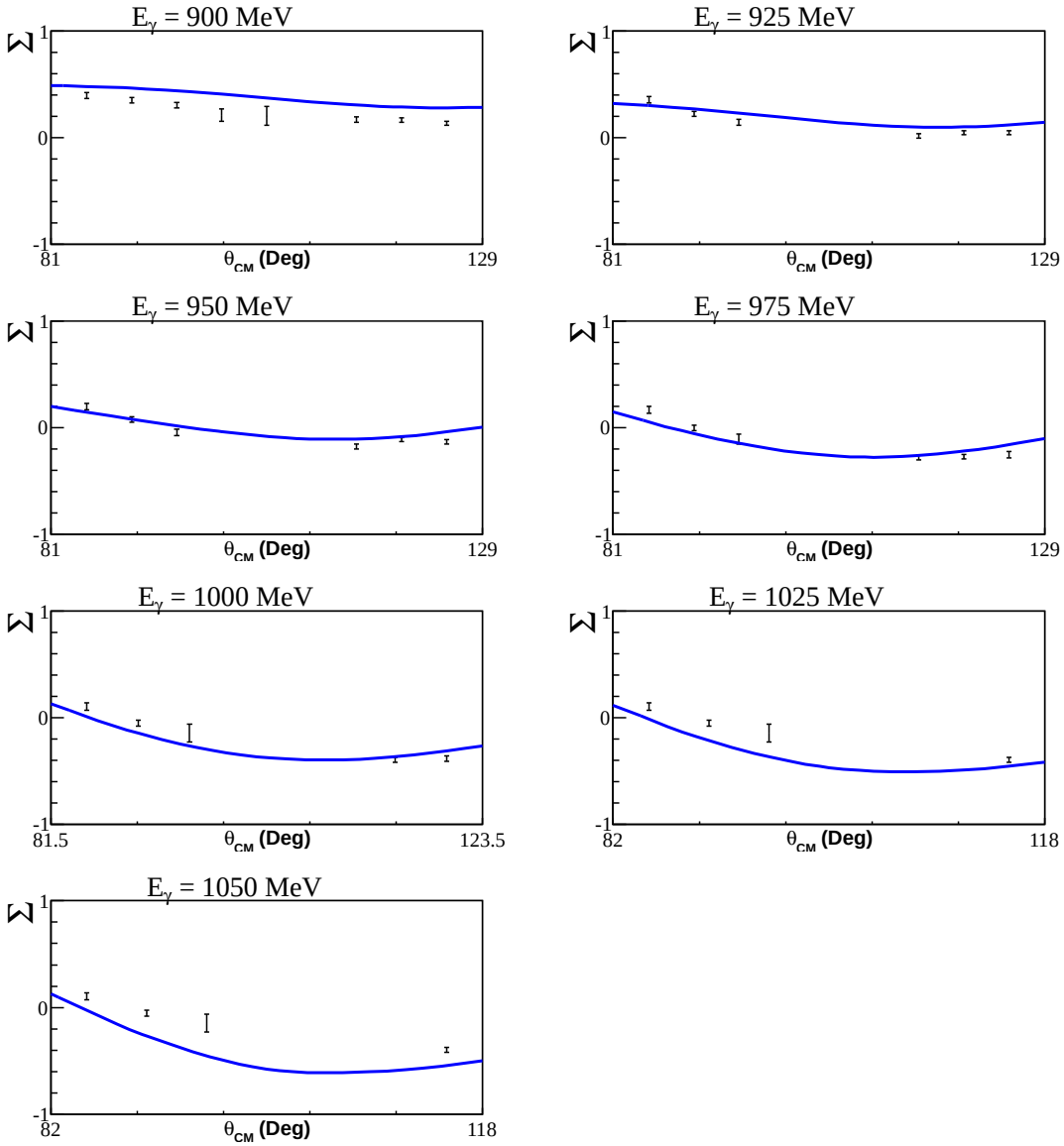

Figure 2.3: Measurement of the Σ observable performed at the Yerevan Synchrotron for $900 < E_\gamma < 1050$ MeV. The blue line shows the SAID model prediction. The θ angles are from the π^0 in the centre of mass.

The GRAAL experiment

The GRAAL (GRenoble Anneau Accélérateur Laser) facility is a Compton back-scattering facility, which generates its beam via the scattering of photons off electrons [25]. Charged and neutral particles are detected at GRAAL using the LAGRANγE (Large Angle GRaal beam Apparatus for Nuclear γ Experiments) detection system, capable of coverage of $0° < \theta < 155^0$ across two separate setups.

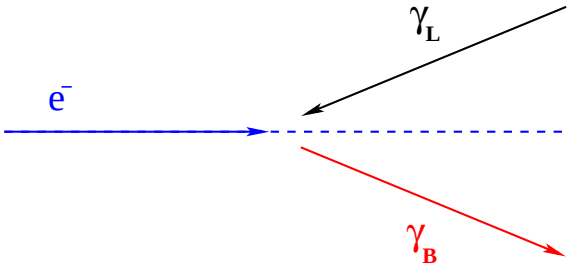

Figure 2.4: Simple diagram to represent the Compton back-scattering used to produce the GRAAL photon beam. e^- is the electron beam, γ_L is the incident laser beam and γ_B is the back-scattered photon beam.

A Compton beam is generated by the process of back-scattering a laser beam off an electron beam (figure 2.4). This process is advantageous as the incident scattered photon preserves almost 99% of the incident laser beam polarisation, and the entire range is considered to be polarised, unlike the coherent *bremsstrahlung* process. However, because of the small cross-section associated with the scattering process, the intensity of the beam is much lower, and as such the experiment must run for longer to accrue statistics. The scattered electron beam is diverted and measured in order to provide the kinematic information of the photon beam. The beam is passed to the detection systems where subsequent reactions are detected in coincidence with the electron event.

The detection systems used in the LAGRANγE setup consist of a calorimeter known as the BGO (Bismuth Germanate) ball, a set of tracking chambers for detection of charged particles in coincidence with the BGO system and a forward wall detection system for detecting particles at forward angles. A schematic diagram of the LAGRANγE detector system is shown in figure 2.5. The measurement of the Σ observable took place at energies ranging from $550 < E_\gamma < 1500$ MeV and had a

relatively large kinematic range from $59° < \theta^{\pi^0}_{CM} < 153°$. The results of the GRAAL measurement of Σ are shown in figures 2.6, 2.7, 2.8 and 2.9.

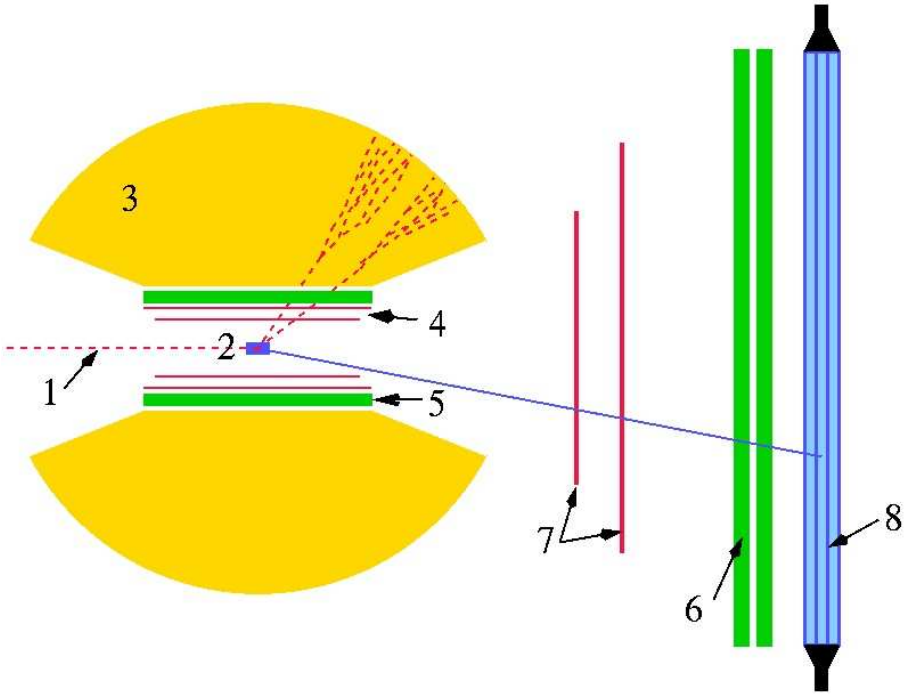

Figure 2.5: Diagram of the LAGRANγE detector system. The annotations are as follows: 1. The incoming Compton beam, 2. The lH_2 target, 3. The BGO calorimeter, 4. Internal wire tracking chambers, 5. Plastic scintillators, 6. Plastic scintillator forward wall, 7. Forward wire tracking chambers and 8. Forward shower wall.

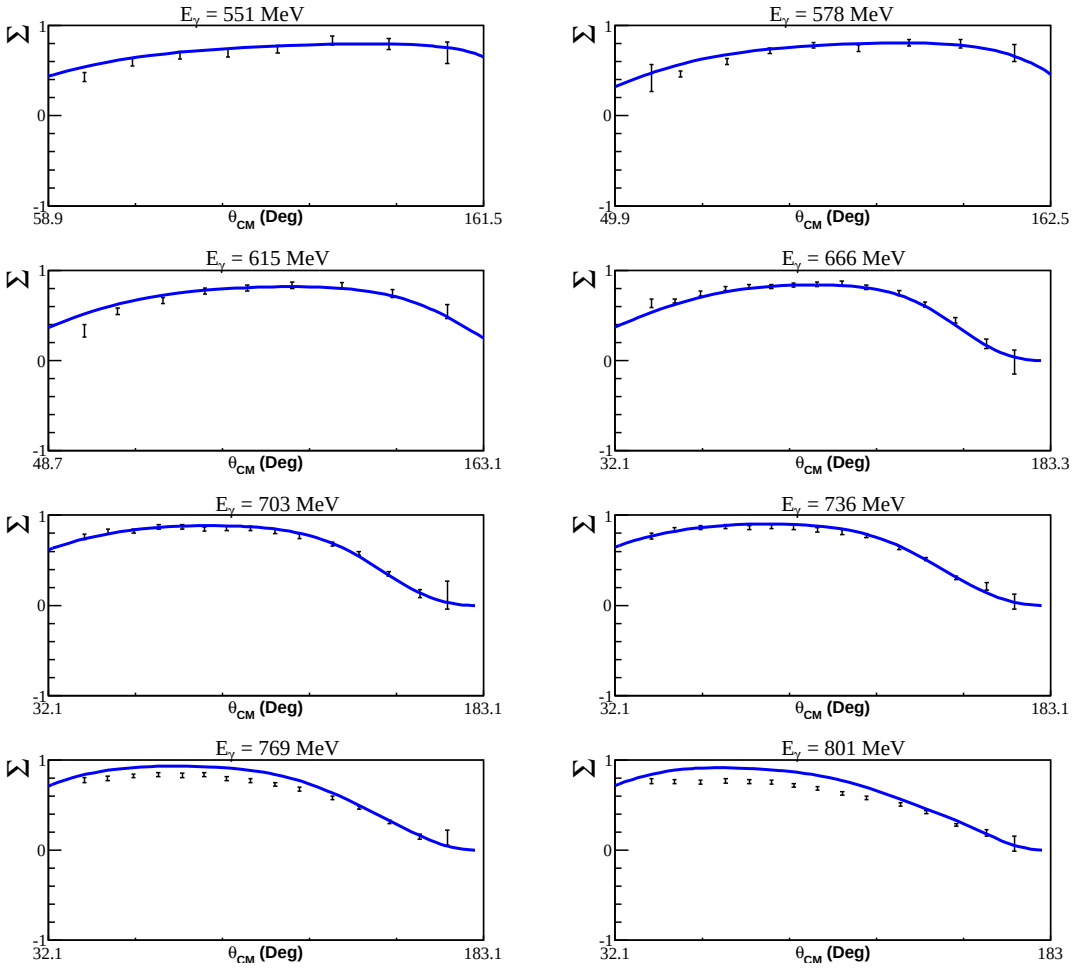

Figure 2.6: GRAAL results for the Σ measurement for $551 < E_\gamma < 801$ MeV. The blue line is the SAID model prediction. The θ angles are from the π^0 in the centre of mass.

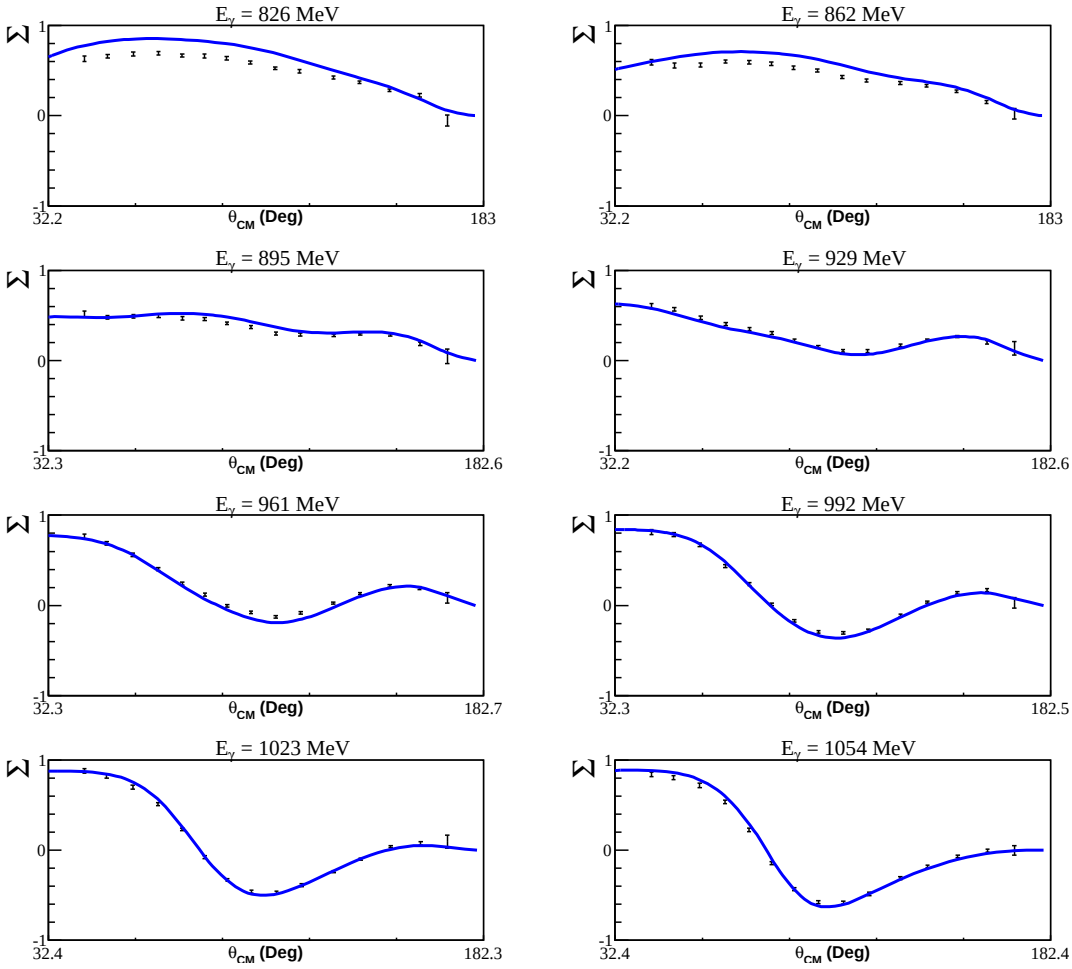

Figure 2.7: GRAAL results for the Σ measurement for $826 < E_\gamma < 1054$ MeV. The blue line shows the SAID model prediction. The θ angles are from the π^0 in the centre of mass.

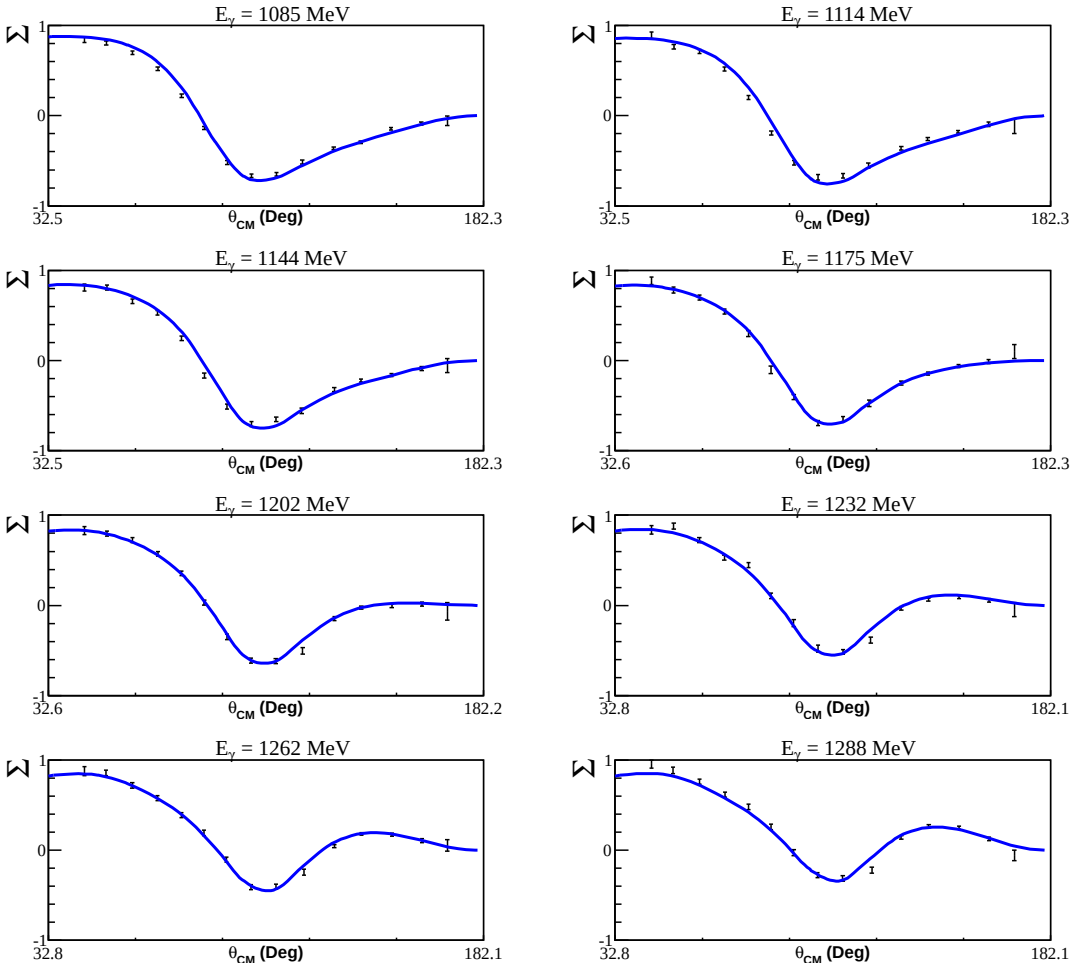

Figure 2.8: GRAAL results for the Σ measurement for $1085 < E_\gamma < 1288$ MeV. The blue line shows the SAID model prediction. The θ angles are from the π^0 in the centre of mass.

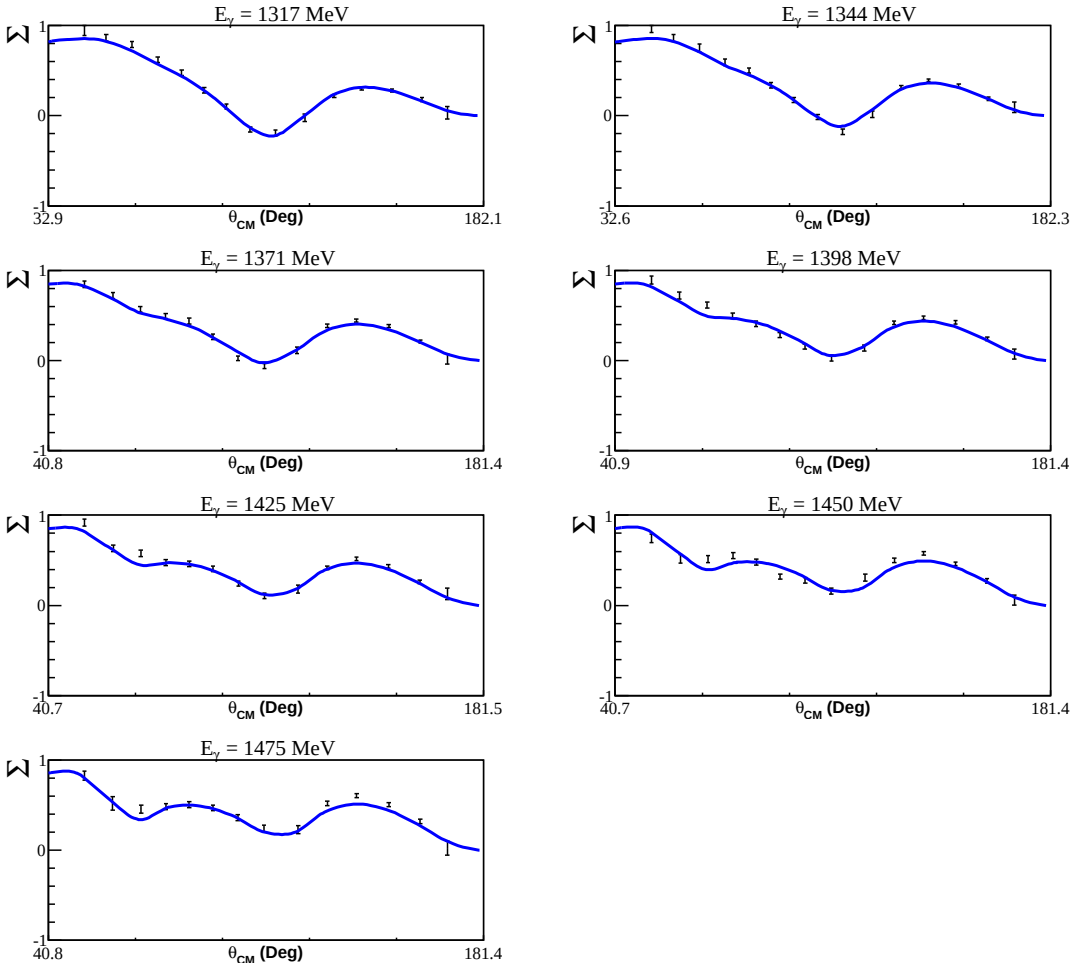

Figure 2.9: GRAAL results for the Σ measurement for $1317 < E_\gamma < 1475$ MeV. The blue line shows the SAID model prediction. The θ angles are from the π^0 in the centre of mass.

2.2.2 Recoil Measurements

Study of the beam-recoil observables is relatively narrow, with only a few previous measurements of both circularly polarised states (C_x and C_z) and the linearly polarised states (O_x and O_z). Measurements with an analyzing material for secondary scattering have been conducted on different reaction mechanisms, such as with Compton scattering [34]. Measurements on the $\gamma p \rightarrow \pi^0 p$ reaction carried out at Kharkov in the late 1970's extracted the observable O_x [35, 36] but had poor kinematic coverage (figure 2.10). Recent measurements of C_x and C_z have been performed at Hall-A at Jefferson Laboratory [37], as well as a measurement of C_x at lower energies at MAMI [38].

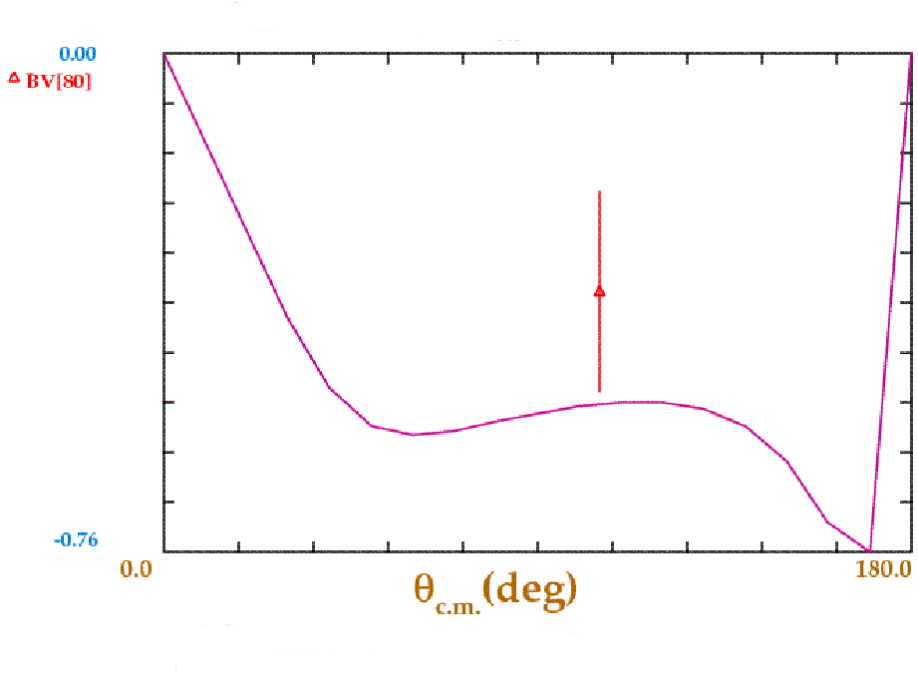

Figure 2.10: The world data for the observable O_x from the SAID database. Plotted between $450 < E_\gamma < 650$ MeV. The plotted data point is from the measurement at Kharkov [35]

The present analysis allows simultaneous extraction of the recoil observables and the single target polarisation observable T. There have been numerous previous measurements for this observable in the energy and angle range covered in this thesis, most of which suffer from poor statistical accuracy and kinematic coverage. The situation was improved by a recent measurement at Bonn [39]. The results

of this Bonn measurement and the predictions from the SAID model are shown in figure 2.11.

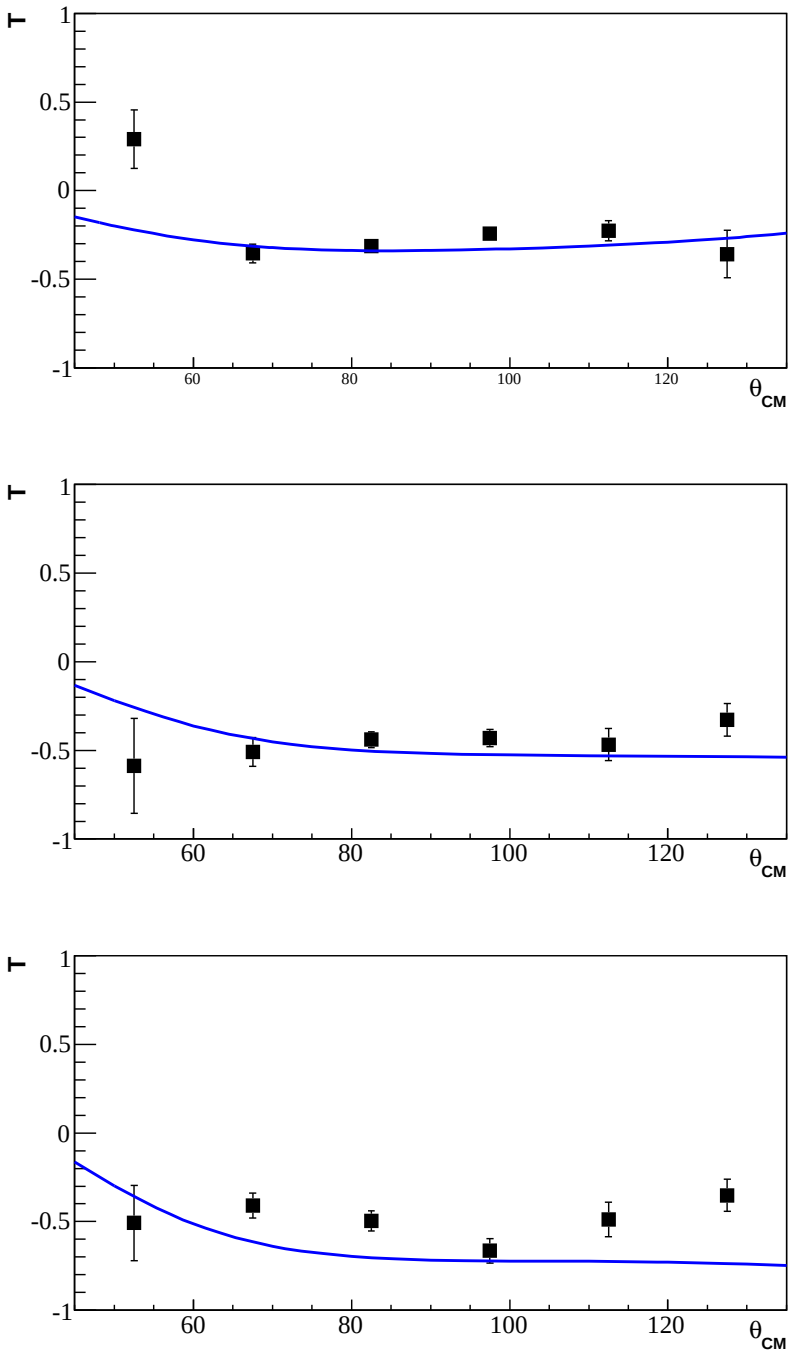

Figure 2.11: Previous measurements from Bonn and SAID predictions for the observable T. Plotted between $450 < E_\gamma < 650$ MeV.

Hall-A Measurement

The measurement of C_x, C_z and P was carried out at Hall-A Jefferson Lab [37]. The measurement was performed using the High Resolution Hadron Spectrometer (HRHS) [40] on the $\gamma p \rightarrow \pi^0 p$ reaction channel using circularly polarised photons. Unlike a traditional *bremsstrahlung* facility, the beam in Hall A is not tagged and as such the mixed electron-photon beam must be reconstructed and separated within the analysis. The HRHS is a magnetic wide-angle spectrometer, designed to have set angles where charged particles are deflected based on their momentum by bending magnets into a series of detector systems. Due to the two body kinematics of the $\gamma p \rightarrow \pi^0 p$ reaction, each fixed angle provides a photon energy and angle in the lab.

The HRHS has tracking chambers sandwiching the carbon polarimeter, as well as a Čerenkov counter, and scintillation counters (figure 2.12). The tracking chambers provide proton tracks before and after the carbon analyzer and the Čerenkov and scintillators provide particle identification information. The use of tracking chambers with this kind of secondary scattering technique for determining recoil polarisation allows extremely accurate determination of scattering angles. Additionally, the precessing of spin in the bending magnets allows access to the z-component of the proton spin (C_z in this case), which is not possible with the A2 setup (chapter 3) due to the absence of a magnetic field in the Crystal Ball setup. The results for C_x and C_z from the Hall-A experiment can be seen in figure 2.13, showing previously unmeasured results over a wide range of energies for several set angles. A recent result covered in a similar setup in Hall-C at Jefferson Lab has expanded the kinematic range of these measurements considerably [41].

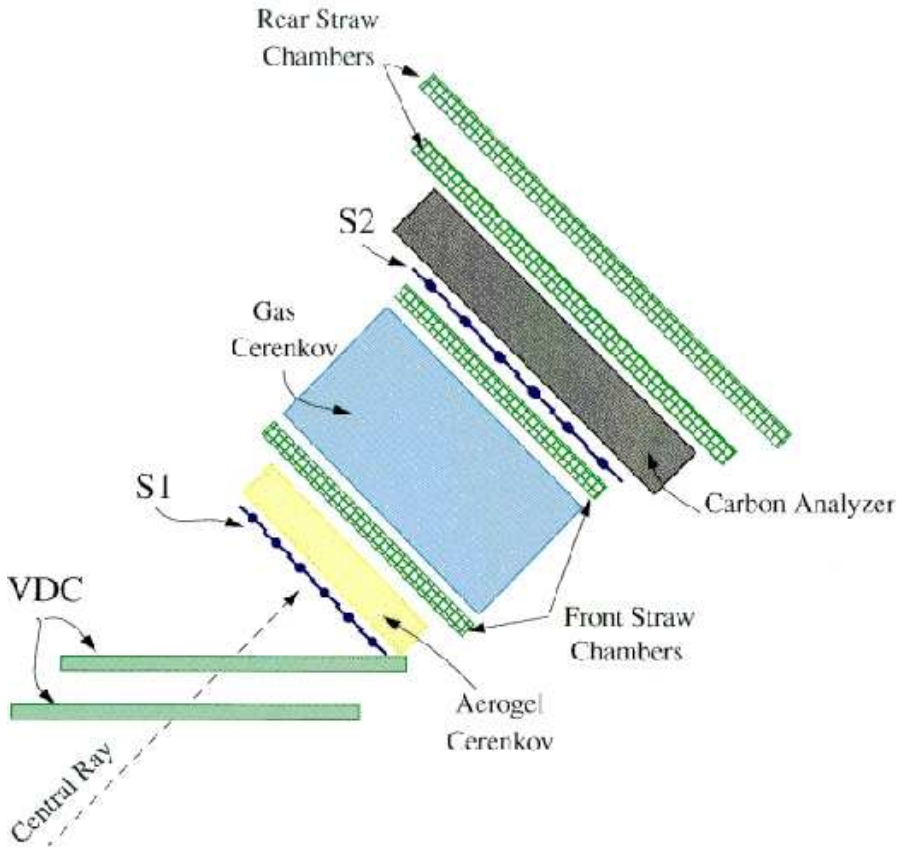

Figure 2.12: The HRHS detector arm, showing the tracking chambers, Čerenkov detectors, scintillators and carbon analyzer [40]. S1 and S2 are scintillator hodoscopes, and VDC are vertical drift chambers.

2.2.3 Summary

The study of polarisation observables has been wide ranging, yet lacking in some energy regimes, such as $450 < E_\gamma < 650$ MeV. A large volume of work has been shown on the single observables, however many of the studies lacked significant kinematic coverage. Advancements in the field has yielded the ability to perform measurements of more complex results using recoil polarisation, thus expanding the kinematic range in which preliminary measurements of these results can be made. The development of polarised targets using Dynamic Nucleon Polarisation [42] and millikelvin cooling technology has allowed double polarisation states such G, F, E and H to be accessed and measured for the first time in ongoing hadronic physics programs. Finally, with new experiments using recoil polarisation in pseudoscalar

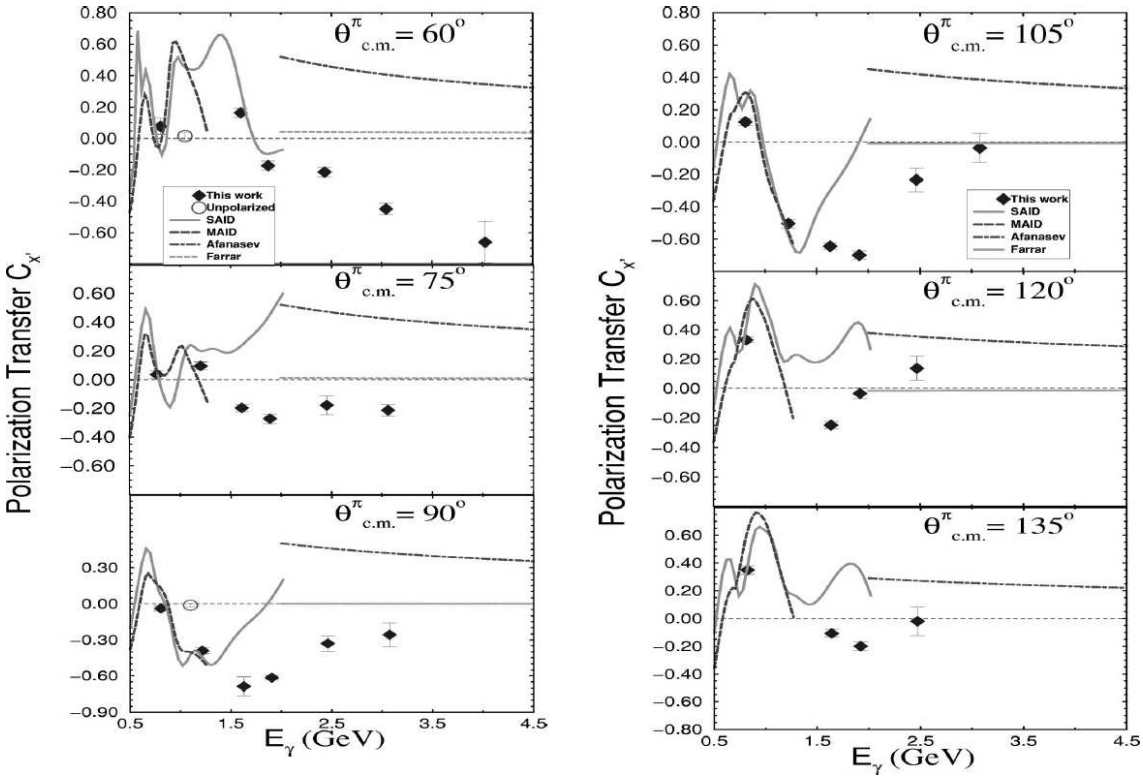

(a)

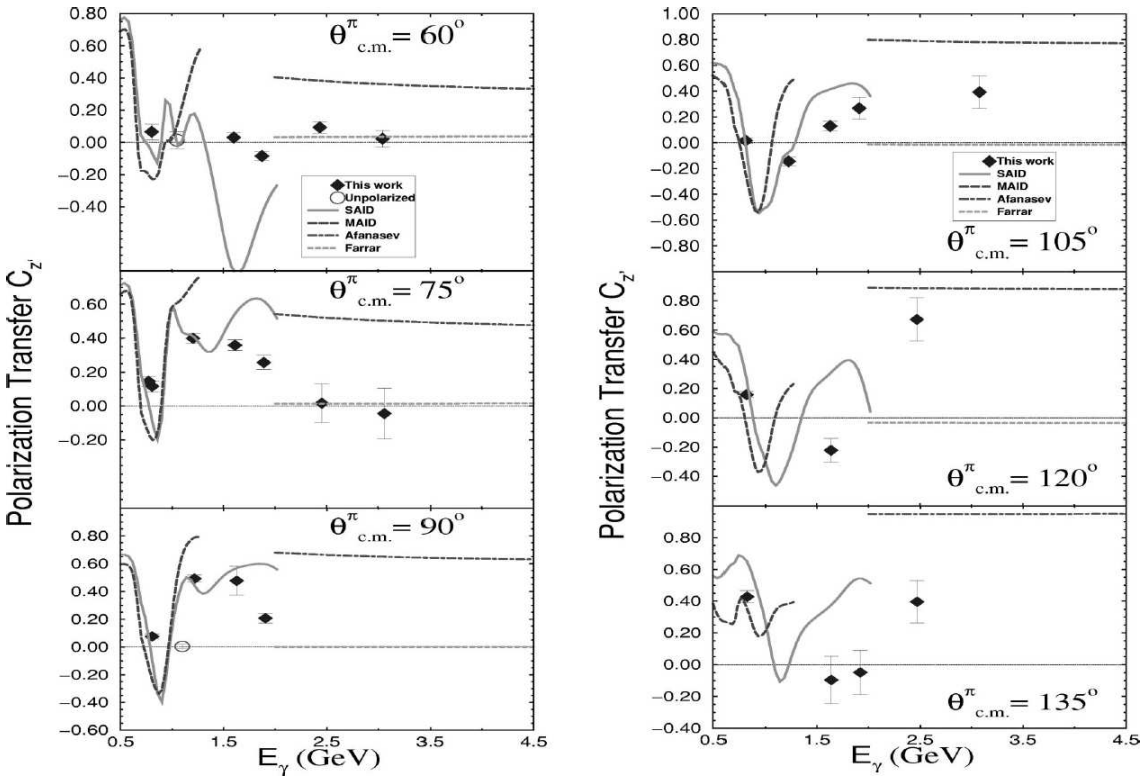

(b)

Figure 2.13: The results from the Hall-A experiment for C_x (a) and C_z (b), from [37].

meson production and the development of these polarized targets allows access to the target-recoil observables T_x, T_z, L_x and L_z, allowing for a complete measurement of all polarisation observables.

Chapter 3

Experimental Setup

This chapter describes the A2 experimental hall at MAMI in the Institut für Kernphysik, the facility where this experiment took place. Figure 3.1 shows a schematic of the experimental setup within the A2 hall.

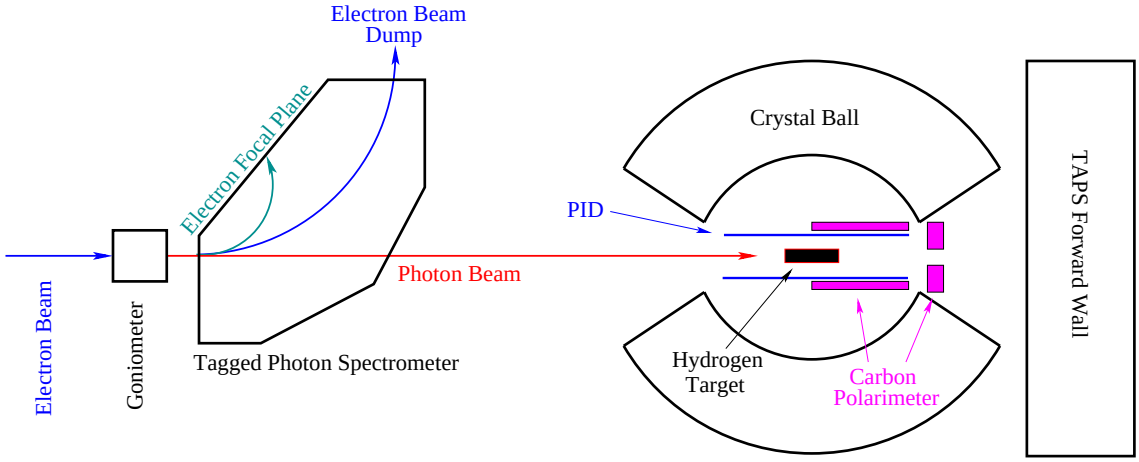

Figure 3.1: Schematic Overview of the A2 setup

The MAMI accelerator produces an electron beam incident on a radiator to produce a *bremsstrahlung* photon beam. The scattered electrons are bent out of the beam, and have their kinematic information measured using the Glasgow Tagged Photon Spectrometer. The photon beam is then incident on a liquid hydrogen target cell at the centre point of the Crystal Ball calorimeter, and upstream of the TAPS calorimeter. A plastic scintillator hodoscope known as the PID surrounds the target, as well as a carbon scatterer. A further carbon scatterer plugs the forward hole in

the Crystal Ball towards TAPS.

3.1 MAMI

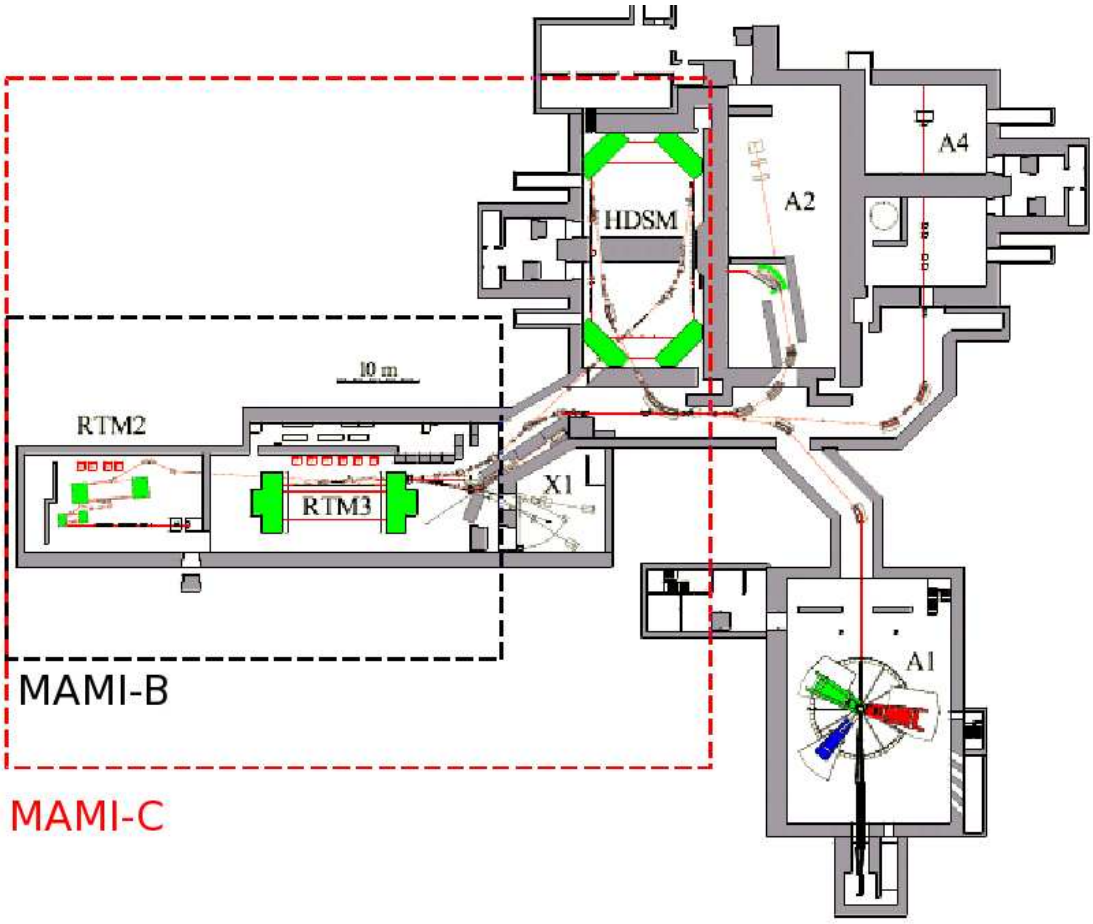

Figure 3.2: MAMI facility layout

The layout of the MAMI (Mainzer Mikrotron) facility [43] is shown in figure 3.2. MAMI is a combination of a Linear Accelerator (LINAC), three Racetrack Microtrons (RTM) and a Harmonic Double-Sided Microtron (HDSM). The facility is capable of producing a highly stable, intense continuous wave electron beam with 100% duty factor. MAMI can run a broad spectrum of energies from 14 MeV up to 1.6 GeV.

The Racetrack Microtron

The fundamental design of the RTMs at MAMI is a series of recirculating tracks running through two 180° bending magnets, passing into a short radio-frequency LINAC, situated in a section free of magnetic fields [44]. Electrons are injected into the LINAC. This then provides acceleration through radio-frequency cavities. The subsequent beam of electrons is passed to the bending magnets and undergoes a 360° bend back to the LINAC. Multiple circulations through the LINAC provides a steady increase in energy, passing the electrons through progressively longer tracks as illustrated in figure 3.3.

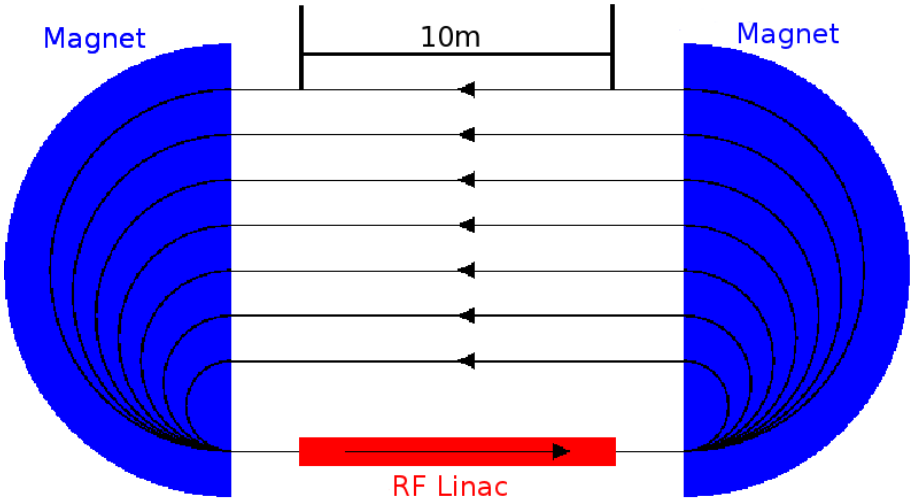

Figure 3.3: Schematic of a generic racetrack microtron

MAMI has three RTMs, MAMI-AI, MAMI-AII and MAMI-B. MAMI-AI and MAMI-A2 make up MAMI-A, into which electrons are injected into at an energy of 3.5 MeV. MAMI-AI is capable of ramping this energy up to 14 MeV. MAMI-AII pushed this up to 187 MeV, allowing experiments to be carried out over the π^0 threshold (∼147 MeV). MAMI-B carried the total energy of MAMI to 855 MeV which pushed over the η threshold (∼708 MeV).

The Harmonic Double-Sided Microtron

The HDSM works under a similar principle. The characteristic difference between the HDSM and a traditional RTM is that it operates two LINACs with in phase

radio-frequency cavities [45]. The beam is bent through four 90° bending magnets and progressively longer tracks between two of the bending magnets on both sides (Figure 3.4). The two LINACs of the HDSM are operated operated at 2.45 GHz and 4.9 GHz. These two frequencies were picked in order to conserve a focused electron beam right up until the end of circulation [45].

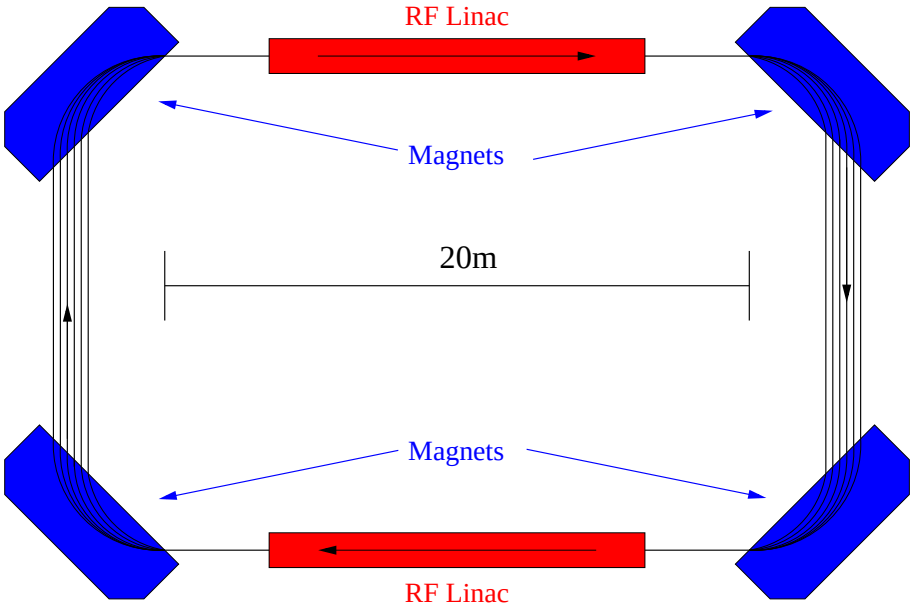

Figure 3.4: Schematic of the Harmonic Double-Sided Microtron

The motivation behind the design of the HDSM, named MAMI-C, was practicality as the design of a traditional RTM would require the bending magnets to weigh greater than 2000 tonnes each. The HDSM brought the MAMI beam from the 855 MeV output of MAMI-B up to 1.5 GeV, going over the strangeness threshold (∼900 MeV). MAMI-C is now capable of operating at 1.6 GeV, providing the A2 hall with the scope to study the η' at threshold (∼1450 MeV). The energy ranges of the microtrons are detailed in table 3.1

		First RTM	Second RTM	Third RTM	HDSM
Injection Energy	MeV	3.97	14.86	180	855
Extraction Energy	MeV	14.86	180	855	1504
Number of turns		18	51	90	43
Energy Spread (1σ)	keV	1.2	2.8	13	110

Table 3.1: Summary of MAMI beam parameters

3.2 The Tagged Photon Spectrometer

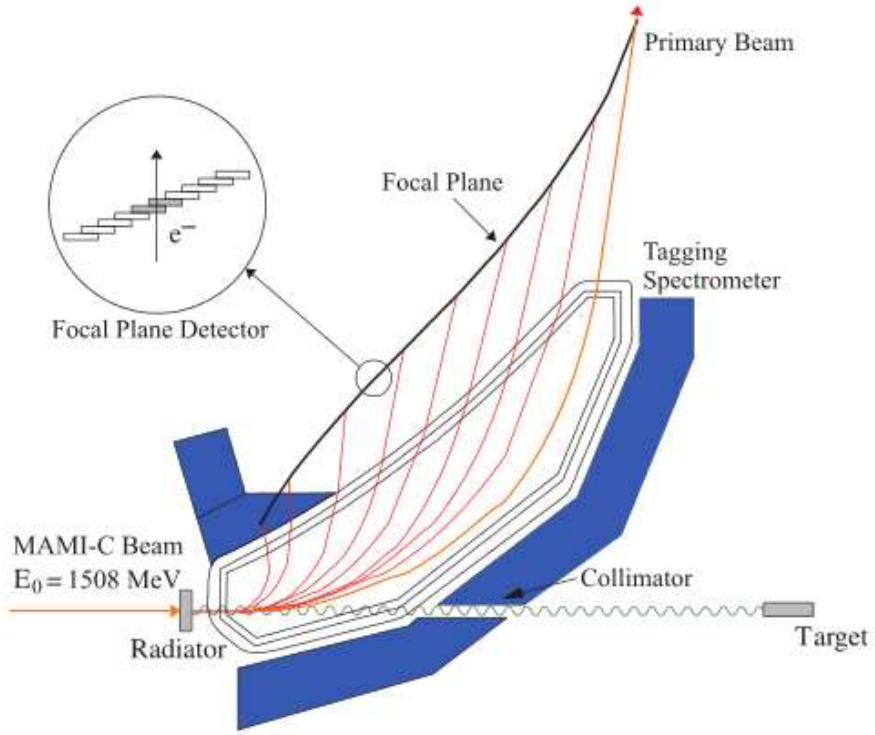

Figure 3.5: Schematic of the Tagged Photon Spectrometer

Figure 3.5 shows a schematic of the Glasgow Tagged Photon Spectrometer (Tagger) [46]. The principal function of the Tagger is to provide the energy of the photon beam used in the photoproduction experiments. Additionally, the Tagger provides a timing coincidence. This is key for experimental running, as multiple electrons are detected for any given event in the experimental area. By examining the timing coincidence between the experimental trigger, it is possible to separate the photon which induced the reaction in the experimental area. The Tagger is composed of three main components: the Goniometer, the Dipole Magnet and the Focal Plane Detector (FPD).

The Goniometer

The Goniometer houses radiators for the production of photon beams. It consists of 3 precise rotational stages and two transverse stages. The transverse stages are

used to place selected radiators into the beam line via remote access, thus reducing interruptions to the beam. One of the transverse stages can be used to move a Møller Coil into the beam line for Møller scattering experiments. The rotational stages are used for the orientation and alignment of the diamond radiator for linearly polarised photon running (see section 3.2.1).

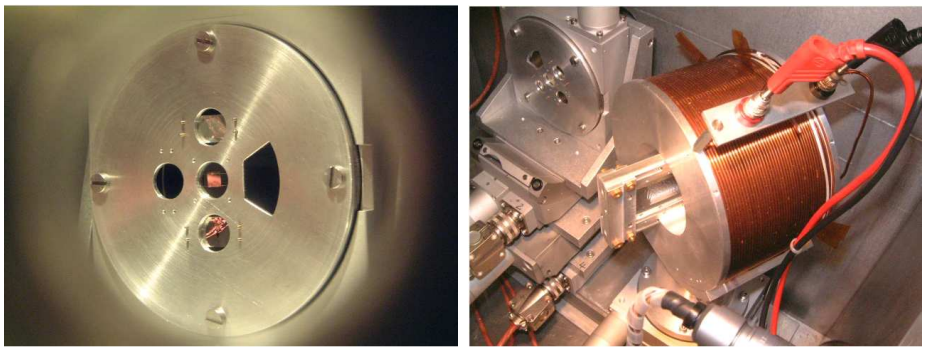

(a) (b)

Figure 3.6: (a). The Goniometer wheel and radiators (Copper, Nickel, Iron, Diamond and Blank). (b). The Goniometer (Left) and Møller coil (Right)

Bremsstrahlung Production

Bremsstrahlung is the process in which the photon beam is generated for use in photoproduction experiments. In general it involves the scattering of an electron off a nucleus. The electron will lose kinetic energy as it is deflected by the Coulomb field of a nucleus. This energy is conserved in the form of the emission of a *bremsstrahlung* photon [47] as in equation 3.1 and figure 3.7.

$$e_0^- + N \rightarrow e_{Sc}^- + N + \gamma_{Brem} \tag{3.1}$$

While the nucleus will experience a recoil effect from the scattering of the electron, this is of the order of a small amount of keV, and is therefore considered negligible to the system. The principal in the A2 experiment is that a beam of electrons at an energy E_0 is fed into the experimental hall, striking a radiator. Within the radiator, usually a metal wafer, the *bremsstrahlung* process occurs emitting a photon

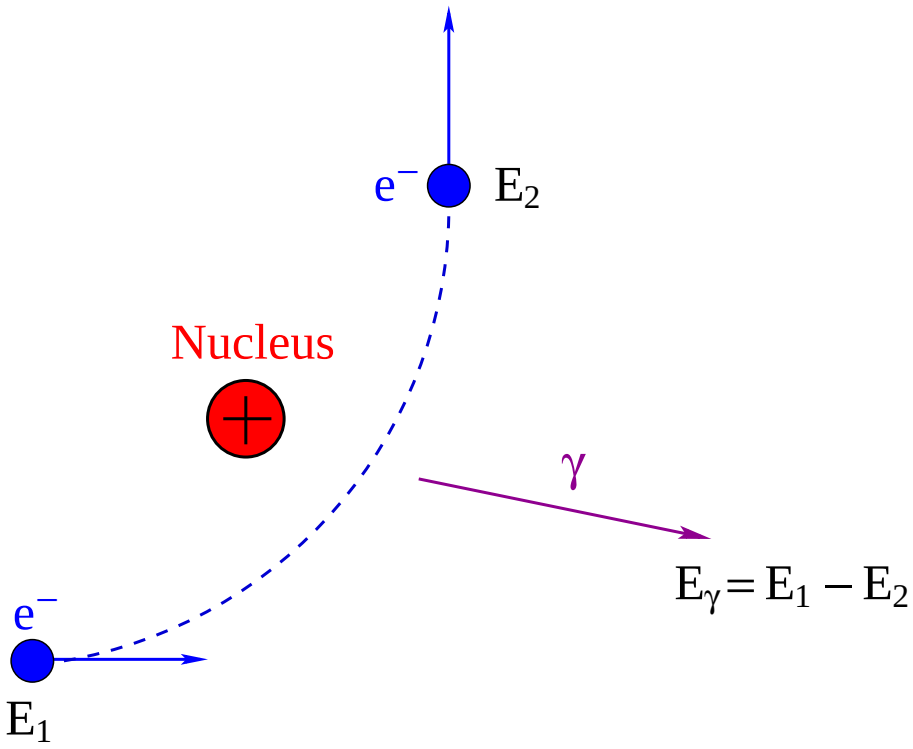

Figure 3.7: Basic concept of Bremsstrahlung

of energy E_γ. The energy of this photon can be determined by the detection of the now decelerated electron, E_{e^-}.

Tagging

$$E_\gamma = E_0 - E_{e^-} \tag{3.2}$$

As previously mentioned, the function of the Tagger is to measure the energy of the photons on an event by event basis. This process is referred to as tagging. As seen in equation 3.2, the information needed to calculate the beam photon energy is the energy of the decelerated electron, required to "tag" the photon.

After the radiator, both the photon and the electron enter the large Tagger dipole magnet [48]. Within the field of the magnet the electron is bent away from the path of the photon beam and into the FPD. The field of the dipole magnet is set such that electrons that do not decelerate in the radiator ($E_0 = E_{e^-}$) are diverted into a lead-lined beam dump. As such, electrons which have lost energy in the radiator

are diverted at increasingly tighter angles. These electrons strike the FPD.

The FPD is an array of 353 overlapping plastic scintillator elements [49]. Each element overlaps with an adjacent element giving the FPD a total of 352 coincidence channels. An electron striking two overlapping elements gives a signal in the FPD. The channels in the FPD do not directly read out any information on the energy of the electron. Instead the position on the focal plane is indicative of the energy loss of the electron. For example, an electron which has lost very little energy in the radiator will be diverted less in the dipole field and will thus interact with an element at the end of the focal plane near the beam dump. Conversely an electron that has lost most of its energy in the radiator will divert at a sharp angle at the end of the focal plane near the goniometer.

Using simulated models, the spectrometer is mapped for all possible electron momenta within the acceptance range of the focal plane. Then the geometry of the plane, as well as position and orientation of the scintillators is defined by the calculated angles and trajectories of the electrons. This position is mapped to be as perpendicular to the electron vector as possible. The widths of the individual scintillators varies across the focal plane, from 9mm to 32mm. This ensures that each channel can approximately cover the same energy range across the non-uniform focal plane. The overlap ensures the rejection of electron events that have undergone multiple scattering, and only events that give a signal in both overlapping scintillators are accepted. A typical *bremsstrahlung* spectrum using an amorphous ${}_{29}Cu$ radiator is shown in figure 3.8. This shows the characteristic $\sim \frac{1}{E}$ behavior with photon energy.

3.2.1 Coherent Bremsstrahlung

Using a continuous electron beam from the MAMI accelerator and inducing the process of *Coherent Bremsstrahlung* [50] it is possible to produce linear (ie transversely) polarised photons. Scattering electrons off a rigid crystal structure induces this process. A crystal has a structure of regular arrays of atoms, allowing recoiling

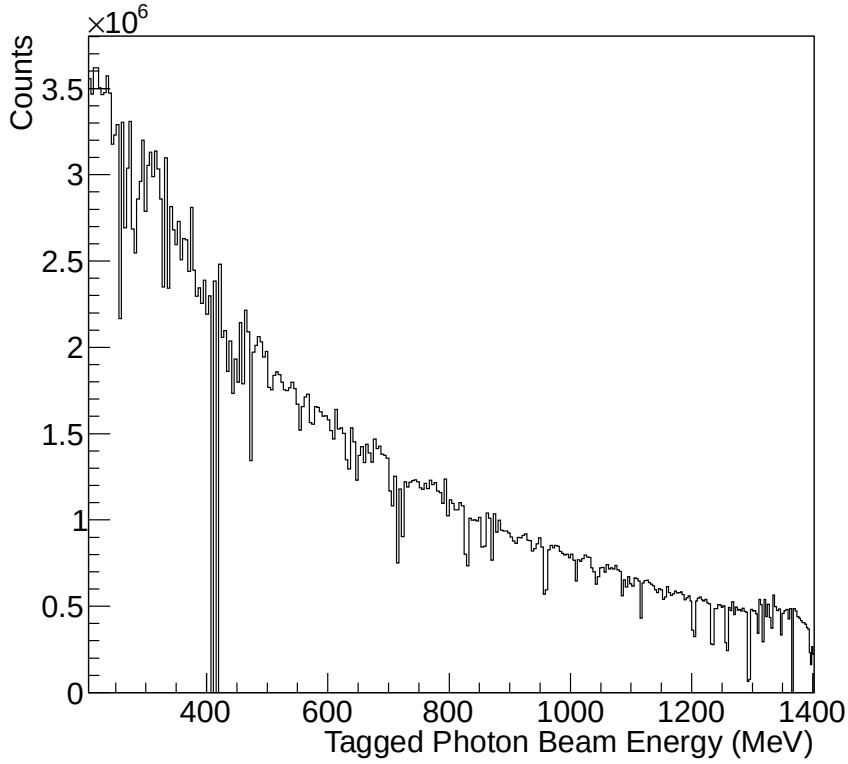

Figure 3.8: Tagged photon beam energy spectrum

momenta to be absorbed by the lattice rather than the individual nuclei. This allows production related to specific momentum transfers from the initial electron on the crystal along the lattice vector $\overrightarrow{g}$. This arrives from the Laue condition [51],

$$\overrightarrow{q} = \overrightarrow{g} \tag{3.3}$$

and

$$\overrightarrow{q} = p_0 - p - k \tag{3.4}$$

in which $\overrightarrow{q}$ is the momentum transferred to the crystal and $\overrightarrow{g}$ is the reciprocal lattice vector responding to *coherent bremsstrahlung* production. p_0 is the electron's initial momentum, p is the electron's final momentum and k is the energy of the *bremsstrahlung* photon produced. Sensitive orientation of the crystal radiator allows the selection of the desired reciprocal lattice vector in reference to the initial electron beam. This allows the production of high degree polarisation photons [51, 52].

The product of this interaction gives a linearly polarised region from the selected energy range sitting on an incoherent background. The coherent enhancement increases with initial electron energy, E_0 [50]. Diamond was chosen over other rigid structures such as silicon, due to the high Debye Factor [53] and therefore small amplitudes of thermal motion. Diamonds do however suffer from imperfections in their structure.

Bremsstrahlung processes are symmetric in the azimuthal plane of the initial beam direction and are separated by longitudinal and transverse momentum components. With a high enough energy, the momentum transfer, $\overrightarrow{q}$, is bound to a thin region of momentum space, coined the "Überall Pancake" [55]. The kinematic dimensions of this region are bound by the symmetry around the initial momentum plane, and thus are restricted by the aforementioned longitudinal and transverse momentum components of $\overrightarrow{q}$, q_l and q_t (see equations. 3.5, 3.6).

$$\delta \leq q_l \lesssim 2\delta \tag{3.5}$$

$$0 \leq q_t \lesssim 2x \tag{3.6}$$

Where δ is the minimum recoil momentum deposited in the longitudinal direction, and x is the quantum energy, defined by the ratio between the energy of the *bremsstrahlung* photon and the incident electron energy. The alignment of the crystal [56] allows for the production of a high degree of linear polarisation.

Collimation of the polarised beam is also key to gaining the highest degree of linear polarisation possible. As described by Timm [50] and Lohmann [51], the coherent photons will be very strongly forward-focused, whereas the incoherent background is dependent more on the energy of the photon itself, thus the introduction of a tight collimator [57] can increase the degree of linear polarisation. Figures 3.9 and 3.10 show how the enhancement is produced from the Tagger spectra and an example of the fit using the AnB method.

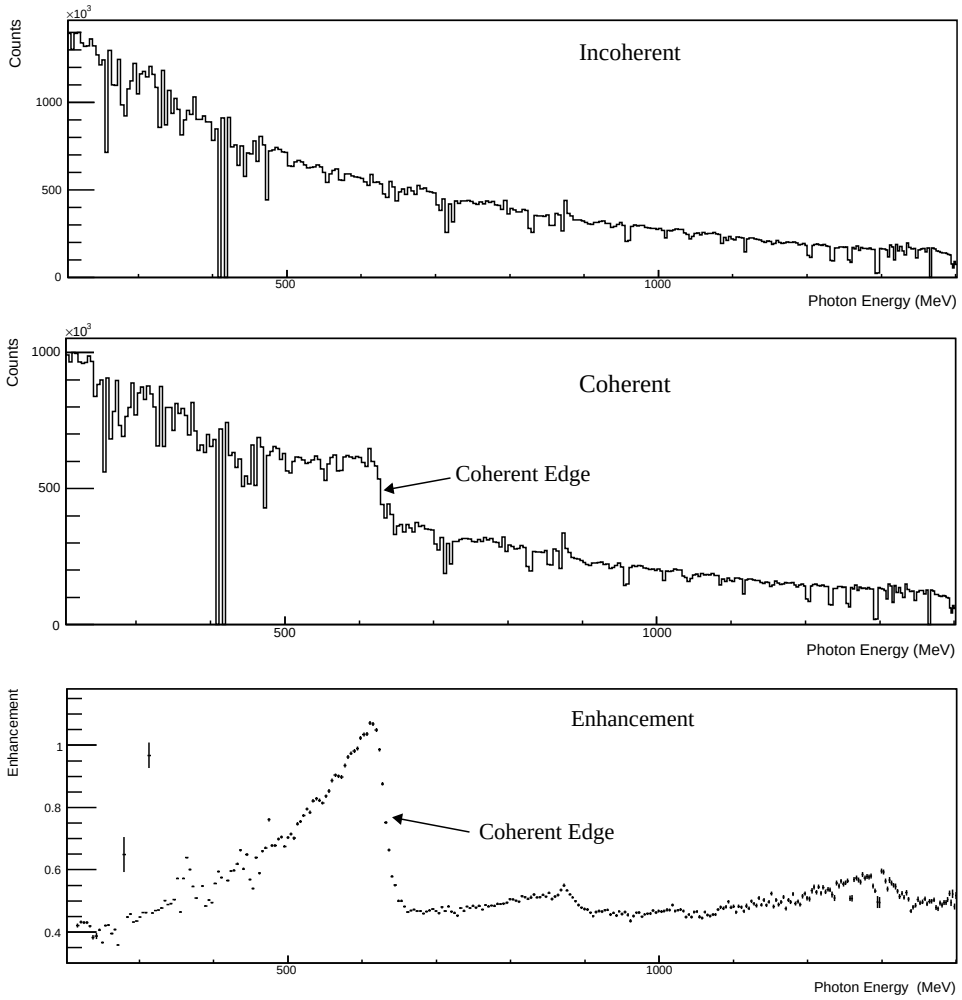

Figure 3.9: Photon energy spectrum showing the incoherent contribution (top), the coherent contribution (middle), and the resulting enhancement from dividing out the incoherent contribution (bottom).

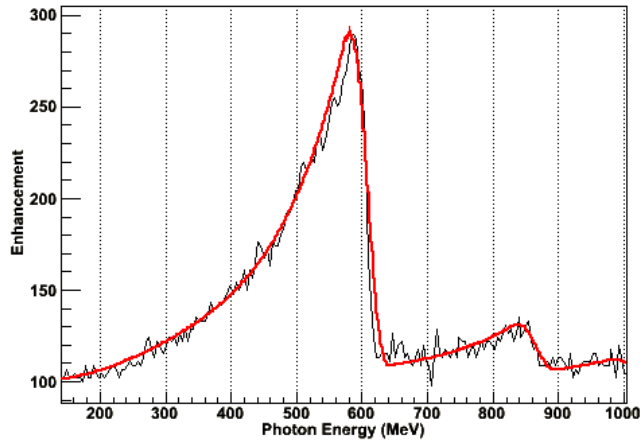

(a) Enhancement of Coherent Spectra without Incoherent background

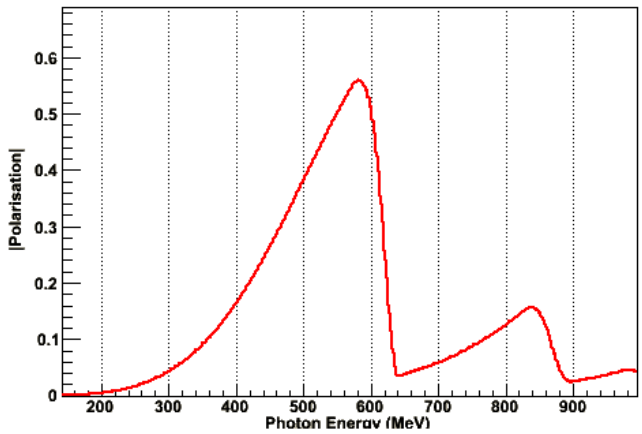

(b) Polarisation Calculated from Enhancement

Figure 3.10: Polarisation (in photon energy) calculated with the analytical bremsstrahlung calculation [54]

3.3 The Crystal Ball

The Crystal Ball is a highly granulated total energy electromagnetic calorimeter, approximated by an icosahedron [59, 60]. Originally designed and built at SLAC to study the J/Ψ [61], the Crystal Ball has been used in multiple setups, including DESY, Brookhaven National Laboratory and now the A2 hall at the MAMI facility. Figure 3.11 shows a schematic diagram of the Crystal Ball with some crystals removed, and figure 3.12 shows a photograph of the Crystal Ball in preparation for the experimental setup. The geometry of the Crystal Ball, seen in figure 3.13, has twenty major triangles of an icosahedron. Each major triangle is divided into four minor triangles, made up of a set of nine small triangular faces. This makes up a

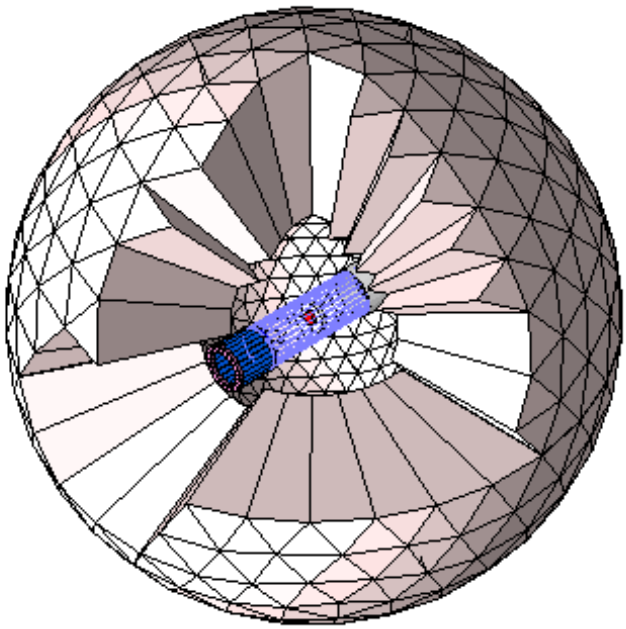

Figure 3.11: GEANT4 [58] model of the CB with the PID shown in blue.

nearly spherical array of 672 crystal elements, with an entrance and exit hole at either side. The sphere is separated into two hemispheres. Each crystal is NaI(Tl) and is a truncated triangular based pyramid, with the larger triangular face making up small triangular faces in each group. Each crystal element is 40.6cm in length, corresponding to ∼16 radiation lengths, attached to a photomultiplier tube (PMT) on the large face of the crystal. The base has a side length of 12.7cm and the inner face has a length of 5.1cm. The inner and outer radii of the Crystal Ball are 25.3 and 66cm respectively. Between the two hemispheres is a equatorial plane of 3.2mm stainless steel hodoscope seal. Accounting for the entrance and exit holes, the Crystal Ball has a near 4π acceptance (∼96%), and is optimized for photon detection.

Electromagnetic showers develop in the NaI(Tl) as photons deposit their energy. The energy deposited is usually contained within a cluster of 12-13 crystals. Due to the high light output of the NaI(Tl), and the high segmentation of the array, almost perfect photon detection efficiency is achieved (∼99%) with a high level of energy and angular resolution. The energy and direction of the photons can be reconstructed via the resulting shower in the cluster. Figure 3.14 shows a map of the

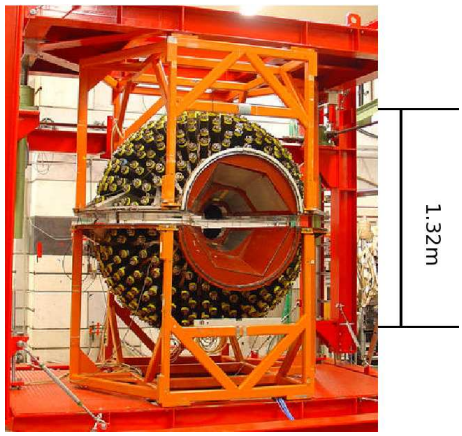

Figure 3.12: The Crystal Ball

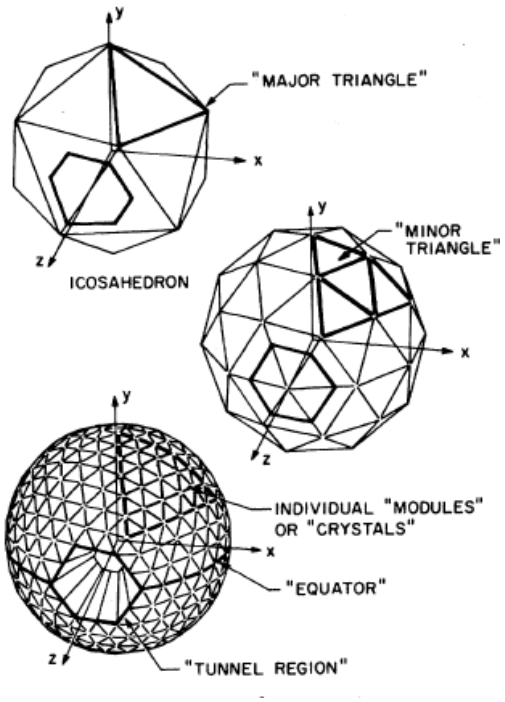

Figure 3.13: Breakdown of the Crystal Balls icosahedron approximation [61]

crystals in the Crystal Ball with single hits from photons, and table 3.3 summaries the characteristics of the Crystal Ball detector.

3.3.1 Particle Identification Detector

Because of the relatively poor timing response of NaI(Tl) crystals and short distance from the target cell to the crystals, it is not possible to use methods of charged particle identification such as Time-of-Flight. To account for this, a barrel of plastic

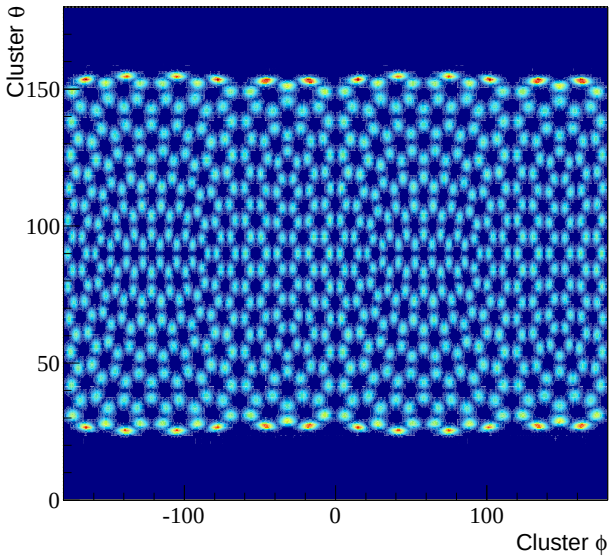

Figure 3.14: Crystal Ball Cluster ϕ vs. θ hits distribution

Acceptance	
Azimuthal coverage	$0^\circ \leq \phi \leq 360^\circ$
Polar coverage	$\sim 20^\circ \leq \theta \leq \sim 160^\circ$
Angular Resolution	
Azimuthal resolution	$\frac{2^\circ}{\sin\theta}$
Polar resolution	$\sim 2 - 3^\circ$
Photon Energy Resolution	
$\frac{\sigma}{E_\gamma}$	$\sim \frac{1.7\%}{E_\gamma}$ (GeV)$^{0.4}$
Timing Resolution σ_t	~ 50 ns

Table 3.2: Characteristics of the Crystal Ball

scintillators known as the Particle Identification Detector (PID) surrounds the target. Figure 3.15(a) shows the PID before insertion into the Crystal Ball. When charged particles interact with a PID scintillator, they will deposit a small amount of energy in the PID and go on to deposit the rest of their energy in the Crystal Ball. This allows the use of the EΔE technique for the identification of charged particles.

Figure 3.15(b) shows a typical EΔE plot. The strong ridge at the base of the plot corresponds to energy deposition from charged pions, which deposit a relatively uniform amount of energy in the plastic scintillators due to their small mass. The curved ridge above the charged pion ridge the energy deposited by protons in the

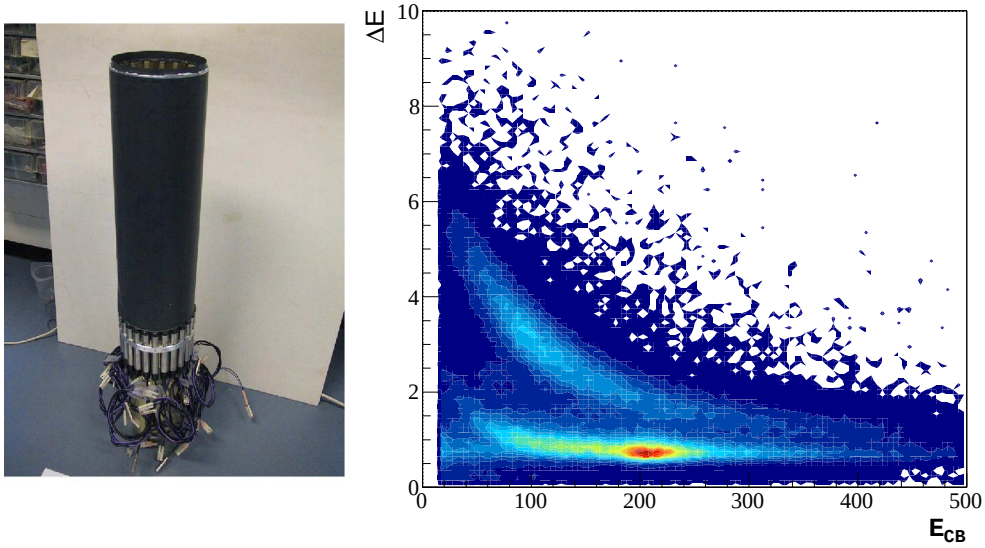

(a) Particle Identification Detector

(b) Typical EΔE Plot

Figure 3.15: The Particle Identification Detector and the EΔE method

plastic scintillators. The selection of regions around these ridges can be used to exclude or include them in a desired analysis.

3.3.2 Recoil Polarimeter

Protons scatter from a nucleon or nucleus in the Recoil Polarimeter in the Crystal Ball or TAPS Calorimeters. The Recoil Polarimeter (Figure 3.16) comprises of a 20.75cm graphite sheath around the target cell, concentrated at forward angles, as well as a 7.25cm thick graphite plug situated in the exit hole of the Crystal Ball. The cylinder has an inner and outer radius of 6.95cm and 9.25cm respectively. The plug has a radius of 9.25cm and has a small beam hole, 4cm in diameter machined at its centre. The principle of scattering in the recoil polarimeter will be covered in chapters 4 and 5.

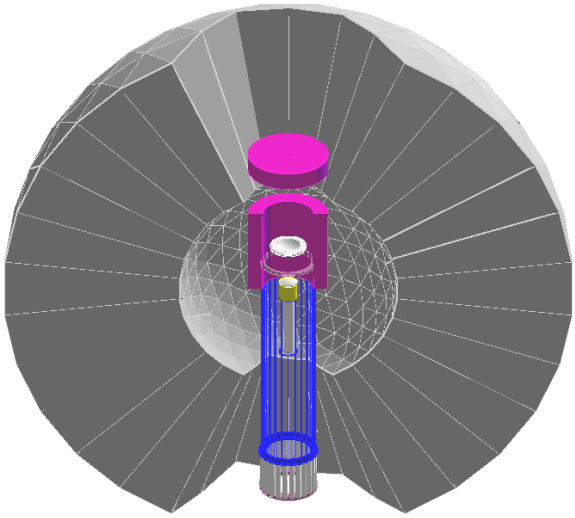

Figure 3.16: GEANT4 [58] model of the CB, showing the components of the Recoil Polarimeter and the PID.

3.3.3 The Liquid Hydrogen Target

The Liquid Hydrogen target cell is a cylindrical kapton container (shown in yellow in figure 3.16). It has a length of 4.8cm and a radius of 2cm, and is situated at the centre point of the Crystal Ball. Hydrogen gas is compressed into a liquid before being supplied to the target cell. Continual temperature control is maintained during running via pumping of additional liquid hydrogen into the system or evaporating excess hydrogen out of the system.

3.4 TAPS

Due to the lack of acceptance at the forward angle of the CB, the TAPS (traditionally, Two Armed Photon Spectrometer) [62] forward wall is used to cover the $0° < \theta < 20°$ exit hole. TAPS was originally used as a neutral detection system for MAMI-B, it was also used at GANIL and GSI. The detector's adaptable design allowed it to also be used at experiments at both Bonn and CERN. In the A2 setup, TAPS is configured as a hexagonal array of 384 BaF_2 crystals. Each crystal has a hexagonal cross section and length of 25cm ($\sim$12 radiation lengths). The crystals

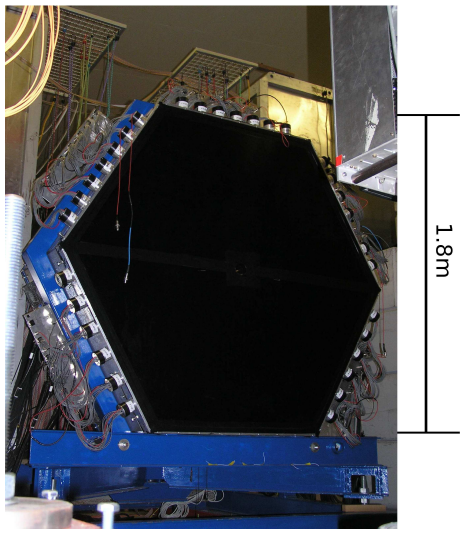

Figure 3.17: The TAPS Forward Wall

have a cylindrical end with a radius of 3cm. Each crystal is optically isolated with Polytetraflouroethylene (PTFE) and aluminium foil, and has a photomultiplier tube attached to the cylindrical end.

The front face of the TAPS detector is also covered in a layer of plastic scintillators, which cap off each detector. Their function is to provide EΔE information, since the PID has the same forward polar acceptance as the Crystal Ball, and cannot be used with the TAPS detector. The vetos are hexagonal themselves, and are composed of the same plastic material as the PID scintillators. Each one is 5mm thick, and has a small light guide to individual PMTs. TAPS has an array of different particle identification techniques associated with it. The veto caps on the crystals provide the option of a simple binary condition of either charged or neutral tagging. The BaF_2 crystals have a well defined scintillation response allowing the use of pulse-shape analysis, using the fast response of the crystals against the total energy to perform particle identification. The distance of the TAPS detector downstream of the target cell ($\sim$150cm) also allows the use of the Time-of-Flight technique. However, the latter three techniques were not employed in this analysis. Figure 3.18 shows a map of the crystals with single photon hits. Table 3.4 shows the characteristics of the TAPS detector.

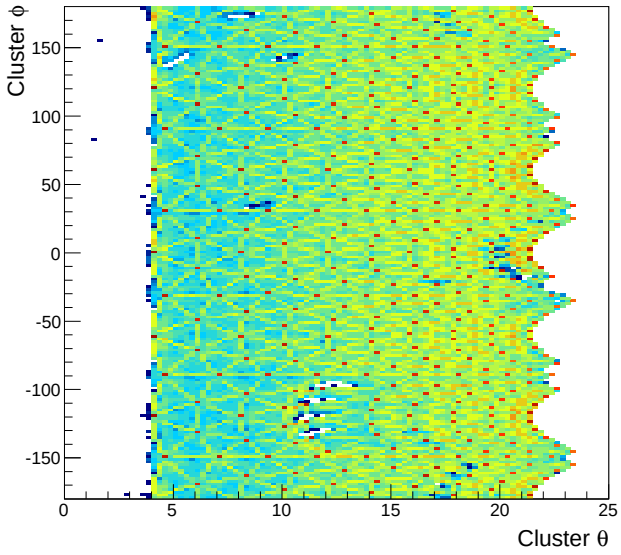

Figure 3.18: TAPS Cluster ϕ vs. θ hits distribution.

Acceptance	
Azimuthal coverage	$0° \leq \phi \leq 360°$
Polar coverage	$\sim 0° \leq \theta \leq \sim 20°$
Angular Resolution	
Azimuthal resolution	$\phi < \frac{180°}{\pi R}$ R: Radius from centre of TAPS
Polar resolution	$\theta < 1°$
Energy Resolution	
$\frac{\sigma}{E}$	$\sim \frac{3.7\%}{E_\gamma}$ $(\mathrm{GeV})^{0.25}$
Decay Timing	
σ_t^{fast}	~ 0.6 ns
σ_t^{slow}	~ 620 ns

Table 3.3: Characteristics of TAPS.

3.5 Acquisition

In general, analogue signals from the PMTs of a detector element are read out and split into three paths: one to a Charge-to-Digital converter (QDC) and the other to a discriminator that outputs a logic pulse to a Time-to-Digital converter (TDC), as well as an input to a logic circuit which triggers the event readout. Each subsystem (Crystal Ball or TAPS) will deliver a single output pulse of the logical OR of the signals of each element. These subsystem outputs are the inputs to the trigger module, which selects whether the event is accepted or rejected. Events which do

not make the acceptance criteria of the trigger module are passed to a fast clear, which resets all the QDCs and TDCs for the detector elements, making them ready for the next event. For accepted events the trigger module issues a gate over which the magnitude of the charge in the analogue pulse is converted to a digital channel in the QDCs, as well as providing a TDC signal which is then compared to the reference time for the event. The information read out from the QDCs and TDCs is passed to the Data Acquisition system (DAQ), which the AcquRoot software running on a dedicated DAQ computer then builds and stores in an event structure. During this time the system is interrupted until this process is complete, and then the QDCs and TDCs are reset for the next event.

3.5.1 Detector Electronics

Tagger

The Tagger readout is based entirely on whether individual focal plane scintillator elements are hit and the respective timing of that hit, and thus involve only TDC readout. When scintillation occurs in a focal plane element and the signal is above a preset discriminator threshold for that particular channel, the logic pulse output from the discriminator is delayed and then fed to a TDC to record the timing for that event. Counting is then stopped by a logical pulse from the experimental trigger (formed by a combination of Crystal Ball and TAPS information). The individual channel rates in the Tagger are determined by the discriminator signal being passed to scalars that accumulate without being restricted by the experimental trigger. This information can then be used to determine the total photon flux from the Tagger, which is essential for cross section measurements.

Crystal Ball

The analogue signals from the individual Crystal Ball PMTs are connected in blocks of sixteen channels. The signal is split into three outputs, which are fed into different modules: one output to a Flash QDC, the second passed through a discriminator to

a CATCH (Compass Accumulation Transfer Control Hardware) TDC and scalars, and the third sent to the trigger electronics. The Flash QDCs are set up in such a way as to sample the analogue pulses over three integrated regions in time: a region before the signal to record as the pedestal, a region over the main pulse and a region at the tail-end of the pulse. The pedestal signal for an individual channel represents the inherent electronic noise in the absence of a signal. Therefore, in order to reduce the total volume of data being taken dynamic suppression of the pedestal signals is performed within the Flash QDC modules. A schematic of the Crystal Ball electronics is shown in figure 3.19.

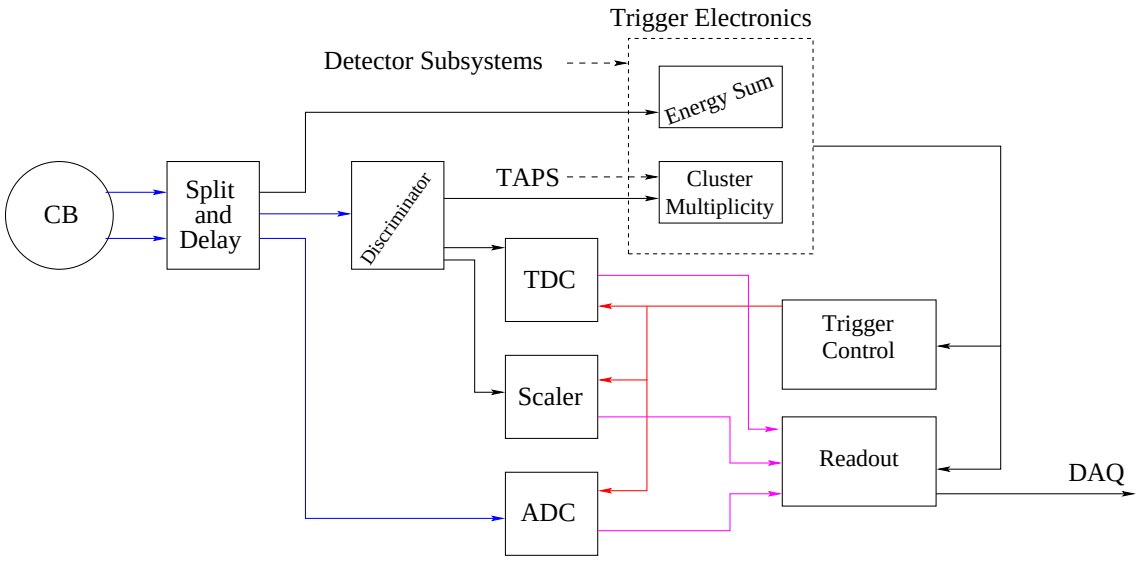

Figure 3.19: Diagram of Crystal Ball electronics

TAPS

The TAPS and Crystal Ball readouts differ as a result of the different inherent time characteristics for BaF_2 and NaI crystals, as discussed in Section 3.4. As a result, the individual TAPS PMT signals are split into three: the first to a QDC with an integration time of 40 ps (the fast component), the second to a QDC with a longer integration time of 200 ps (the slow component) and the third via a Constant Fraction Discriminator (CFD) to a TDC. A CFD rather than the more standard leading-edge discriminator is used in the TAPS readout to make better use of the excellent intrinsic timing resolution of BaF_2. The use of two QDCs per channel

with different integration times allows for pulse-shape analysis to be employed for particle identification [63].

3.5.2 Trigger

The experimental trigger is based upon two criteria that characterize any given event and determine whether the event is passed to the DAQ. The first of these is a sum of the total energy collected in the Crystal Ball. The second condition is a multiplicity trigger, which contains information on the total number of detected particles in the Crystal Ball by summing individual NaI signals into groups of sixteen and requiring that one or more such groups pass a threshold of around 40 MeV. The trigger conditions for the present beamtime were a total energy sum of 300 MeV and a multiplicity of three or more. Determining the optimum trigger conditions for a particular beamtime involves seeking a balance between a high event rate and a low DAQ deadtime (the time during which an event cannot be read out due to the DAQ processing a previous event). The experiment initially began with an energy sum of 200 MeV which was later increased to reduce the deadtime.

3.5.3 Software

AcquRoot

The primary purpose of the AcquRoot [64] software package is control of the DAQ system. Running on a dedicated DAQ computer during experimental periods it is used to coordinate the readout of the individual detector QDCs and TDCs when the trigger conditions are passed, buffering all relevant information for each event before storing it in a dedicated compressed binary format. It also handles the online monitoring of the experiment, as well as offline analysis. AcquRoot is a C++ based system, and is compiled against the CERN ROOT analysis framework [65]. It provides the user with a multitude of classes governing the read out from the various detectors, and ROOT provides many useful physics classes. This allows the user to

easily write their own analysis class and fit it into the AcquRoot framework.

Geant4 A2 Simulation

In order to simulate the A2 experiments, a detailed Monte Carlo simulation of the A2 experimental setup is used. This simulation was written in the Geant4 [58] Toolkit. The simulation provides a detailed three dimensional model of the detector systems and the ability to process events and account for different materials within the various systems, as well as different physics processes. Simulated events for a particular reaction channel can be generated using the AcquRoot event generator and processed with the Geant4 A2 simulation. The simulation tracks the particle calculating changes to the track and energy based on various cross sections associated with the materials in the system. The output of the simulation can be analysed in parallel to the data using the AcquRoot analysis package.

Chapter 4

Calibration and Event Reconstruction

Prior to any data analysis, the detector systems and their components must be calibrated in order to output useful and meaningful physics information from the raw data taken at the experimental facility. Information needs to be in three useful formats; time, position and energy. This chapter will describe the method of calibration for each detector system, with normal procedure in A2 being the splitting of the calibrations amongst different groups in the collaboration, and lead on to the event reconstruction of the reaction channel. The calibrations are used to convert information from both the QDCs and TDCs into energies and timing information. Detector hits in the Crystal Ball and TAPS are grouped using a clustering algorithm for elements read out from the same particle hit. Information passed into the data stream, in the form of Tagger, PID, Crystal Ball, TAPS Crystals and TAPS veto information, once calibrated can be used to identify desired reaction channels, including the selection of π^0's and both inclusive and exclusive event selection techniques.

4.1 Detector Calibration

4.1.1 Timing Alignment

It is essential that the timing for the elements in the detector systems is accurate since timing coincidences provide correlation for the detection systems and also for the clustering of the calorimeters discussed later. In addition to this, use of the time of flight identification technique requires precise timing. The method of aligning timing for channels is relatively generic for all the detection systems in the A2 setup, and thus only the Tagger alignment will be covered.

Each Tagger channel TDC readout can be fitted with a Gaussian, in order to determine the mean of the timing peak for each channel. By limiting the fit function to defined limits, the fit can be applied to all channels in the Tagger. This mean value can then be used to apply an offset to each channel allowing them to be aligned to an arbitrary time. Figure 4.1 shows the respective plots in the TDC alignment process for the Tagger, and the specifics of one of the uses of the timing alignment of the Tagger is covered in section 4.1.2

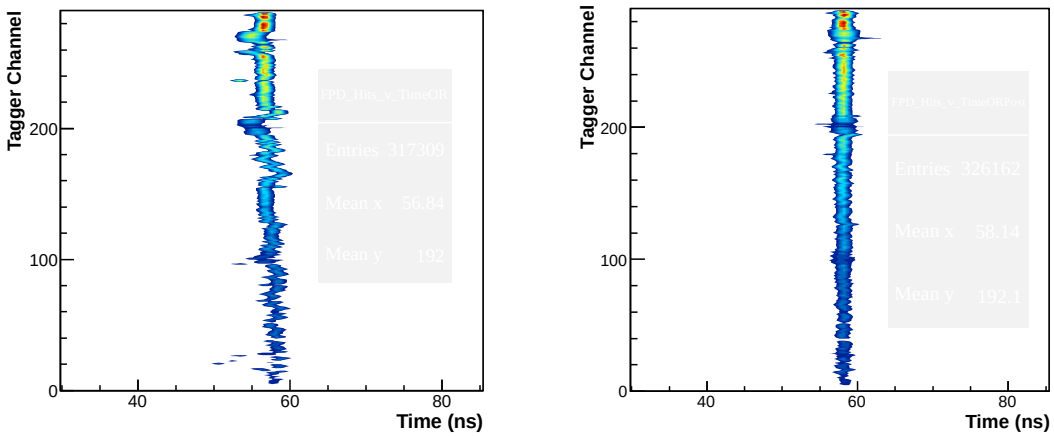

Figure 4.1: (Left) and (right) show Tagger channels vs. Time prior to and after alignment respectively. In this example the Tagger timing is aligned to 58 ns.

4.1.2 Tagger Energy Calibration

As mentioned in section 3.2, the energy of the *bremsstrahlung* beam is calculated from the MAMI incident beam energy and the lateral position on the taggers focal plane of the electron hit (see equation 3.2). The energy of the photon beam is a continuous spectrum (see figure 3.9 (b)), covering all energies up to the narrow, well defined energy of the MAMI electron beam. The measurement of the photon beam energy relies on accurate knowledge of the primary electron beam delivered by MAMI, which is defined by the number of recirculations from the microtrons. This and the measurement of the scattered electron energy are all that is needed in order to get an accurate measurement of the *bremsstrahlung* photon energy. A detailed description of how the output of MAMI is determined can be found in the Jankowiak paper [43].

Because the Tagger is a hodoscope and does not read out to QDCs, the energy of the electrons scattered in the radiator is determined by the position on the scintillator focal plane (FPD). The calibration of channel position to electron energy is described in the paper by McGeorge [48]. By the slow variation of the Taggers bending magnet, the electron beam can be scanned across the FPD elements. Because the field strength of the magnet is understood in order to dump the beam for both the MAMI-B output (855MeV) and the MAMI-C output (1508MeV), these small steps in field strength (moving away from 1.056T towards 1.833T) allow the measurement of magnetic field strengths when the electron beam is striking overlapping FPD scintillators. This element position is very well known (± 0.05 of a channel), thus it is possible to look at a channel's ID number against the field strength of the magnet. This then provides a relative measure of the Taggers channel ID number to the energy of the scattered electron.

Multiple measurements at a fixed field and varied beam energies can be seen in figure 4.3 with resulting calibration. By the use of a computer program, the calculation of the calibration was performed, based on the Tagger field map, using the basis of the main beam trajectory towards the dump. The resolution of the tagger varies over the focal plane, and is shown in figure 4.2. When the Tagger

was built, an NMR probe was installed inside. This was used in order to measure the uniform field of the magnet. As the position and angles of the FPD elements was known from the installation of the focal plane, the program could then apply a χ^2-minimisation algorithm in order to interpolate between the measured points and provide smooth function of scattered electron energy in relation to the Taggers Channel ID number.

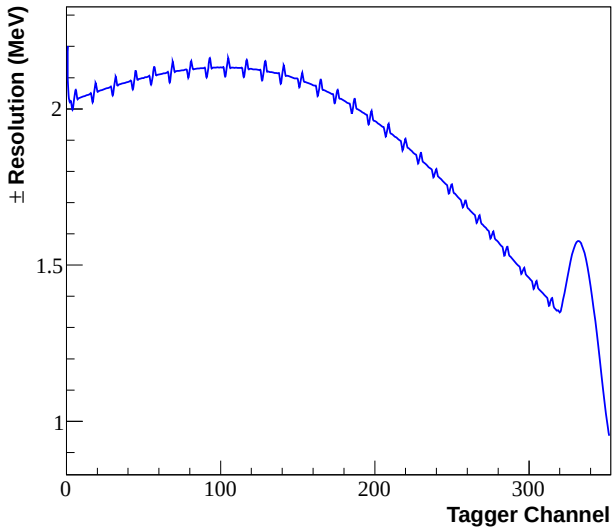

Figure 4.2: The variable Tagger resolutions across the focal plan element number.

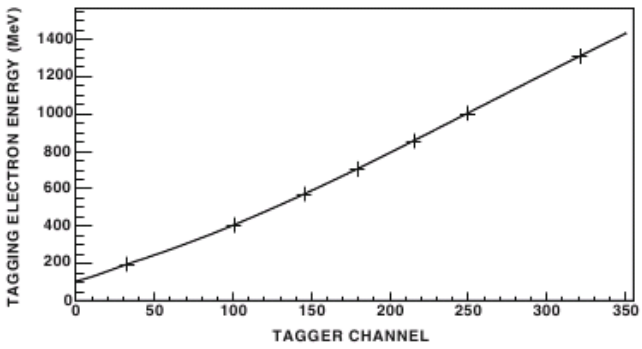

Figure 4.3: Tagged electron energy against channel ID Number [48]

Small discrepancies between the calculated and measured energies arise, due to the small screws in the upgraded magnet pole shims, producing non-uniformities in the magnetic field. These discrepancies vary from 1.5 MeV to 4 MeV across the FPD (moving from highest to lowest photon energies). The investigation of this is also

covered in the McGeorge paper [48], and a correction factor is added to the energy calibration. The Tagger energy calibration was carried out by colleagues at the University of Glasgow.

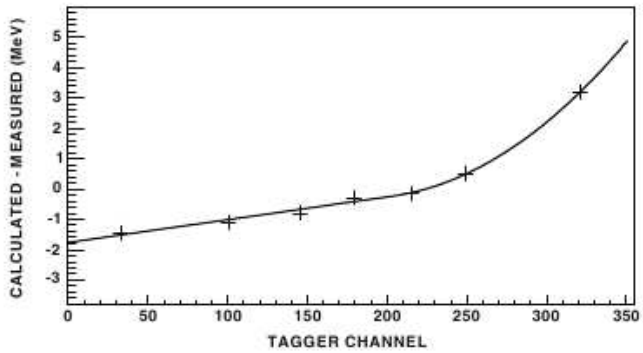

Figure 4.4: Discrepancies between calculated and measured Tagged Electron Energies against Channel ID Number [48]

Tagging Efficiency

Tagging efficiencies are used to determine the photon flux on the target, and are essential for cross section measurements, in order to normalise the yield. For polarisation experiments, the tagging efficiency has a different use, to produce enhancement plots for determining the magnitude of linear photon polarisation in the experiment. The tagging efficiency is the ratio of the number of photons that pass into the experimental area to the number of electrons in the focal plane with a relative background subtraction. Equation 4.1 shows ratio of photons to electrons in the focal plane.

$$\epsilon^{n}_{tagg} = \frac{N_{\gamma}}{N_{e^-} - N_{bg}} \tag{4.1}$$

A Pb-glass detector is used to provide the trigger for tagging efficiency, rather than the Crystal Ball. This is because using the Crystal Ball would result in the reaction cross section being folded into the tagger spectrum, which would make it difficult for the polarisation to be calculated without first accounting for this cross section. To make things simpler, the use of the Pb-glass allows the tagging efficiency to be measured without needing to account for the reaction cross section.

Due to build up of radiation on the Tagger focal plane elements, background measurements are taken with no incoming beam. These background measurements are then taken into account in the calculation of the tagging efficiency (equation 4.1). After a background measurement has been made, a measurement for each polarisation plane setting (*Parallel* and *Perpendicular*), as well as an unpolarised run, are taken. The unpolarised run is used to divide out the relative unpolarised contribution to the polarised spectra, thus producing an enhancement for degree of linear polarisation calculations (see section 3.2.1).

Prompt and Random Events

For each triggered event, there are multiple electrons detected in the Tagger focal plane counters. These events are a random background, stemming from certain interactions such as Møller scattering in the radiator, or photons that do not make it through the collimator. As detailed in section 4.1.1, the Tagger timing is aligned, giving a strong "prompt" peak around electron events that are associated with the experimental trigger. This peak sits on the relatively flat distribution of "randoms". In order to get clean event selection, this background must be subtracted from the region under the prompt peak.

As individual events on the focal plane elements cannot be determined to be prompt or random on an event by event basis, a large sample must be built up in order to define windows for deciding on prompt and random electron events. Figure 4.5 shows the sampling regions of the windows. Random windows are placed either side of the prompt peak. This is due to the fact that the background is not completely uniform, so two large samples of randoms are taken either side of the prompt peak to account for any slope in the random background when subtracting from the prompt peak.

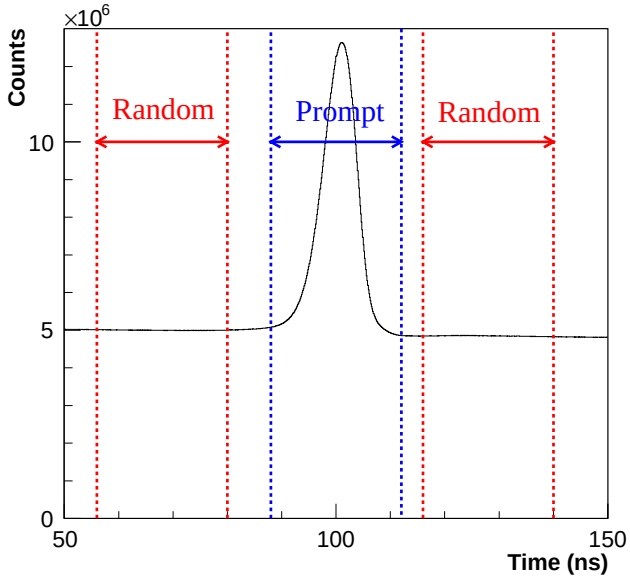

Figure 4.5: Tagger time spectrum showing the sampling of prompt (blue) and random (red) regions. Each region is a 24 nano-second sample of the time spectrum giving double the number of randoms, which is accounted for when subtracting the randoms from the prompts

4.1.3 Crystal Ball Energy Calibration

Determining a particle's energy from the Crystal Ball is complicated: different particles deposit different amounts of energy in the crystals as they traverse, or cause different numbers of crystals to fire. A particle's energy is determined firstly on the basis of the energy calibrations of the crystals, and secondly on the identification of the cluster and finally adjusted with a constant to account for the particle type. Calibration of the Crystal Ball involves getting a meaningful output in MeV from the QDCs. In order to calibrate the Crystal Ball for photonuclear reactions, more detail was required as particles such as the neutral pion will deposit more energy (typically greater than 40MeV) creating a cluster of many crystals in the ball, as outlined in section 4.1.6.

Before performing an energy calibration, alignment of the high voltages for the Crystal Ball PMTs needs to be performed. An $^{241}Am/^{9}Be$ source was placed at the centre of the Crystal Ball. The subsequent reaction chain of the α decay of Americium ends with $^{*12}C \rightarrow ^{12}C\gamma$, the decay photon being of low energy (4.43MeV). By

detecting a photon in each crystal, the high voltage on each PMT was adjusted until the peak from the photon in each crystal was aligned to the same position for each element.

An excellent source for providing a detailed energy calibration is the $\gamma p \rightarrow \pi^0 p$ reaction, as this channel is very well determined and understood. Using the beam energy and the emission angle of the π^0, the expected energy of the γ's from the $\pi^0 \rightarrow \gamma\gamma$ decay can be calculated, and the comparison of the signal output to this calculation can be used for the calibration. It is necessary to calibrate the output on a crystal-by-crystal basis, and as such the use of events where a large amount of the initial energy deposited in the cluster ($\sim$70%) is in the central crystal. These events are used to adjust the MeV per channel gain of each crystal element such that the output is aligned to the π^0 mass peak of $\sim$134.97 MeV/c^2. Such an adjustment will affect the central crystals neighbors, and as such an iterative process is used on the neighbors until the signal alignment converges and the output peak is steady on $\sim$134.97 MeV/c^2.

$$V_2 = \frac{M_{\gamma\gamma}}{M_{\pi^0}} V_1 \tag{4.2}$$

Equation 4.2 illustrates how the iterative process works in adjustment of the gain factor for each element using the π^0 mass. V_2 is the new factor, and V_1 is the gain factor from the previous iteration. $M_{\gamma\gamma}$ and M_{π^0} are the invariant mass of the detected photons and the PDG invariant mass of the π^0 respectively. Table 3.3 in the previous chapter shows the angular and energy resolutions of the Crystal Ball. The Crystal Ball energy calibration was carried out by colleagues at the University of California [66].

4.1.4 Particle Identification Detector Calibration

Azimuthal Channel Alignment

As mentioned in section 3.3.1, charged particles are identified using the EΔE technique, where a small amount of energy (ΔE) is deposited by charged particles passing

through a PID element in coincidence with total energy (E) deposition in the Crystal Ball. The azimuthal alignment of each of the twenty four elements is very important for charged particle detection.

Selecting events where a minimum of a single hit is registered in the PID, and looking at this against the azimuthal distribution in the Crystal Ball and taking a projection for each element of the PID, a peak for charged particles can be seen. This is shown in figure 4.6. The width of this peak is restricted to the width of a PID channel. By fitting a Gaussian distribution for each element, the azimuthal position of each PID channel can be determined by the mean of the fit. The smaller, broader peak on the left plot in figure 4.6 is indicative of lighter charged particles (generally $\pi^{\pm}$'s) depositing energy in the PID channel. These events are from coplanar events from other reaction channels such as $\gamma p \rightarrow \pi^{+} n$.

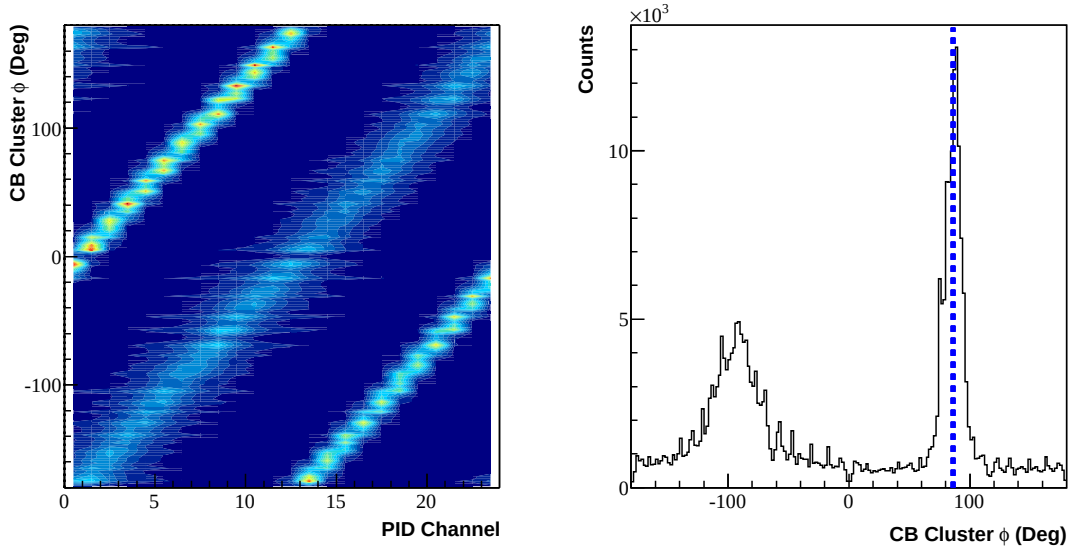

Figure 4.6: Correlation used to project the azimuthal angle of PID channels (right). The sharp peak is proton clusters in the Crystal Ball with a coincident PID hit (left), with a broader coincident $\pi^{\pm}$ peak.

Energy Calibration

Energy calibrations of the PID are normally carried out using a combination of information in the Crystal Ball and the PID. Because of the presence of the Polarimeter,

reconstructed proton energy from the π^0 was used to perform the energy calculation. This will be covered in section 4.2. By considering the energy in a PID element against the reconstructed energy in the Crystal Ball (Figure 4.15), projections can be taken of the energy deposition in the PID element. A total energy range is chosen for each channel, and a projection of the energy deposited in the PID element for that range is taken. A fit to this energy is then matched to a simulated energy. A more detailed description of this method can be found in reference [67]. PID calibrations were carried out by colleagues at the University of Edinburgh.

4.1.5 TAPS Energy Calibration

Initial high voltage alignment of the BaF_2 elements was set using cosmic muons. Using the minimum ionising peak of the cosmic muons (37.7 MeV), the gain for each channel could be aligned. Similar to the Crystal Ball, the energy calibration of the BaF_2 elements of TAPS were calibrated using $\gamma p \rightarrow \pi^0 p$ reactions. After the Crystal Ball energy calibration has been performed, the π^0 invariant mass is plotted where a single decay photon from the $\pi^0 \rightarrow \gamma\gamma$ is detected in the Crystal Ball, and a second is detected in TAPS. It is then a case of adjusting the gain of the element (MeV/channel) until the π^0 invariant mass peak is adjusted to the accepted PDG mass. This requires several iterations for all crystals, until the gain for each channel is set to output accurately defined photon energies. The algorithm for clustering is the same as the CB, and is explained in detail in section 4.1.6. The Veto caps for each crystal are calibrated in the same was as the PID, however as they are located after the polarimeter, they can use the energy from the proton as opposed to that of the reconstructed energy from the π^0. Calibration of the TAPS detector was carried out by colleagues at the University of Gieβen [68], and details of the angular and energy resolutions of TAPS can be found in table 3.4.

4.1.6 Clustering

Energetic particles produce a shower of electromagnetic particles in an individual crystal in a highly segmented calorimeter, such as the Crystal Ball or TAPS. This shower will generally spread to surrounding crystals, depositing its energy over several crystals, forming what is known as a cluster. Different particles will produce relatively unique cluster signatures, with differing numbers of crystals scintillating with different energy spreads. Use of a clustering algorithm allows these crystal clusters to be grouped into energy depositions which are caused by the original incident particle. Photons entering the Crystal Ball will generally cause a shower which will spread to an excess of 10 NaI Crystals (∼98% of the time) depositing all their energy within a cluster of this size. However, protons will tend to deposit their energy contained to ∼2-3 neighboring crystals.

The clustering algorithm attempts to find the crystal with the highest energy deposition, and then treats this as the central crystal within the cluster. It then proceeds to check energy deposition in the nearest neighboring crystals, adding them to the sum of the energy. This provides a total energy in a cluster, as well as a count of the number crystals in the cluster (see figure 4.7). The sum of the energy is simply given as $E_{sum} = \Sigma_n E_n$ where E_n is the energy for the n^{th} crystal. Subsequent clusters are accepted or rejected based on energy threshold of 15 MeV. The relative position of the particle is also supplied by the clustering algorithm. This position is calculated as a weighted mean of the individual crystals positions within the cluster.

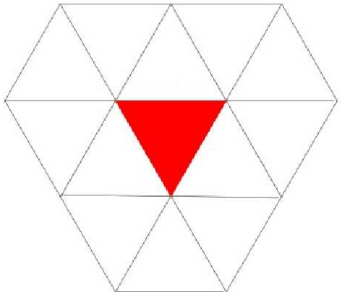

Figure 4.7: Schematic of an NaI cluster supplied by the clustering algorithm, showing the central energy crystal and its neighbors

$$r_{mean} = \frac{\Sigma_n r_n \sqrt{E_n}}{\Sigma_n \sqrt{E_n}} \tag{4.3}$$

Where r_n is the coordinate position of the n^{th} crystal, and E_n is again the energy of the n^{th} crystal.

4.2 Event Reconstruction

The calibration constants are applied to the raw signals to produce the energies, times, angles and positions which allow particles to be identified and constructed as Lorentz vectors (also called relativistic 4-vectors). This section will cover the necessary steps to reconstruct the $\gamma p \rightarrow \pi^0 p$ reaction. A cut on cluster multiplicity is first applied to reduce the event sample into the initial most probable events. After a π^0 has been selected these reconstructed 4-vectors can be identified in the analysis using the information from the various detectors and can then be used to select reaction channels. This analysis starts by assuming all clusters are photons, and is split into two separate event reconstructions: an inclusive reconstruction for the extraction of the Σ observables and an exclusive reconstruction for the extraction of the O_x and T observables.

The photon 4-vector from the Tagger which is assumed to induce a reaction in the target is selected. This interaction will produce a shower of different particles from a variety of competing mechanisms. This analysis concerns the selection of a meson, specifically a π^0, and a proton. The proton is scattered in the carbon Polarimeter, and its scattering angle is calculated. The analysis concerning the scattered proton is covered in section 4.2.4.

Initial constraints are placed on the number of detected particles in the final state, followed by the reconstruction and selection of a π^0. An inclusive selection of events is studied with the reconstruction (rather than explicit detection) of a proton in order to select the $\gamma p \rightarrow \pi^0 p$ reaction channel, with several constraints placed on different factors such as mass and energy. Finally a proton scattered in the carbon analyzer

is selected from the available vectors as a final step in the exclusive analysis for the beam recoil observable extraction (Chapter 5). Figure 4.8 is a diagram showing the final detected states in black.

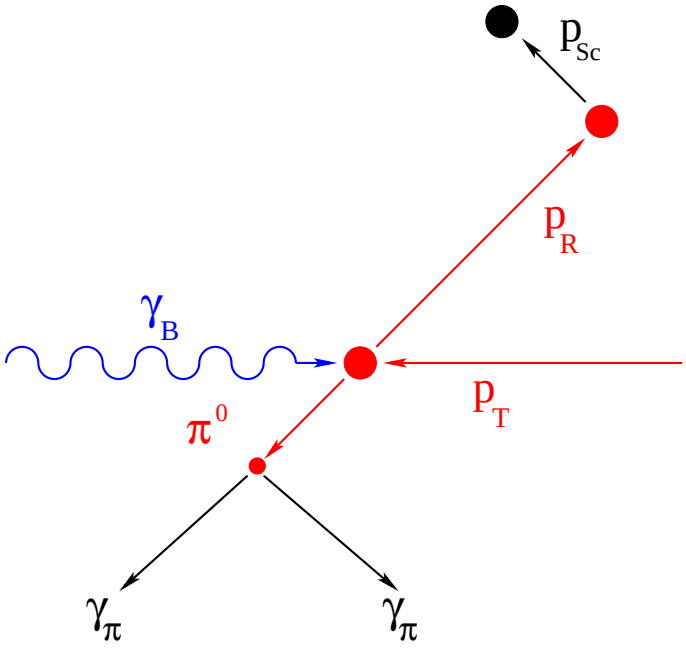

Figure 4.8: Diagram of the $\gamma p \rightarrow \pi^0 p$ reaction, where p_T is the target proton, γ_B is the tagged beam photon, p_R is the recoiling proton. The γ_π are the decay photons from the π^0 and p_{Sc} is the proton scattered in the polarimeter.

4.2.1 Cluster Multiplicity

Before the selection of the π^0 event, a cut is placed on cluster multiplicity. As the reaction channel $\gamma p \rightarrow \pi^0 p$ has a π^0 which decays to two photons ($\pi^0 \rightarrow \gamma\gamma$) in the final state, it is reasonable to expect events with a total of three clusters in the calorimeters to be the events which should be examined for this reaction. The reconstruction of the π^0 from the two decay photons is covered in the following section. While it would be possible to extract meaningful data when demanding three or greater clusters, the inherent problem with extracting the $\pi^0 p$ channel from competing processes and eliminating false clusters due to hadronic split-off within the crystals would not be worth the statistical gain, as seen in figure 4.9.

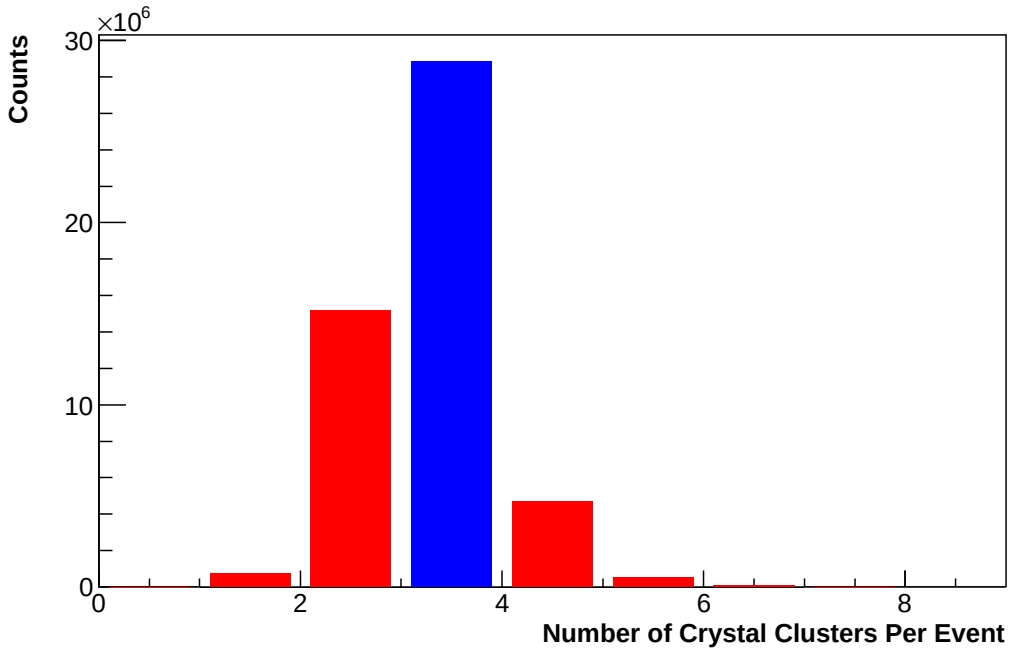

Figure 4.9: Number of events for different cluster multiplicity in the Calorimeters

4.2.2 Selection of π^0's

The π^0 is the lightest bound meson and does not decay via the strong force. Instead it decays via the electromagnetic interaction ($\pi^0 \rightarrow \gamma\gamma$) with a branching ratio of $\sim$99% [12]. Because the π^0 has such a short lifetime ($8.4 \times 10^{-17} s$), it is impossible to detect the π^0 directly, as it will travel the order of nanometers before its decay. Thus, the π^0 must be inferred and selected from the detection of the two decay photons. When energy and position of the two decay photons can be reconstructed, it is possible to calculate the mass of a combination of two photons with the following equation:

$$M_{\gamma\gamma} = \sqrt{2E_{\gamma_1}E_{\gamma_2}(1 - cos\psi)} \tag{4.4}$$

Where E_{γ_1} and E_{γ_2} are the detected energies of the respective photons, and ψ is the angle between the two detected photons.

It is not just the π^0 that can be reconstructed from two decay photons. There is another dominant process of two photon decay, that of the η. The difference in mass of these two particles makes it easy to separate the two mesons (M_{π^0}: 134.97 MeV,

M_η: 547.72 MeV). The 4-vectors for the two photons can be reconstructed from the clusters in the calorimeters:

$$p_{\gamma_1} = (\overrightarrow{p}_{\gamma_1}, E_{\gamma_1}) \tag{4.5}$$

$$p_{\gamma_2} = (\overrightarrow{p}_{\gamma_2}, E_{\gamma_2}) \tag{4.6}$$

where $\overrightarrow{p}_{\gamma_n}$ is the momentum vector of the (x, y, z) components of the γ_n's momentum, and E_{γ_n} is the respective photons energy. Then the reconstruction of the π^0 4-vector is as follows:

$$p_{\pi^0} = p_{\gamma_1} + p_{\gamma_2} \tag{4.7}$$

Before the actual reconstruction of the π^0 can be carried out, the two photons must be identified from the three clusters that were previously demanded (section 4.2.1). Each 4-vector corresponding to a cluster is initially assumed to be a photon. These "photons" are then processed through a sorting function:

- Get all possible unique combinations of 4-vectors.
- Create candidate 4-vectors by combining unique combinations.
- Subtract the PDG mass of the π^0 from the mass of the candidate 4-vectors, creating mass differences.
- Sort the mass difference in order of lowest to highest.
- Use the lowest mass difference to select the two optimum photons.

This provides two 4-vectors in an event that make up the best possible π^0 and a candidate proton 4-vector to be used in the selection of scattered protons. As a cross-check the two photon 4-vectors are examined for a PID coincidence in order to eliminate a possible charge coincidence in the Crystal Ball, and the charged or neutral condition in TAPS mentioned in section 3.4. The charge or neutral condition monitors whether a vector from the BaF_2 crystal has associated veto event, labeling the vector either charged or neutral.

4.2.3 Inclusive Event Reconstruction

The inclusive event reconstruction only requires the detection of the two π^0 decay photons to identify the reaction. In order to reconstruct the reaction, the following information is required:

- The 4-vector of the Tagged photon from the beam: $\overrightarrow{p}_{tagged}$
- The 4-vector of the target: $\overrightarrow{p}_{target}$
- The 4-vector of the π^0: $\overrightarrow{p}_{\pi^0}$

$\overrightarrow{p}_{tagged}$ is provided by the Tagger, and $\overrightarrow{p}_{\pi^0}$ is selected using the information discussed in section 4.2.2. Figure 4.10 shows the invariant mass drawn from the selected π^0's 4-vector. A clear peak can be seen around the mass of the π^0. In order to select a π^0 event, a cut was placed on the mass between 98 MeV and 171 MeV, which was three σ of a Gaussian fitted to the π^0 peak. Figure 4.11 shows the angular distributions of the selected π^0, with the regions of acceptance loss due to the steel rim of the Crystal Ball hemispheres highlighted (section 3.3).

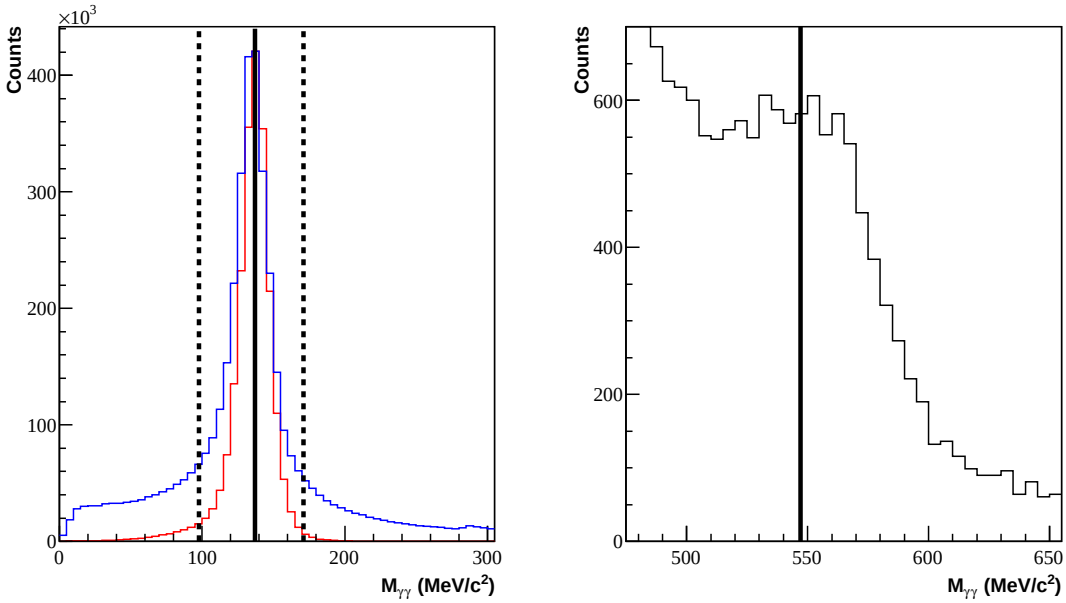

Figure 4.10: (Left)Invariant mass of the π^0 reconstructed from the two selected photons. Simulated (red) and data (blue). The dashed lines indicate the three σ cut on the peak, and the solid line indicates the PDG mass of the π^0. (Right) The η peak present with the PDG mass of the η indicated by the solid line.

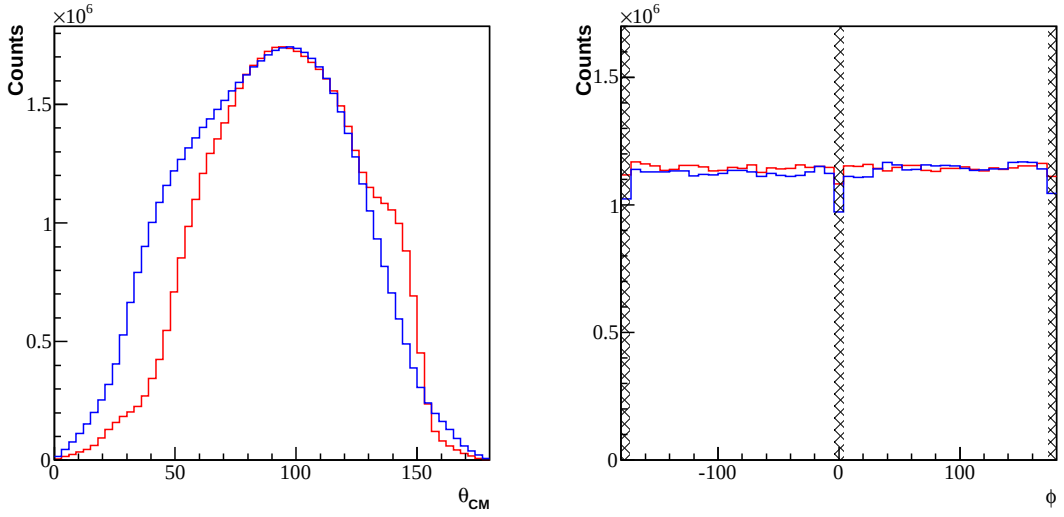

Figure 4.11: The angular distributions of the π^0. (Left) the θ distribution in the centre of mass. (Right) the ϕ distribution, the hatched regions indicate the loss of acceptance due to the steel rim of the hemispheres of the Crystal Ball. The data is shown in blue compared to the simulation in red.

Once the invariant mass cut has been made, the π^0's in the selected range are assigned the PDG mass. Now the reaction can be reconstructed by reconstructing a proton. As the inclusive analysis does not explicitly require detection of the proton, the following relation is used to reconstruct the proton using the missing mass technique:

$$\overrightarrow{p}_{recon} = \overrightarrow{p}_{tagged} + \overrightarrow{p}_{target} - \overrightarrow{p}_{\pi^0} \tag{4.8}$$

Figure 4.12 shows the reaction missing mass following identification of a π^0, with a clean peak around 938 MeV/c^2. It also shows the background of the missing mass, with a clear peak at ∼1300 MeV/c^2. This peak is predominantly from the $\gamma p \rightarrow \pi^+\pi^0 n$ channel. The elimination of these events is discussed later in this section. Unlike the two photon invariant mass for π^0 identification, where it is effective to use a cut on the mass of the pion, due to the energy of the tagged photon associated with the reconstruction of the proton different cuts must be applied. Figure 4.13 shows how the missing mass broadens with beam energy and the fits in two different beam energy regions. In order not to accept increasing amounts of

background at low energies, an energy dependent cut was applied to the missing mass, ranging from $857 < M_{missing} < 1010$ MeV/c^2 at the lowest beam energies and $829 < M_{missing} < 1029$ MeV/c^2 at the highest beam energies. These cuts were calculated by fitting a Gaussian to the missing mass at different photon beam energies.

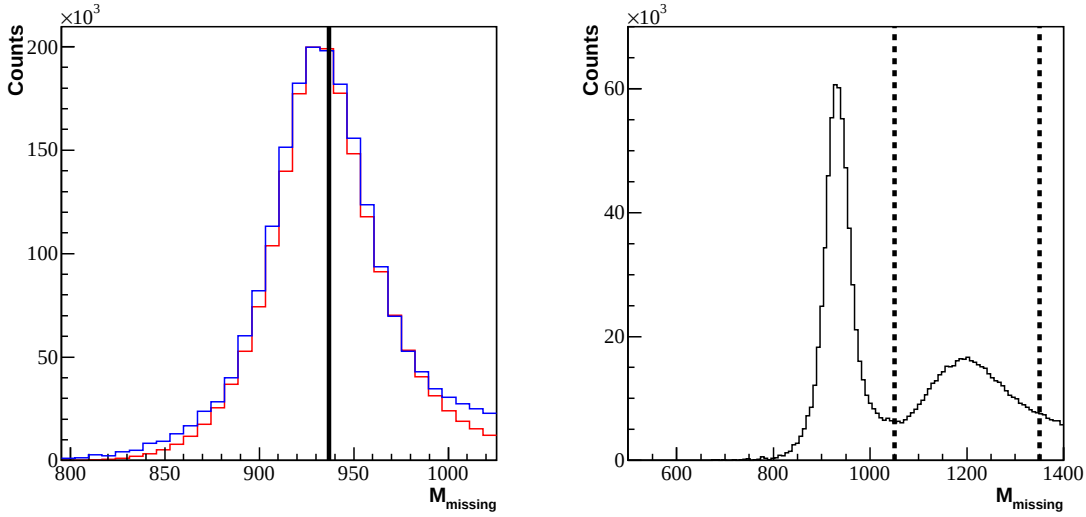

Figure 4.12: (Left) Missing mass of the reaction using the reconstructed π^0. Simulated (red) and data (blue). (Right) The same plot with the background peak shown.

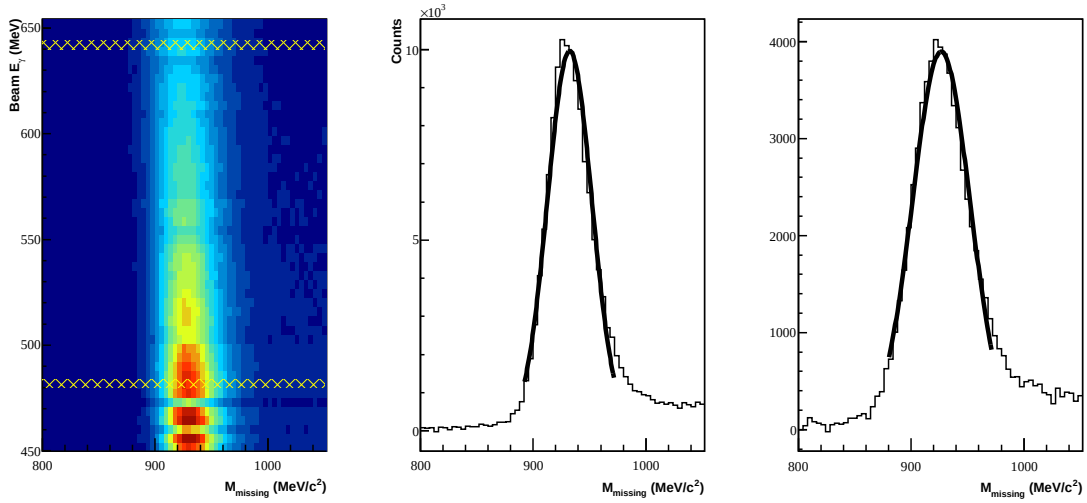

Figure 4.13: (Left) Missing mass of the reaction against beam energy showing the broadening effect due to beam energy with regions indicating where projections (middle) and (right) were taken. The σ of the fits was (middle) $\sigma = 19.3$ MeV/c^2 and (right) $\sigma = 25.8$ MeV/c^2 show a clear broadening as energy increases.

Figure 4.14 shows the angular distribution of the reconstructed proton with regions of acceptance loss highlighted in the ϕ distribution. The discrepancy between the simulation and data in θ is related to the background shown in figure 4.12, the exclusion of which is covered in the following part of this section. The next step in the inclusive event reconstruction is to check the coplanarity of hits in the PID and the reconstructed proton, as well as the EΔE technique on the associated energies. As mentioned in section 4.1.4 the polarimeter violates the EΔE with the Crystal Ball due to the scattering of the proton (Figure 4.15(left)). Instead, a reconstructed EΔE is performed. Figure 4.15 shows reconstructed proton energy against the energy deposited in the PID.

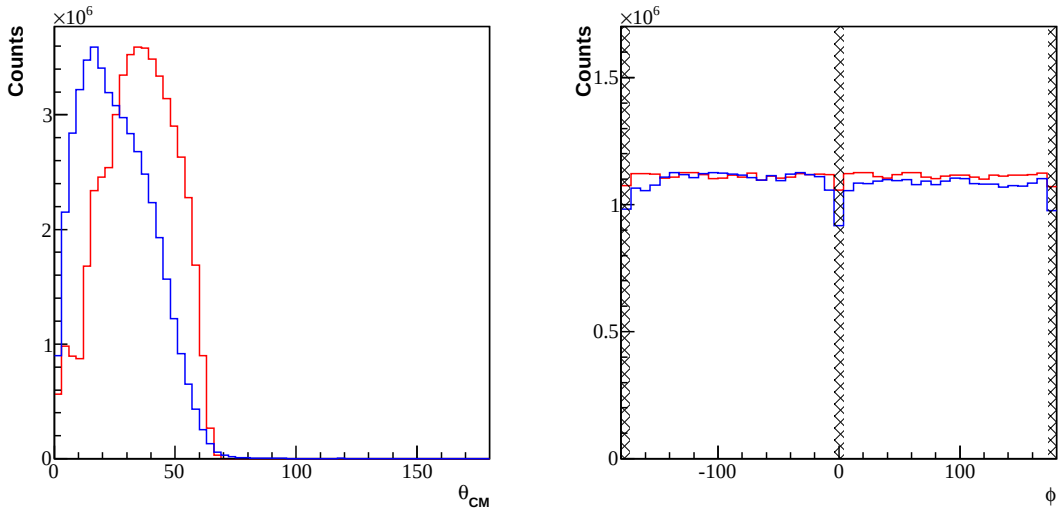

Figure 4.14: The angular distributions of the reconstructed proton. (Left) The θ distribution in the centre of mass, and (right) the ϕ distribution with the regions of acceptance loss highlighted.

The proton band can be seen, highlighted inside the polygonal region. Along the base of figure 4.15(middle) there is a lighter charged particle background. This background can be excluded by applying the region cut in figure 4.15(bottom). This cut effectively eliminates the misidentification of π^+'s as protons from the $\gamma p \rightarrow \pi^+\pi^0 n$ reaction. Figure 4.16 shows the reconstructed mass of the proton against the photon beam energy before and after the reconstructed EΔE cuts are applied.

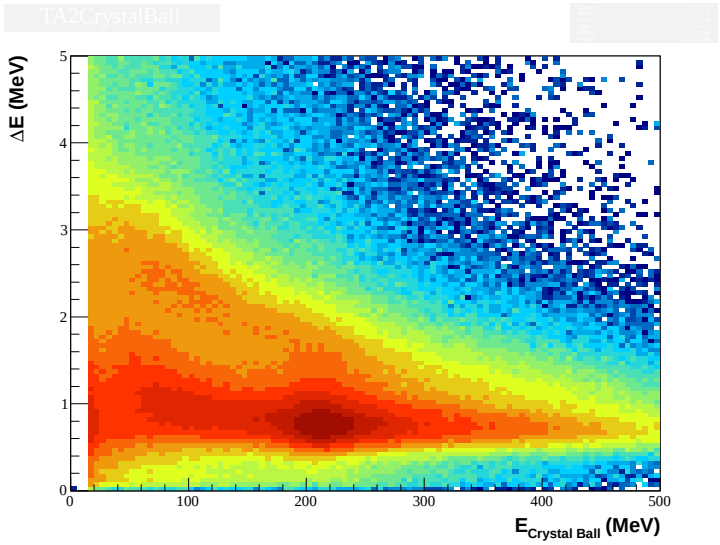

(a) Standard EΔE with the polarimeter in place

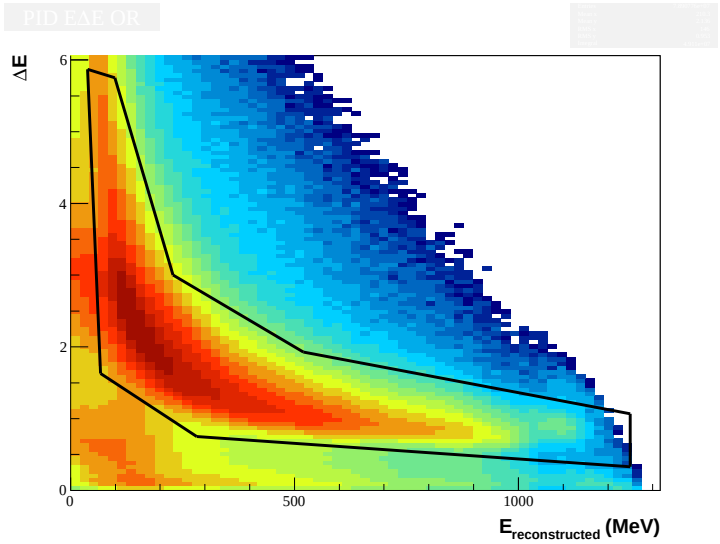

(b) Reconstructed proton energy against energy in the PID

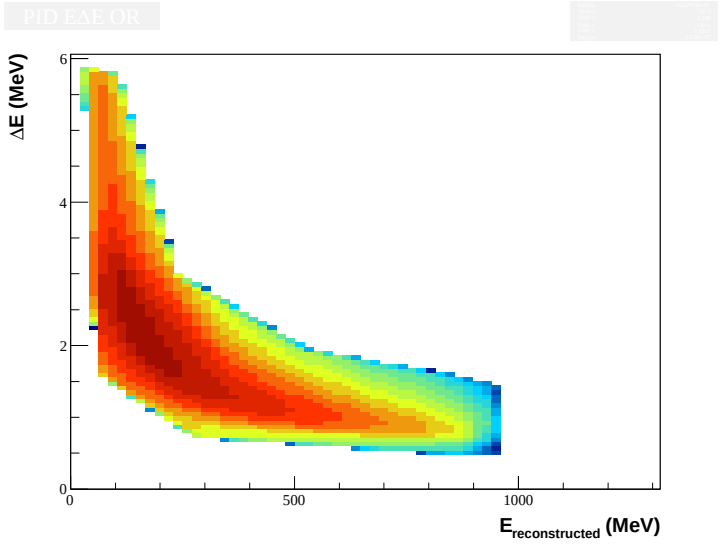

(c) Reconstructed proton energy against energy in the PID after a polygon region has been isolated

Figure 4.15: Reconstruction of the EΔE plots. The top plot should be compared with a typical EΔE (figure 3.15(right)). The middle and bottom show the reconstructed energy with an exclusion region.

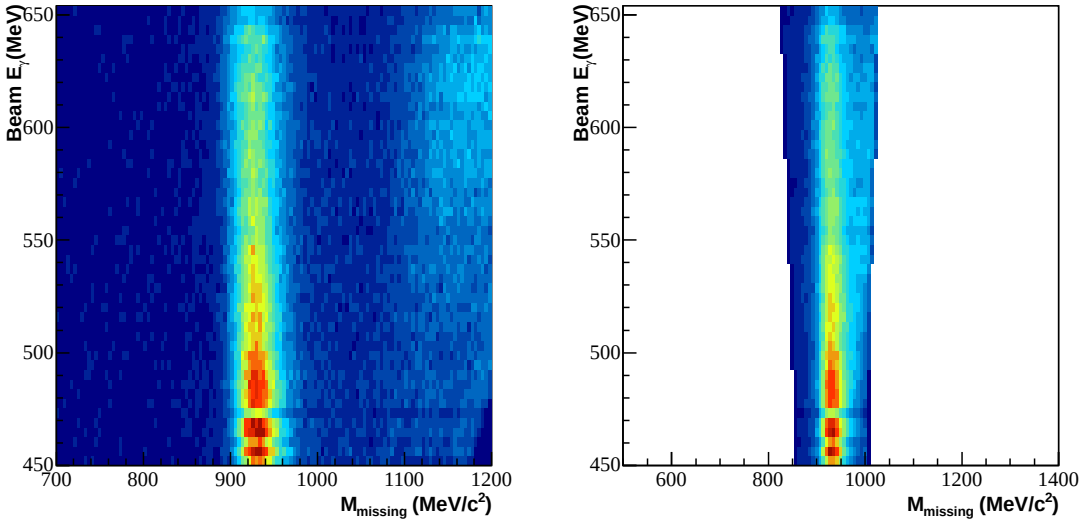

Figure 4.16: Missing mass after the reconstructed PID cuts. (left) Before the PID cuts are applied, and (right) after the PID cuts are applied. (right) Shows a much cleaner signal with no hint of the $\gamma p \rightarrow \pi^+\pi^0 n$ contamination.

At this stage, the inclusive analysis has provided enough kinematic information on the $\gamma p \rightarrow \pi^0 p$ reaction that the Σ observable can be extracted. This is covered in the following chapter (section 5.2). In order to do this a cut must be placed on the coherent peak in the photon beam energy spectrum. Figure 4.17 shows the cut placed on the coherent peak ($450 < E_\gamma < 650$ MeV) which is based on the enhancement plot shown previously in figure 3.9, as well as the modulation which the linearly polarized photons induce in the meson ϕ emission. This is covered in more detail in the following chapter.

4.2.4 Proton Scattering Angle

In order to perform recoil polarimetry measurements, it is necessary to exclusively detect the scattered proton as well as have a reconstruction of it. Both the reconstructed vectors and the scattered vector are needed in order to measure the scattering angle. This section describes the detection of the proton, and the reconstruction of the scattering angle.

Following the inclusive event reconstruction in the previous section, for the extrac-

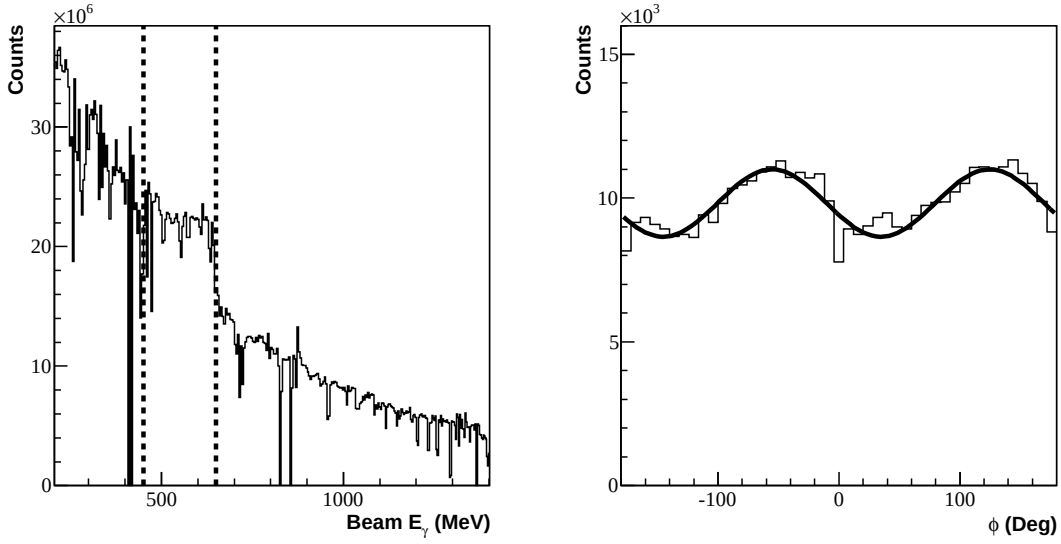

Figure 4.17: Modulation of the π^0 ϕ distribution from linearly polarized photons. (left) Shows the cut placed on the photon beam energy, (right) shows the enhanced $cos(2\phi)$ modulation of the π^0 ϕ distribution from the linearly polarized photons.

tion of O_x and T it is necessary to include the proton. Figure 4.19 shows the necessary information to obtain the proton scattering angle in the carbon.

The candidate proton ($\overrightarrow{p}_{detect}$) that was left over from the sort photon routine (Section 4.2.2) is detected and its angular information is given by the position in the calorimeters. All events are reconstructed to the centre of the target cell due to the lack of vertex information from a tracking detection system.

The reconstructed proton has all the information we need from inclusive event reconstruction, similarly its position is reconstructed from the π^0.

These two vectors are required to calculate the scattering vector. First step is to consider whether the scattered vector originated in the forward plug or the sheath of the Polarimeter, as the calculation of the scattered angle differs geometrically. If the reconstructed proton has an angle in the lab $\theta_{recon} < 18^\circ$ it is considered to have scattered in the forward plug. In this case, a cut on the kinetic energy of the reconstructed proton of 150 MeV is used, as this is the stopping power of the forward plug for protons. On the other hand, if the reconstructed proton has $\theta_{recon} > 24^\circ$ the cut on the kinetic energy of the reconstructed proton is set to 100 MeV, the

stopping power of sheath of the Polarimeter.

It should be noted that the forced 6° loss of acceptance is to exclude events that may scatter in the steel region around the exit hole of the Crystal Ball, as well as a partial cluster in the Crystal Ball in the crystals around the exit hole.

Now that it has been established whether the proton has scattered into the Crystal Ball or TAPS, the scattering angle can be calculated. A position vector, $\overrightarrow{v}_{recon}$, is calculated from the reconstructed vector. Due to the lack of tracking detectors, the scattering is assumed to occur at the centre point of the polarimeter.

$$\overrightarrow{v}_{recon} = \hat{p}_{recon} \cdot \frac{8.25cm}{sin(\theta_{recon})} : \quad \text{Crystal Ball} \tag{4.9}$$

$$\overrightarrow{v}_{recon} = \hat{p}_{recon} \cdot \frac{31.5cm}{cos(\theta_{recon})} : \quad \text{TAPS} \tag{4.10}$$

A position vector for the detected vector is also calculated by multiplying the unit vector by the radius from the target to the Calorimeter:

$$\overrightarrow{v}_{detect} = 49cm \cdot \hat{p}_{detect} : \quad \text{Crystal Ball} \tag{4.11}$$

$$\overrightarrow{v}_{detect} = \frac{173cm}{cos(\theta_{detect})} \cdot \hat{p}_{detect} : \quad \text{TAPS} \tag{4.12}$$

Unlike the Crystal Ball's curved inner face, the dependence on the length of the vector to the face of TAPS on θ_{detect} needs to be accounted for, as in equation 4.12. Once these position vectors have been calculated the calculation of the scattered vector is simply:

$$\overrightarrow{v}_{scatter} = \overrightarrow{v}_{detect} - \overrightarrow{v}_{recon} \tag{4.13}$$

Figure 4.18 shows the polar scattering angles for both calorimeters.

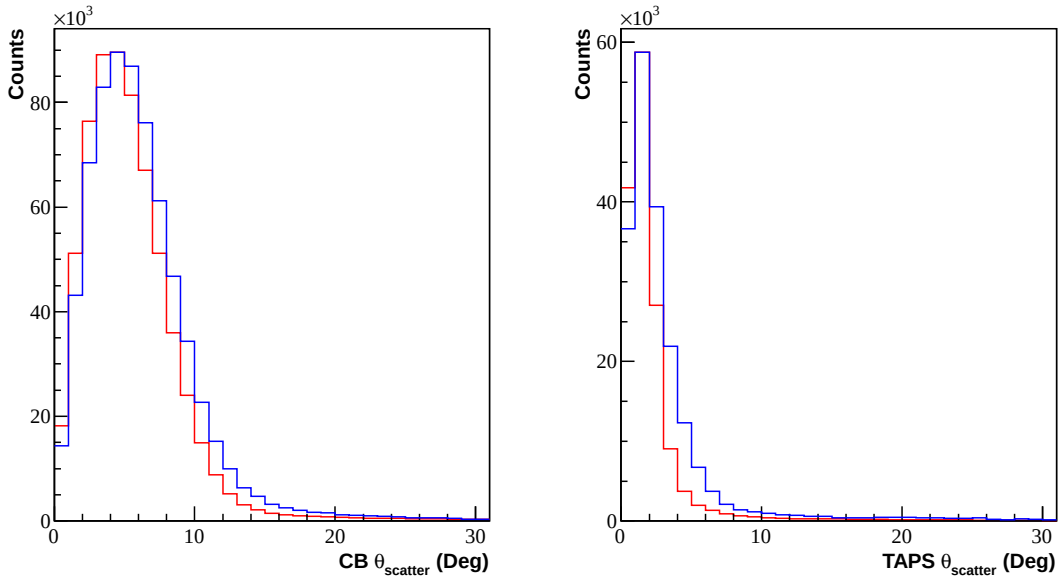

Figure 4.18: $\theta_{scatter}$ for both calorimeters. (a) The Crystal Ball and (b) TAPS. Red is the simulation and blue is the data.

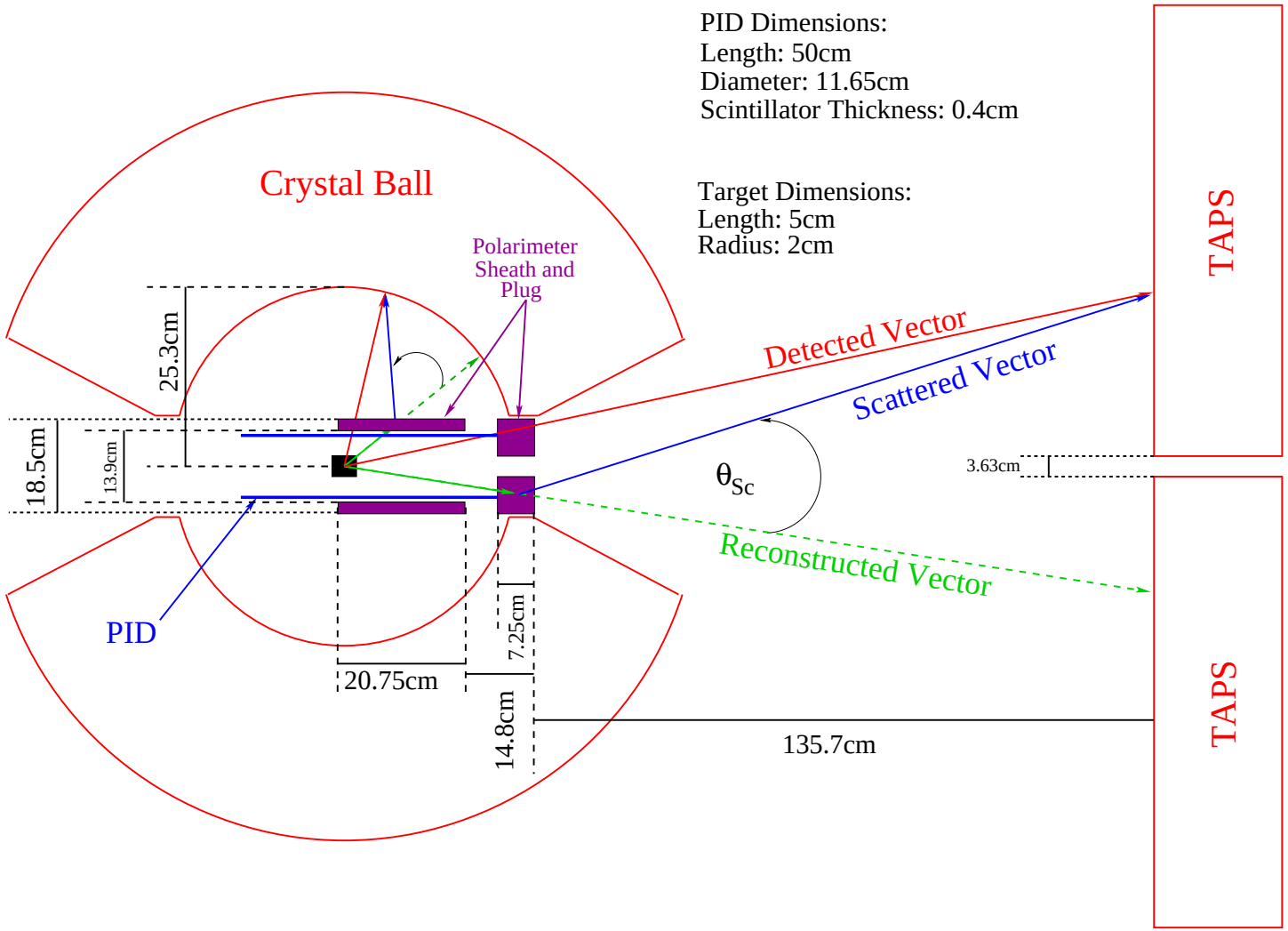

Figure 4.19: Setup of the Polarimeter in the Crystal Ball and TAPS configuration, showing the vectors necessary to calculate the scattering angle.

Chapter 5

Extraction of Observables

This chapter will describe the process of polarisation observable extraction from the event reconstruction that was described in the previous chapter. Observables are extracted by means of an asymmetry in the azimuthal angles of the respective particle, Σ being extracted from the π^0's azimuthal angle in the centre of mass system, and O_x and T being extracted from the azimuthal proton scattering angle with respect to the carbon Polarimeter.

5.1 Determining the Degree of Linearly Polarised Photons

The observables measured in this thesis are a result of polarisation induced or transferred from a linearly polarized photon beam. As such it is necessary to calculate the degree of linear polarisation in order to extract meaningful values for the observables. There is no dedicated photon beam polarimeter in the A2 setup, meaning that the degree of linear polarisation must be calculated from the available information. As discussed in section 3.2, an enhancement is produced by dividing the incoherent contribution out from the polarized photon energy distribution. By then applying a fit to the resulting enhancement distribution the degree of linear polarisation as a function of photon energy can be extracted.

Previous experiments have used the Analytic Bremsstrahlung Calculation (AnB) [54] to perform the fit and polarisation extraction. There are, however, a number of problems with the AnB calculation. The actual fit to the enhancement from which the calculation of the polarisation is based is done more or less by eye, coupled with the fact that there are many free parameters involved in the fit-by-eye procedure. A typical enhancement distribution is far from smooth, and the "best fit" often does not match the data around important regions such as the coherent peak. This is clearly demonstrated in the enhancement and associated fit shown previously in figure 3.10. One further disadvantage associated with the AnB method is that it is far from straightforward to estimate the systematic uncertainty on the degree of linear polarisation as a result of its fit-by-eye nature. In addition to this, there are a number of assumptions made in the calculation such as the spatial and angular spread of the beam, as well as how efficiently the beam is collimated.

Rather than relying on the AnB method, the present analysis uses a new fit function developed at Glasgow University [69]. This new phenomenological technique uses the fact that the enhancement can be broken down into three contributing factors: one from the primary crystal lattice vector (the large peak region), one from the second crystal lattice vector (the smaller peak region at higher energy), and the other from the residual sum of the small coherent contributions from the rest of the crystal lattice. As defined in Timm [50], the coherent contribution from each lattice vector is well understood. A typical example of this fit can be seen in figure 5.1. The major advantage of this new technique over the AnB method is the more rigorous estimation of systematic uncertainty that it allows.

It has been possible to test these two methods of extracting polarisation using data from previous experimental run periods. This involves utilising coherent π^0 photoproduction from certain nuclear targets. In this process $\Sigma(\gamma, \pi^0) = 1$ [70, 71], meaning that the extraction of this observable is equivalent to an extraction of the degree of linear photon polarisation. For this process to be valid, a spin-zero target nucleus such as ^{12}C is required. Such data have been used to test the robustness of the new phenomenological fit against the AnB fit [69]. An example comparison be-

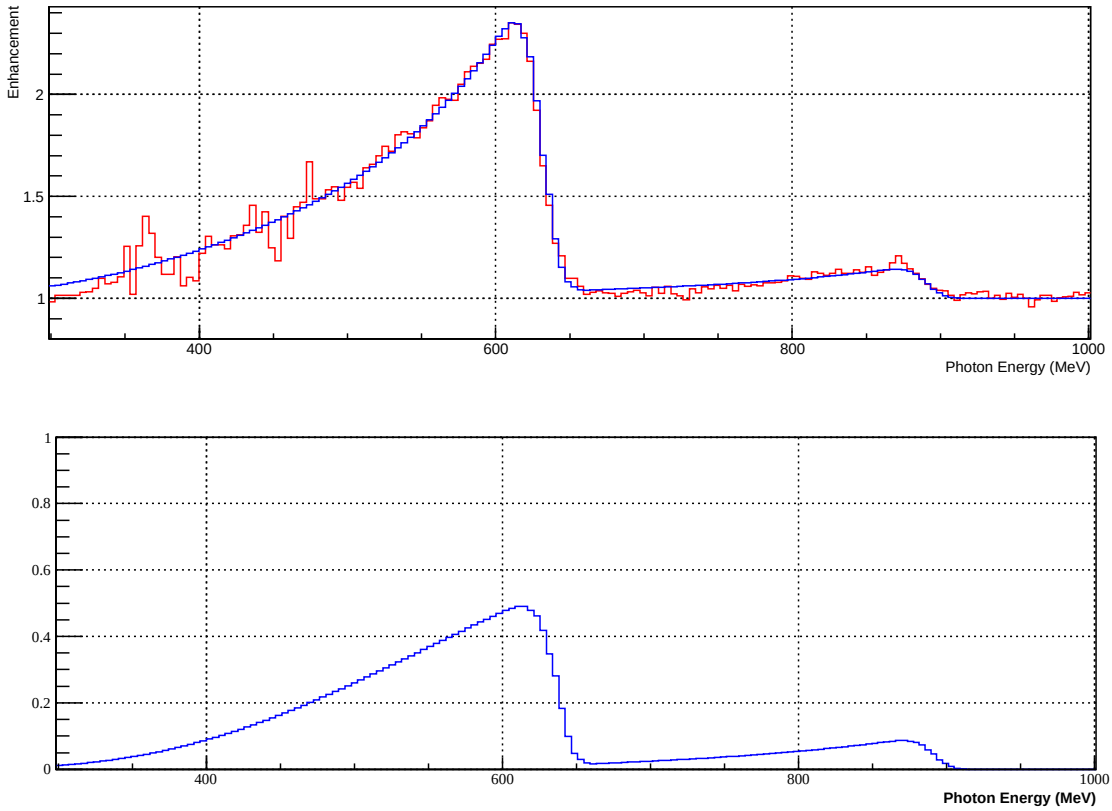

Figure 5.1: Top Plot: Fit (blue) to the enhancement (red) from the experimental data. Bottom Plot: Polarisation extracted from the fit [69]

.

tween the two fit techniques based on previous data can be seen in figure 5.2. As can be seen, small differences in the enhancement fits can cause significant differences in the resulting polarization.

5.2 Extraction of Σ

Σ is defined as the modulation induced in the system by a linearly polarized photon beam. It manifests itself in the azimuthal distributions of the emitted products in a photoproduction reaction; in this case, the π^0 from the $\gamma p \rightarrow \pi^0 p$. The cross section for this process can be described with:

$$\frac{d\sigma}{d\Omega} = \sigma_0(1 + P^T \Sigma cos(2\phi)) \tag{5.1}$$

Where σ_0 is the unpolarised cross section, P^T is the degree of linear polarisation of the photon beam and ϕ is the azimuthal separation of the reaction plane, in which the π^0 and proton are emitted, and the polarisation plane. The most straightforward way to extract the Σ observable involves making use of the $cos(2\phi)$ dependence of the polarisation. This can be done by dividing out unpolarised data from the polarized. However the necessity to understand fully the acceptance of the detector systems complicates this method. Instead an asymmetry can be formed from two different polarized data sets. These must be orthogonal with a 90° phase difference between the polarisation planes. Traditionally, these planes are defined as *parallel* and *perpendicular*, as the planes are oriented with respect to the horizontal in the laboratory. In this experiment, *parallel* and *perpendicular* were shifted by 45° in order that the *parallel* distribution did not have its maximum polarisation plane in the region of the steel rim at the Crystal Ball hemispheres, thereby minimizing the loss of acceptance.

From now on, $\parallel$ and $\perp$ will denote *parallel* and *perpendicular* orientations of the beam polarisation respectively. For a distribution of π^0's in two different polarisation

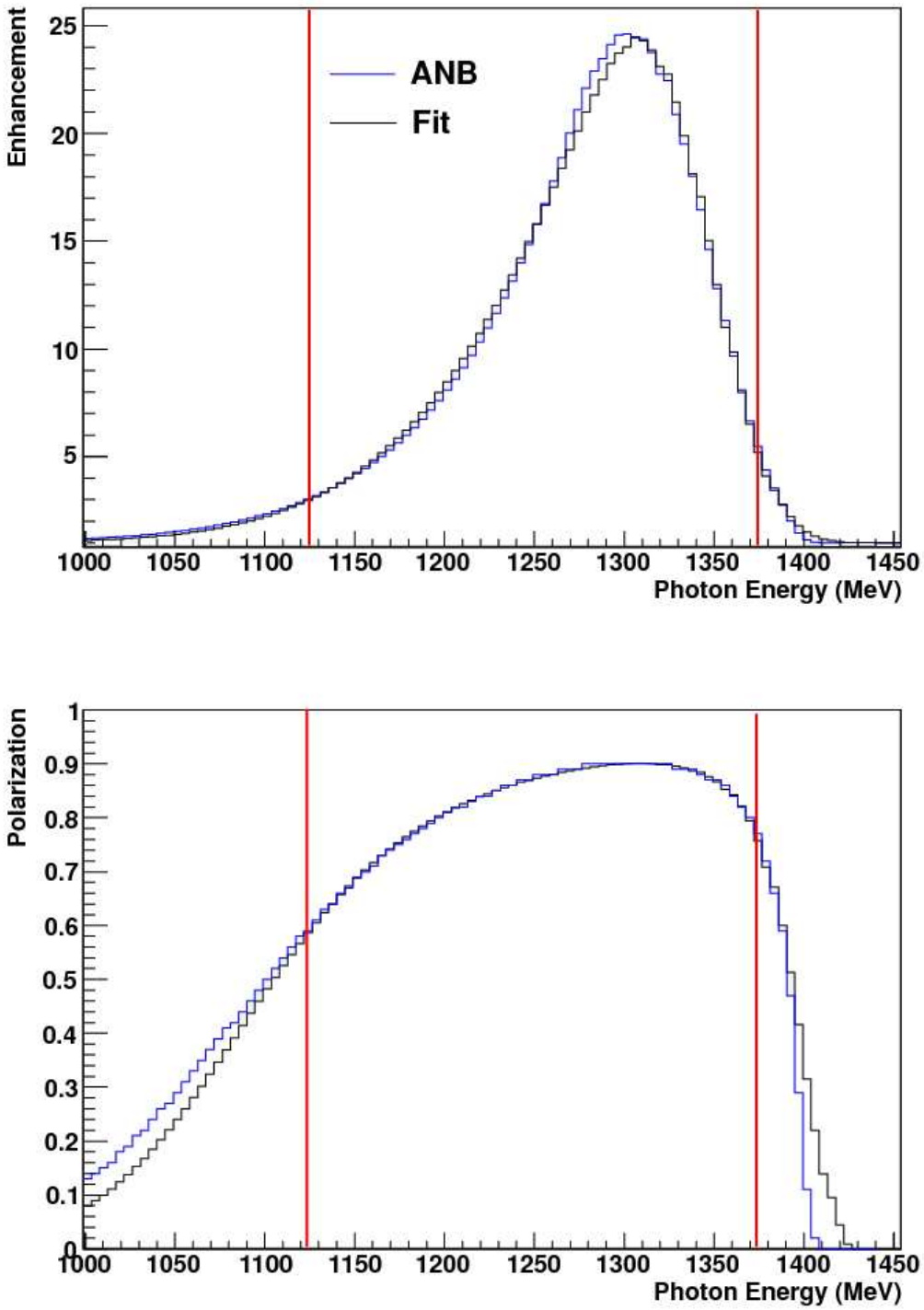

Figure 5.2: Example of an AnB (blue) and a phenomenological fit (black) to an enhancement spectrum (top), with the resulting polarisation (bottom) from [69].

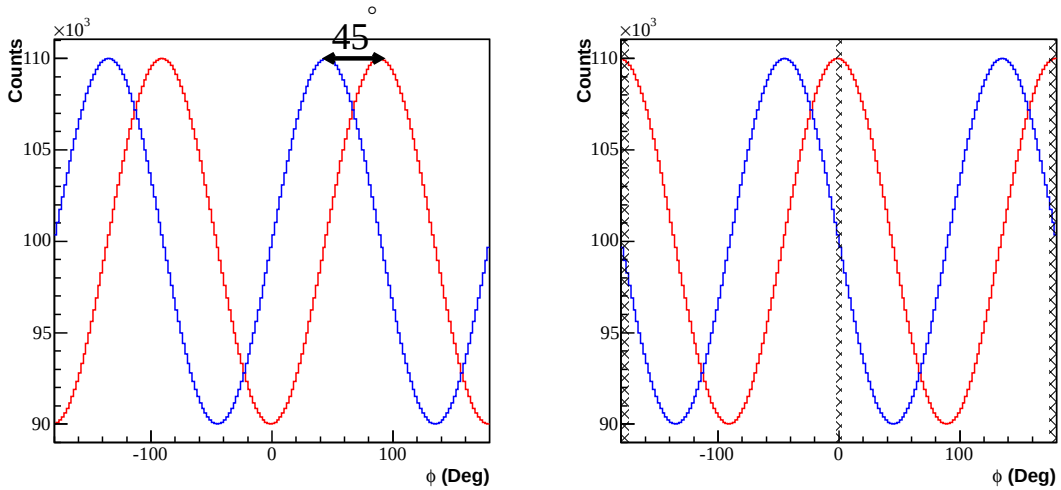

Figure 5.3: Example ϕ distribution for (left) *perpendicular* and (right) *parallel*. (left) shows the 45° phase shift used in this experiment and (right) shows the areas of maximum polarisation, which align with the region of reduced acceptance of the Crystal Ball when the polarisation planes are in the classic orientation. Classic orientation is shown in blue, and the new orientation in red.

planes, the distribution can be written as follows:

$$\begin{aligned} N_{\parallel} &= AF_{\parallel}(1 + P_{\parallel}^{T}\Sigma cos(2\phi)), \\ N_{\perp} &= AF_{\perp}(1 + P_{\perp}^{T}\Sigma cos(2\phi)) \end{aligned} \tag{5.2}$$

Where $F_{\parallel,\perp}$ is the photon flux of the beam for the two different polarisation planes, and $P_{\parallel,\perp}^{T}$ is the degree of linear polarisation for the two different planes. It is safe to assume that the degree of polarisation and flux for both planes is equivalent, as during the taking of data the polarisation planes were switched regularly, meaning any shift in these variables would be reflected in both planes. In equation 5.2 A is the acceptance of the detector system. It is important to note that the detectors acceptance is invariant of the polarisation plane. The new orientation of the polarisation planes means that there is no significant difference between the flux of both polarisation planes due to loss of acceptance.

Forming an asymmetry from both distributions in equation 5.2 gives:

$$\frac{N_{\parallel} - N_{\perp}}{N_{\parallel} + N_{\perp}} = P^{T}\Sigma cos(2\phi) \tag{5.3}$$

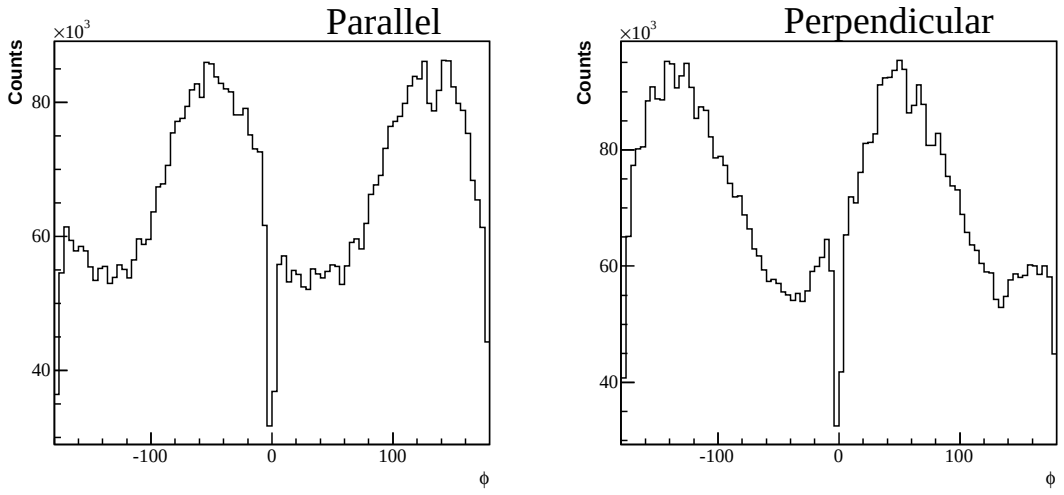

Figure 5.4: Azimuthal π^0 angular distributions for both polarisation planes for all θ in the centre of mass.

Where the flux and acceptance cancel out, so explicit measurements of both these factors is not required in order to extract an asymmetry. It is likely due to the sensitive orientation of the diamond that there will be a small offset in the ϕ distribution, ϕ_0 giving:

$$\frac{N_{\parallel} - N_{\perp}}{N_{\parallel} + N_{\perp}} = P^T \Sigma cos(2\phi - \phi_0) \tag{5.4}$$

Figure 5.5 shows the resulting asymmetry taken with the distributions in figure 5.4. The relationship between polarisation observables and experimental quantities is given by references [17, 72]. In this analysis it was possible to extract Σ over a wide range of energies ($450 < E_\gamma < 650$ MeV) and π^0 polar angles ($50^\circ < \theta_{CM} < 160^\circ$). Due to the high level of statistics taken in the experiment, it was possible to extract the angular distributions for each Tagger channel across the entire coherent peak ($\sim$4 MeV bins), with the exception of two channels at either end of the coherent peak where the degree of linear polarisation effectively drops to zero. Figure 5.6 shows a typical angular polar (θ) versus azimuthal (ϕ) plot for a single Tagger channel. An example of the fits for a single Tagger channel can be found in figure 5.7

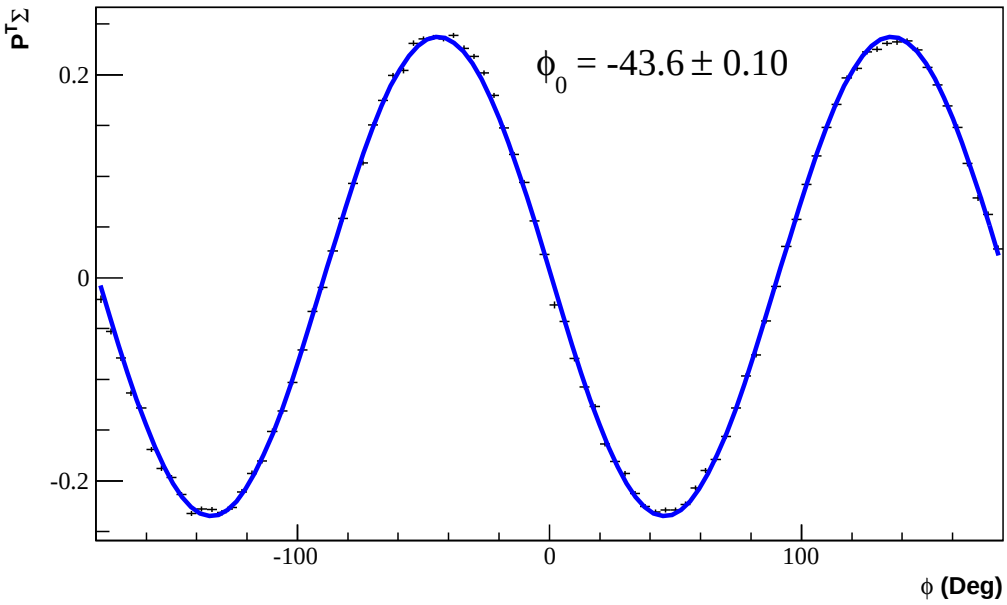

Figure 5.5: Example of the asymmetry between two polarisation planes. This is taken over the entire coherent peak and averaged over all π^0 θ in the centre of mass. ϕ_0 was extracted as 43.6°

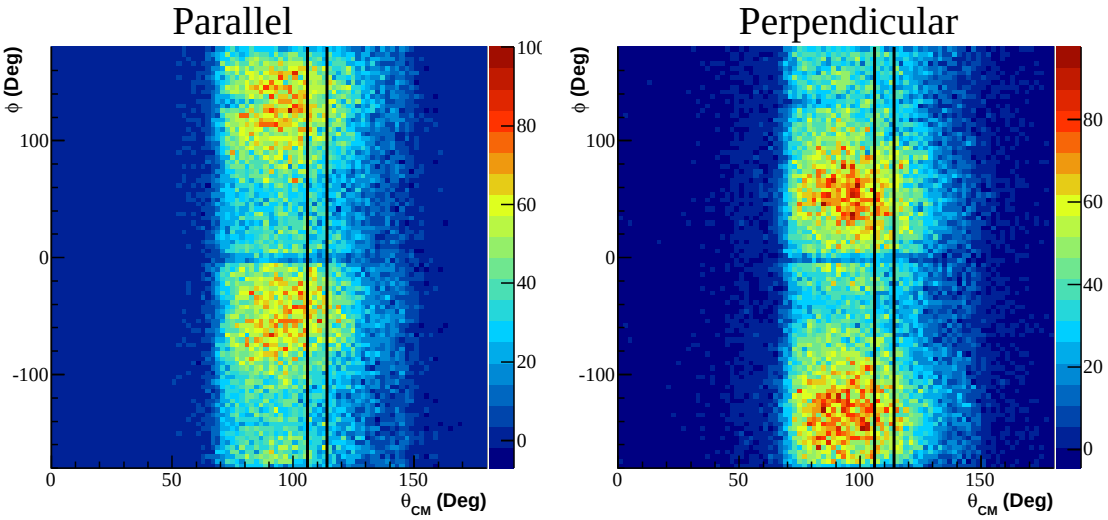

Figure 5.6: Typical angular distribution for the extraction of Σ. The region highlighted with the black lines shows an example of a θ projection taken in order to extract the π^0 ϕ distributions to form an asymmetry.

5.3 Extraction of O_x and T

The extraction of the beam-recoil observable O_x is discussed in this section, and along with it the extraction of T from a simultaneous fit function. This section

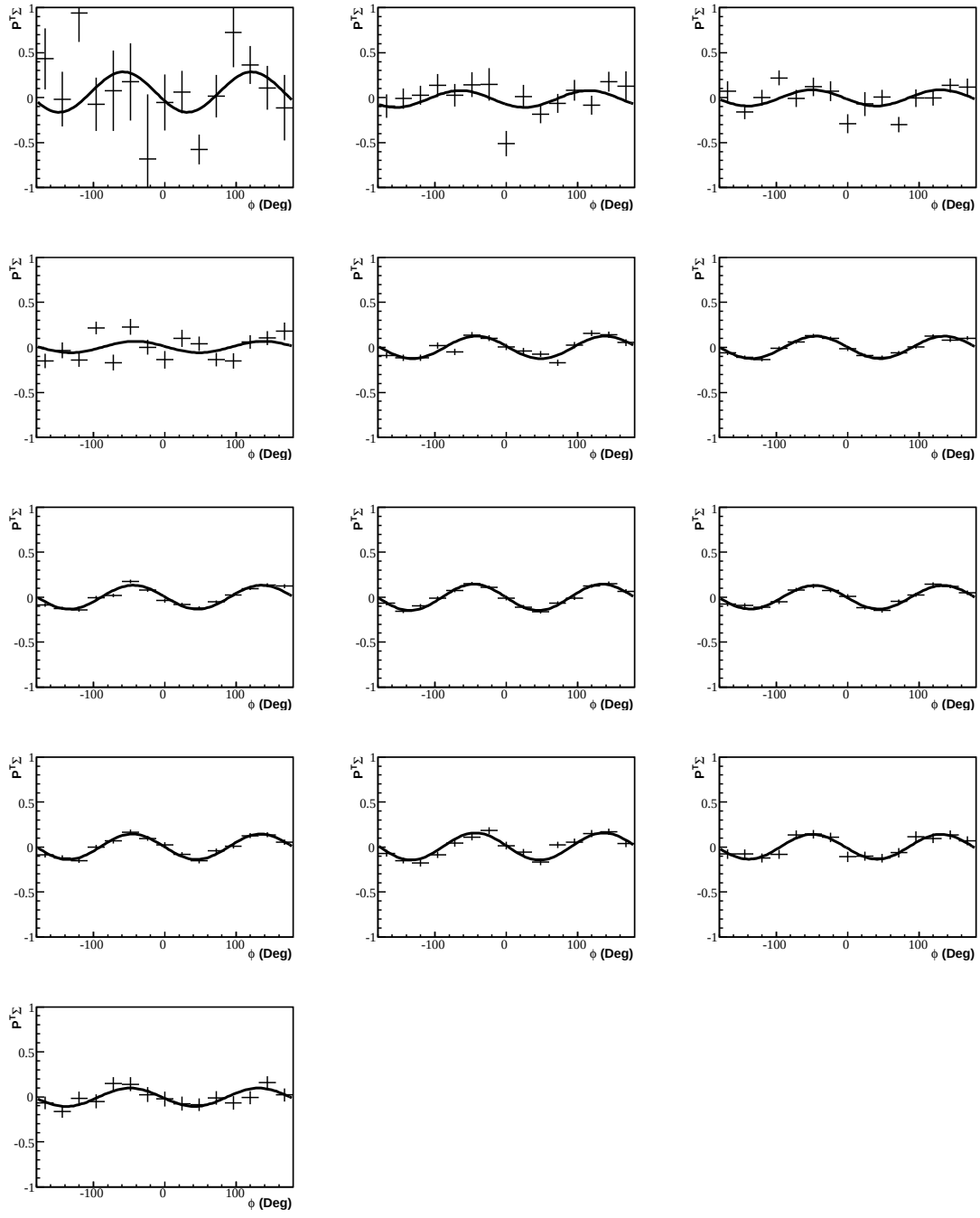

Figure 5.7: Example of fits for the extraction of Σ for a single Tagger channel. Each plot is an asymmetry for a different θ projection from the example plots in figure 5.6 from $50^\circ < \theta_{CM} < 160^\circ$.

will briefly outline the nucleon-nucleon interaction which is utilized to analyse the polarisation of the recoiling nucleon, as well as an outline of the analysing power of the carbon polarimeter. The extraction of the observables will follow.

5.3.1 The Nucleon-Nucleon Interaction

The extraction of O_x requires the measurement of polarisation transfer from a linearly polarized photon to the recoiling proton. As mentioned in section 3.3.2, the polarisation is measured via the method of secondary scattering in a carbon polarimeter. Protons that scatter via the strong interaction display a characteristic sinusoidal modulation in their outgoing azimuthal distribution, with respect to the polarimeter, as discussed later in this section. The amplitude of this distribution is directly related to the transverse polarisation of the proton multiplied by the effective proton-carbon (p-C) analysing power associated with the polarimeter, which is discussed in section 5.3.2. This section will outline the nucleon-nucleon interaction as a tool for measuring the polarisation of the recoiling proton.

The force between two nucleons is governed by the QCD colour charge (Section 1.1.1). However a theoretical framework for this force has not been formally achieved in terms of quarks and gluons within QCD; phenomenological models are instead used. These models are based on parameters from fits to data on $N-N$ interactions, with constraints placed on symmetries of the strong interactions [73, 74, 75]. There is a dependence on the spins of the two nucleons in a $N-N$ interaction (s_1 and s_2 for the two respective nucleons), meaning that the potential must factor in these spins. The interaction can happen between either proton-proton, neutron-neutron or proton-neutron, with all interactions having the same strength after any electromagnetic forces are taken into account.

Figure 5.8 shows a representation of the scattering process. A nucleon incident on the target with momentum vector $\overrightarrow{p}$ will have angular momentum $\overrightarrow{L} = \overrightarrow{p} \times \overrightarrow{d}$ where $\overrightarrow{d}$ is the position vector of the incident nucleon with respect to the target nucleon. The combined spin of the system $\overrightarrow{S} = \overrightarrow{s}_1 + \overrightarrow{s}_2$, and the spin orbit

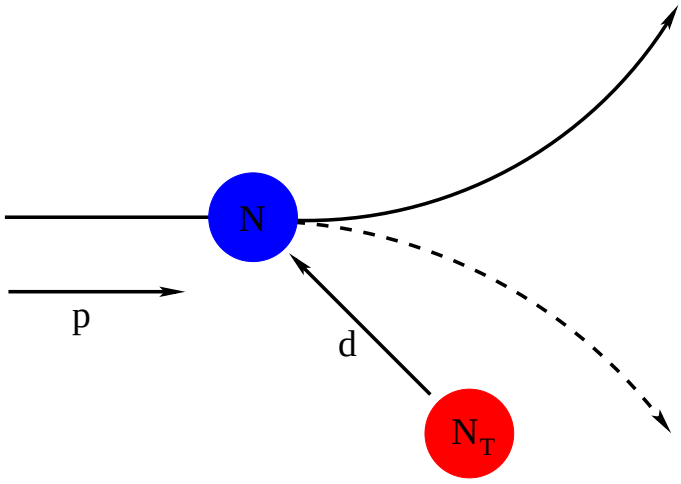

Figure 5.8: Diagram of the nucleon-nucleon interaction. N_T denotes the target nucleon with spin aligned downward. The blue N is the approaching nucleon, distance $\overrightarrow{d}$ away from the target nucleon, with momentum vector $\overrightarrow{p}$. Its path divergence is dictated by the angular momentum of the system.

coupling follows as $\overrightarrow{L} \cdot \overrightarrow{S}$. The nucleon is deflected (or attracted) dependent on the orientation of the angular momentum $\overrightarrow{L}$. Figure 5.8 shows the nucleon being deflected away from the target nucleon as the angular momentum is aligned into the page. The dashed line shows how the nucleon would be attracted towards the target nucleon if the target spin is aligned out of the page. This is the basic principle of how polarisation relates to the spin-orbit coupling of the strong force scattering. The polarisation of the incoming nucleon can be defined as follows:

$$P_N = \frac{N^{\uparrow} - N^{\downarrow}}{N^{\uparrow} + N^{\downarrow}} \tag{5.5}$$

where $N^{\uparrow,\downarrow}$ is the number of spin up or spin down states in the nucleon interaction system [76]. Spin-orbit coupling results in nucleons being scattered in the same direction when their spins are preferentially aligned, and the polarisation can be calculated from the outgoing protons azimuthal distribution with respect to the polarimeter.

5.3.2 Analysing Power

The parametrization of the analysing power was performed by colleagues from Edinburgh University [77]. Analysing power, in terms of spin polarisation observables, is the sensitivity of the anlysing medium to the spin of a nucleon undergoing a strong force scatter. Proton-carbon analysing power is normally measured as part of the experiment by using electron-proton scattering in order to calculate the effective analysing power (A_{eff}). Analysing power is required when measuring the polarisation transfer to the recoiling nucleon using a secondary scattering method. To date, the most widely used material for secondary scattering is carbon (^{12}C), and several laboratories have measured the $p-C$ analysing power [78, 79, 80]. Carbon has been used for the reason of its high cross-section for scattering. In order to measure the analysing power with the method of electron-proton scattering, scattering of incident protons in the carbon polarimeter with known polarisation must be used, such that the only unknown variable is the analysing power itself. These protons are produced by scattering polarized electrons off a proton (lH_2) target. Because of previous measurements of the analysing power of carbon, there is enough data to form a parametrized fit in terms of the momentum of incident protons on the analyzer and the scattering angle θ_{Sc}. Parametrization of this nature have been calculated previously, the most prominent being the McNaughton calculation [81].

At the A2 experiment there is no way to produce a sample of protons of known polarisation in order to characterize the analysing response of the carbon polarimeter, nor a practical way to dump the electron beam used to produce protons in elastic $e-p$ scattering. In order to get around this, the analysing power was extracted from the GEANT4 simulation of the A2 experiment with the carbon polarimeter added to simulate the geometry. In order to do this, new methods of extracting the effects of polarized scattering were added by colleagues at the University of Edinburgh. These parametrization were based mainly upon the work in reference [81] but also used the recent world dataset of $p-C$ scattering from reference [80].

With these new methods, it was possible to simulate polarized scattering in the carbon polarimeter for the A2 simulation using a polarized proton beam with $\overrightarrow{P}_{proton} =$

± 1, and the azimuthal distributions could be analyzed to extract an effective analysing power. The new additions to the simulation do not, however, take account of the systematic uncertainties involved with the analysing power of the polarimeter. The precise extraction technique of the analysing power will be presented in the next section.

5.3.3 Extraction

The extraction of O_x and T is dependent on the azimuthal distribution of scattered events from the polarimeter. The azimuthal distribution of scattered proton events can be written as:

$$N_{sc}^{\parallel,\perp} = \left[1 + A_{eff}\left(\frac{P \pm P^T T cos(2\phi_{\pi^0})}{1 \pm P^T \Sigma cos(2\phi_{\pi^0})} cos(\phi_{sc}) \pm \frac{P^T O_x sin(2\phi_{\pi^0})}{(1 \pm P^T \Sigma cos(2\phi_{\pi^0}))} sin(\phi_{sc})\right)\right]$$

Where:

- $N^{\parallel,\perp}$ is the number of events with the *parallel* or *perpendicular* proton polarisation.
- A_{eff} is the effective analysing power of the polarimeter.
- P is the recoil proton polarisation observable.
- P^T is the degree of linear polarisation of the photon beam.
- T is the target proton polarisation observable.
- Σ is the beam polarisation observable, discussed in section 5.2.
- O_x is the beam-recoil polarisation transfer observable.
- ϕ_{π^0} is the π^0's azimuthal angle in the centre of mass.
- ϕ_{sc} is the proton azimuthal scattering angle in the polarimeter reference frame.

Because the scattering angle of the proton in the azimuthal direction is with reference to the polarimeter, it is important that each event is rotated into the polarimeter reference frame, as defined below. Forming an asymmetry from the previous expression

gives:

$$a = \frac{N_{sc}^{\parallel} - N_{sc}^{\perp}}{N_{sc}^{\parallel} + N_{sc}^{\perp}} \tag{5.6}$$

$$a = \frac{P^T \Sigma cos(2\phi_{\pi^0}) + A_{\text{eff}}((P^T T cos(2\phi_{\pi^0})cos(\phi_{sc}) + (P^T O_x sin(2\phi_{\pi^0}))sin(\phi_{sc}))}{1 + A_{\text{eff}} P cos(\phi_{sc})}$$

This leaves four observables to consider when extracting O_x. T and Σ can be extracted with O_x by fitting the asymmetry which is covered later in this section. P requires a precise model of the acceptance of the detector setup that is not available. However the observable is well understood from previous experimental observation and as such, models introduced in chapter 2 are used to constrain P rather than trying to perform a direct measurement of it. The behavior of P from the SAID model [20] for an energy of $450 < E_\gamma < 650$ MeV is shown in figure 5.9.

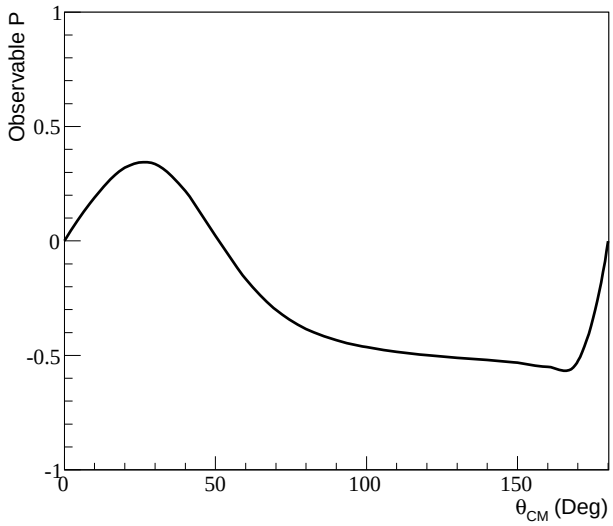

Figure 5.9: Behavior of the recoil observable P used to constrain the fit for extracting O_x. The figure is taken over an energy range of $450 < E_\gamma < 650$ MeV from the SAID model

This means O_x, T and Σ can be extracted with a single fit function. For the Σ observable it should be noted that the inclusive event selection described in previous sections, in which the explicit detection of the scattered proton is not required, gives far better statistical accuracy. It is therefore fixed for each kinematic setting from the inclusive analysis results and only the observables O_x and T need to be extracted from this part of the analysis.

Before considering the azimuthal scattering distribution, it is necessary to select as clean a sample as possible of events which undergo nuclear scattering in the polarimeter, as covered in section 4.2.4. Protons that scatter in the polarimeter do so via two different mechanisms: Coulomb scattering or nuclear scattering. Unlike nuclear scattering, Coulomb scattering does not preserve any meaningful information on the spin of the proton, and as such, these events are considered background. Because of the low efficiency of the polarimeter, only ∼10% of events will undergo a nuclear scatter. In order to select nuclear scattered events, a cut must be placed on the scattering angle ($\theta_{scatter}$). Using the simulation, it was possible to simulate a sample of events without nuclear scattering and compare that to the simulation with nuclear scattering and the data. Figure 5.10 shows the comparison between simulation with and without nuclear scattering with the data for events in both calorimeters. Different cuts were applied dependent on whether the proton scattered into TAPS or the Crystal Ball. This is because TAPS has a much better angular resolution than the Crystal Ball, as can be seen in figure 5.10.

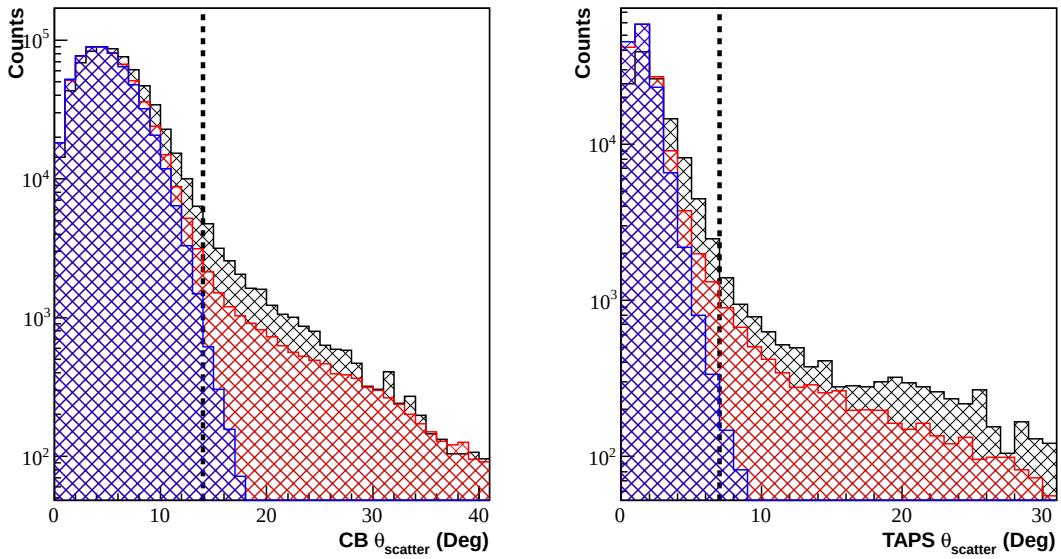

Figure 5.10: Selection of $\theta_{Scatter}$ events where (left) is scattered events in the Crystal Ball, (right) is scattered events in TAPS. On both plots, blue shows no nuclear scattered events in the simulation (only Coulomb scattering), red is all scattered events in the simulation and black is the data. The dashed lines show the regions selected to exclude the Coulomb peak at $\theta_{scatter} = 14°$ for the Crystal Ball and $\theta_{scatter} = 8°$ for TAPS.

Once the nuclear scattered events have been selected, the associated azimuthal distributions in the polarimeter reference frame are required for the asymmetry. The definition of the polarimeter reference frame is as follows:

$$\overrightarrow{z}_{pol} = \frac{\overrightarrow{p}_{recon}}{|\overrightarrow{p}_{recon}|}; \qquad \overrightarrow{y}_{pol} = \frac{\overrightarrow{p}_{tagged} \times \overrightarrow{p}_{\pi^0}}{|\overrightarrow{p}_{tagged} \times \overrightarrow{p}_{\pi^0}|}; \qquad \overrightarrow{x}_{pol} = \overrightarrow{y}_{pol} \times \overrightarrow{z}_{pol} \tag{5.7}$$

Where $\overrightarrow{p}_{recon}$ is the reconstructed proton vector incident on the polarimeter, $\overrightarrow{p}_{tagged}$ is the tagged photon beam vector and $\overrightarrow{p}_{\pi^0}$ is the π^0 vector in the centre of mass. Figure 5.11 shows a schematic diagram of the axes of the polarimeter frame. Now the azimuthal distribution of the scattered proton can be extracted from the events rotated into the polarimeter frame. Figure 5.12 shows a sample of the proton azimuthal distribution in the polarimeter reference frame, averaged over all θ^{π^0} in the centre of mass, as well as all energy.

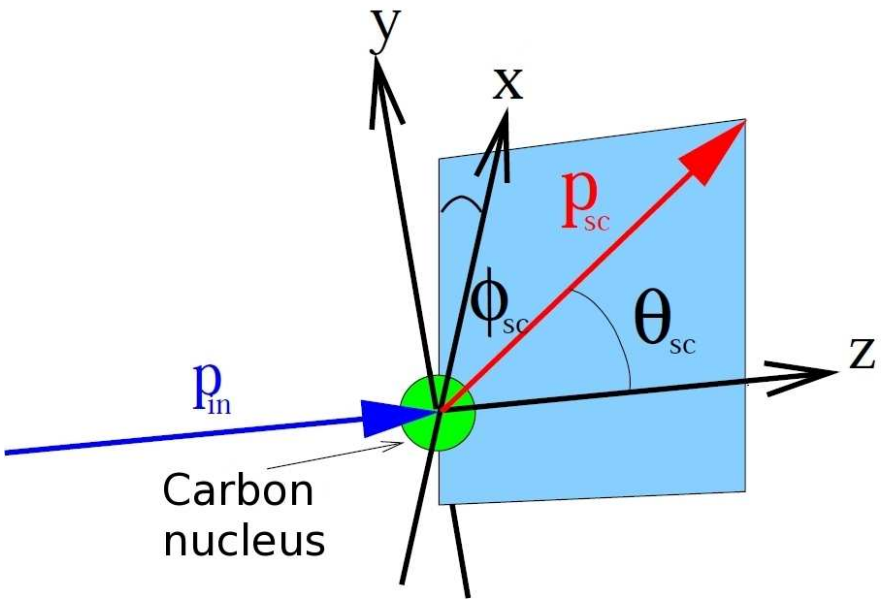

Figure 5.11: Scattering in the polarimeter reference frame.

Because of the rotation into the polarimeter frame, the asymmetry has a ϕ_{π^0} dependence when using a linearly polarized beam, due to the modulation of ϕ_{π^0} as given by the Σ observable. This can be seen in equation 5.6. In order to account for this, rather than using a sample such as the one shown in figure 5.12, the azimuthal distributions used to extract the asymmetry must take into account the π^0 azimuthal

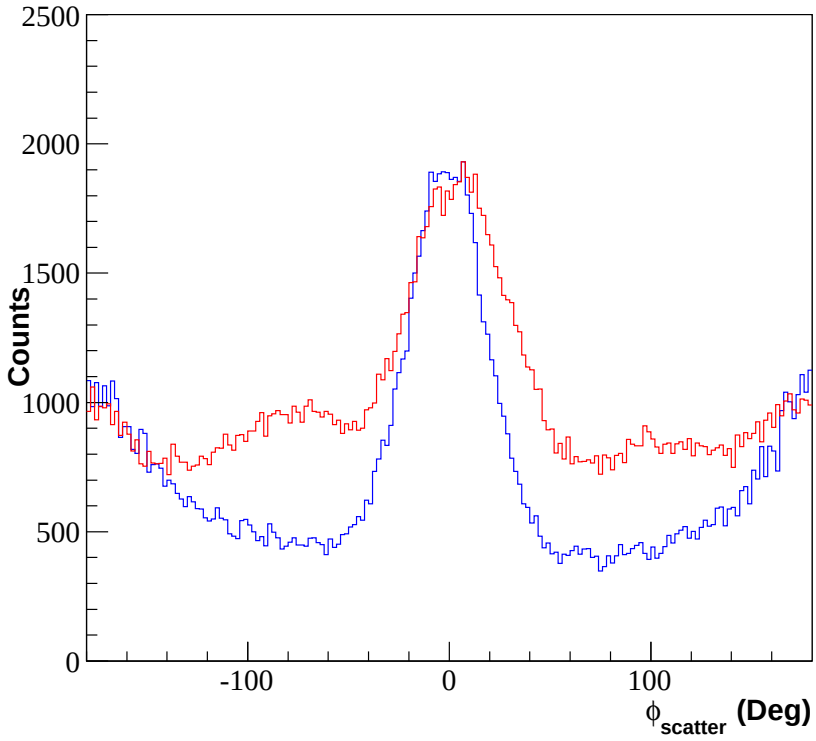

Figure 5.12: Azimuthal sample of scattered events in the polarimeter. Red shows the simulation compared to the data in blue. The difference observed is because the proton polarisation in the simulation is preferentially aligned to $P_{proton} = \pm 1$ and as such more events scatter via the strong interaction.

distribution. Figure 5.13 shows the samples of $\phi_{scatter}$ versus ϕ_{π^0} that are used to form an asymmetry. After forming an asymmetry, from the difference between *parallel* and *perpendicular* photon beam polarisation planes shown in figure 5.13 a clear modulation with ϕ_{π^0} can be seen (figure 5.14). This modulation is accounted for in the function shown in equation 5.6.

There are two methods available when extracting observables from the two dimensional asymmetry. The first is to individually fit projection's of ϕ_{π^0}, and subsequently fit the parameters of each projections fit in order to account for the sinusoidal modulation in figure 5.14. This technique is problematic in the sense that there is no easy way to extract T from this method. A better method is to define a two dimensional fit based on equation 5.6, where the value for P is constrained by the SAID model shown in figure 5.9. This fit can be seen in figure 5.15.

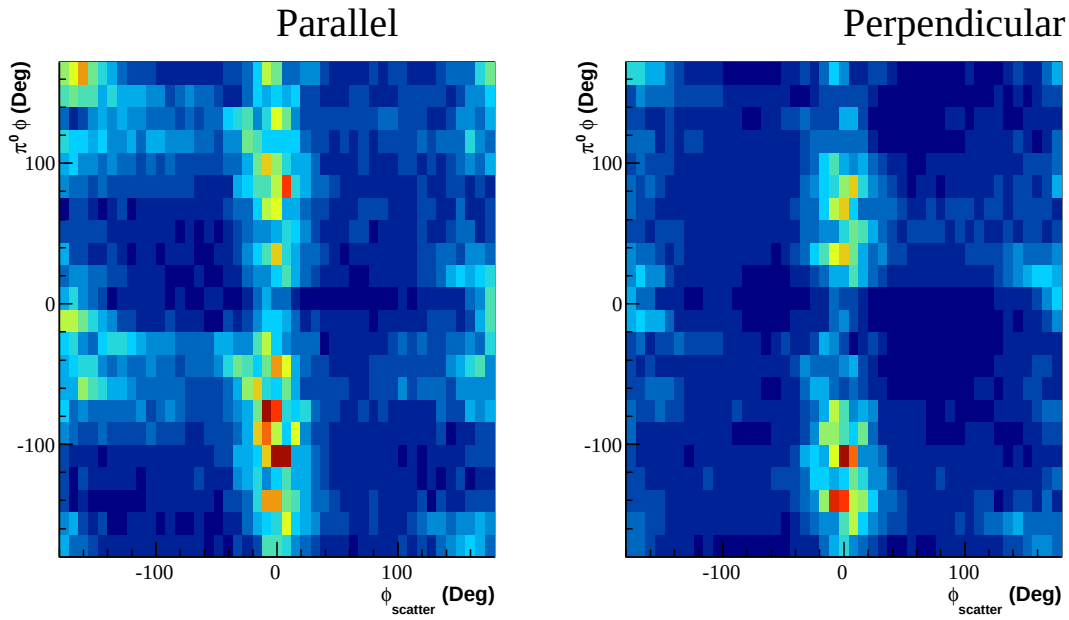

Figure 5.13: Parallel and perpendicular distributions of $\phi_{scatter}$ verses π^0 ϕ. These distributions are used to form a 2-d asymmetry.

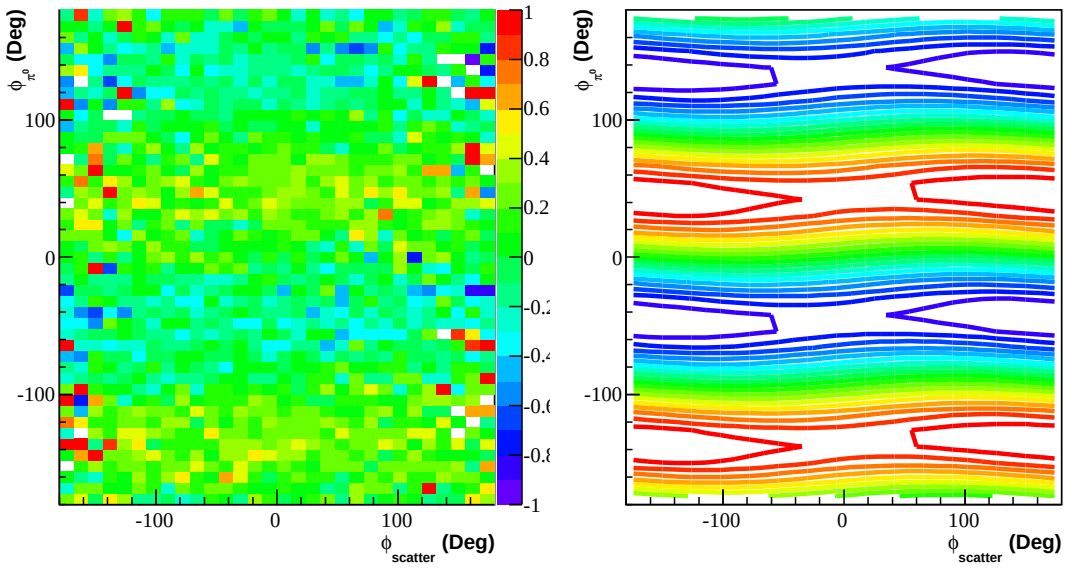

Figure 5.14: 2-dimensional asymmetry between *parallel* and *perpendicular* beam polarisation planes. (left) shows the 2-dimensional asymmetry from the data, (right) shows a projection of the fit, highlighting the modulation with ϕ_{π^0}.

Values extracted from the fit are in the form of $P^T A_{eff} O_x$ and $P^T A_{eff} T$. Determining the degree of linear photon beam polarisation was covered in section 5.1, so all that is required to extract meaningful numbers is the effective analysing power,

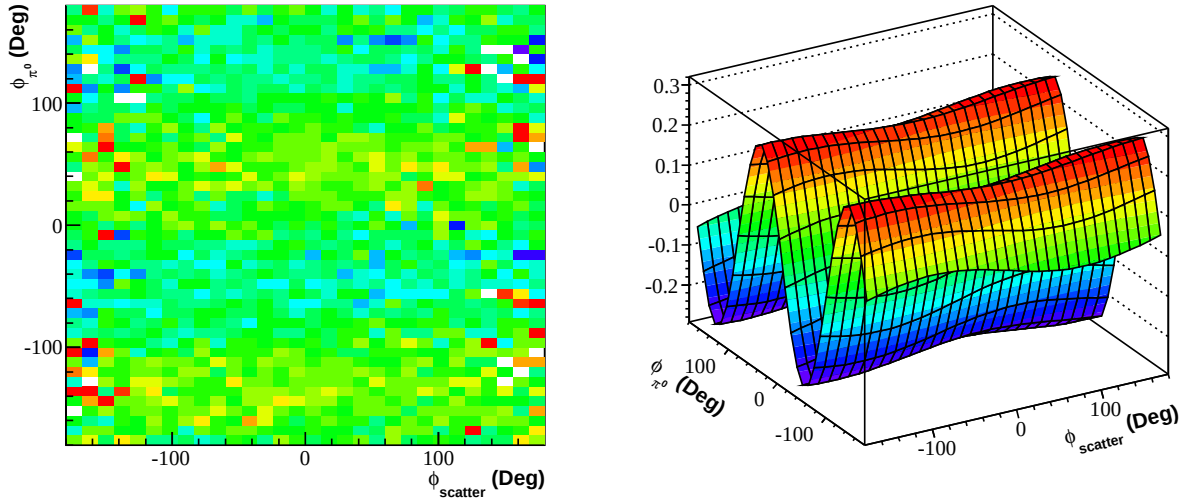

Figure 5.15: Example of the 2-dimensional fit used to extract O_x and T. (left) The recoil ϕ versus meson ϕ, and (right) the fit applied to the distribution. The different dependencies of the can be seen as a $sin(\phi)$ for the recoil and a $cos(2\phi)$ for the meson.

introduced in section 5.3.2. This was performed using the parametrization from McNaughton [81] and the A2 Geant4 simulation. In order to get an effective analysing power, an asymmetry was formed from two sets of simulated data where the proton polarisation was set to ± 1. The fit function for this simulated parametrized asymmetry is as follows:

$$N_{sc}^{\pm} = (1 + A_{eff}(P^p sin(\phi_{sc}))) \tag{5.8}$$

Where:

- $N_{sc}^{\pm}$ is the distribution of events for the different simulated datasets.
- A_{eff} is the effective analysing power.
- P^p is the proton polarisation set in the simulation (± 1).
- ϕ_{sc} is the azimuthal distribution of scattered protons in the polarimeter reference frame.

Typical simulated asymmetries and the associated fits based on the above equation can be seen in figure 5.16. A sample of the resultant values extracted for A_{eff} as a

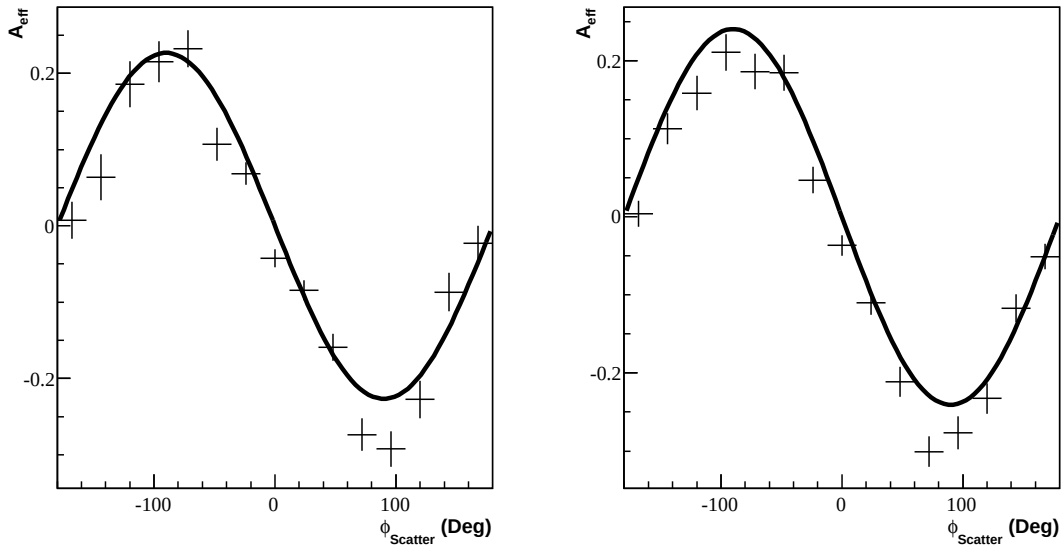

Figure 5.16: Sample fits for the simulated analysing power, showing the $sin(\phi)$ fits to the simulation where incoming polarisation was set to 100% to measure the sensitivity of the carbon analyzer.

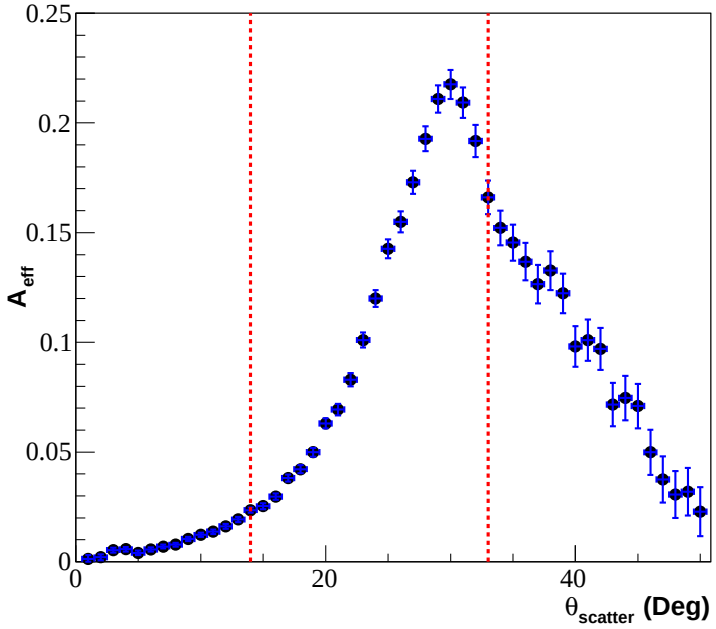

Figure 5.17: Values of effective analysing power varying with $\theta_{scatter}$. The red lines show the limits placed on $\theta_{scatter}$ ($14^\circ < \theta_{scatter} < 33^\circ$).

function of $\theta_{scatter}$ for data simulated over a photon energy range coinciding with the coherent peak are shown in figure 5.17, highlighting the cuts placed on the scattering angle. The lower limit was determined from figure 5.10 where the dilution of nuclear

scattering from Coulomb scattering events reaches a minimum. The upper limit was placed where the effective analysing power falls off from its maximum value, and a dramatic increase in statistical uncertainty is observed as the scattering angle increases. This latter effect, while not critical for the simulated data, has a much bigger impact on the statistical precision of the observables extracted from real data. This effect is primarily due to a reduction in the overall acceptance of the polarimeter at high scattering angles.

Chapter 6

Results and Discussion

This chapter presents and discusses the results for each of the polarisation observables discussed in the previous chapter, and estimates the significance of the systematic uncertainties associated with each result. The results show Σ, O_x and T for the $\gamma p \rightarrow \pi^0 p$ channel using a linearly polarised photon beam.

6.1 Σ measurement

The Σ results were extracted using the techniques outlined in chapters 4 and 5. The inclusive analysis allowed the identification of the $\gamma p \rightarrow \pi^0 p$ reaction channel by the selection of a π^0 from a set of 4-vectors, and the subsequent reconstruction of the proton from the missing mass of the reaction following identification of a π^0. Σ can then be extracted from azimuthal distributions of the π^0, provided the degree of linear beam polarisation can be calculated.

The measured Σ observable was extracted in bins of individual Tagger channels across the coherent peak (each channel being around 4 MeV in width) from $450 < E_\gamma < 650$ MeV, which corresponds to energies in the centre of mass system of $1313 < W < 1449$ MeV. These individual channels were binned in thirteen points across the π^0 polar angle distribution in the centre of mass frame over the range $50^\circ < \theta_{CM} < 160^\circ$. This level of binning was chosen to provide the most data

points available while preserving a good level of statistical accuracy. The results themselves are discussed in the following section. Tabulated results are shown in appendix A.

6.1.1 Results

Figures 6.1, 6.2, 6.3, 6.4, 6.5, 6.6 and 6.7 show the results of the measurement of Σ. Each individual plot in these figures shows the behaviour of Σ with respect to θ_{CM} for increasing photon energies (Tagger channels) with the associated statistical uncertainties. These are shown by the distribution of black points in each plot. The lines correspond to the different model predictions that were introduced in chapter 2. In each plot, the red line shows the MAID model prediction [18], blue shows the SAID model prediction [20], and finally green the Bonn-Gatchina model prediction [82]. In relevant plots, where the kinematic range of the previous measurements overlap with the results presented in this section, the previous results are included as coloured points with their statistical uncertainties. An appropriate label for each previous measurement is included in the plots, for measurements performed at the following laboratories: Kharkov [83, 84], Frascati [84], Yerevan [33] and GRAAL [25]. Some of these facilities were briefly introduced in chapter 2. The systematic uncertainties of the present measurement for each result are included as the blue bands at the base of the plots, discussion and estimation of which is covered in the following section.

The results in all bins, with the exception of a few points where the statistical and systematic uncertainties are particularly large at the extremes of θ_{CM}, increase to a maximum around the central polar angle values and slope back towards zero at forward and backward angles. The larger statistical uncertainties at forward angles are due to the small reaction cross section in that region, while the ones at backward angles result from a much reduced detector acceptance. As photon energy increases the overall statistical uncertainty decreases, reaching a minimum at the highest energies. This is primarily due to the fact that the degree of linear photon polarisation increases with energy over the coherent peak, as discussed in section 5.1.

Across all energies, the result for Σ generally peak around $0.6 < \Sigma < 0.8$.

The trend of the results and the model predictions are generally all in agreement, with the exception of the MAID model at lower photon energies which tends to diverge from the present and previous results at backward polar angles. Numerically the results exhibit good agreement with both the SAID and Bonn-Gatchina models, particularly at high photon energies. While the kinematic range of the previous results from various facilities is limited, in the regions where a comparison can be made the present results agree well with the GRAAL and Yerevan measurements at higher photon energies, but agree less well with the Kharkov and Frascati low-energy data points.

6.1.2 Systematic Uncertainty

There are two systematic uncertainties associated with the Σ measurement: one arising from the determination of the degree of linear photon polarisation, and the other as a result of the unavoidable inclusion of background events in the final data sample leading to a dilution of Σ. Determination of the degree of linear photon polarisation is via the phenomenological fit technique (section 5.1) [69], the systematic uncertainty associated with which has been estimated to be at most 5%. This value comes directly from the uncertainties in the various parameters that make up the fit function. The resulting systematic uncertainty on Σ is therefore $\sigma_{pol}^{syst} = 5\%$ across the range of photon energies of interest.

The second source of systematic uncertainty on the Σ measurement is a dilution (or contamination) as a result of the inclusion of background processes. Identification of $\gamma p \rightarrow \pi^0 p$ events is based on a 3-σ cut on the reaction missing mass, as described in section 4.2. However, as can be seen in figure 6.8, a potentially significant background exists under the 3-σ region of the main peak of interest, the level of which varies with photon energy and polar angle. As an example, everything below the red line in figure 6.8 must be considered to be background events. It is neither possible to eliminate these events nor directly measure the effect they have on the extracted

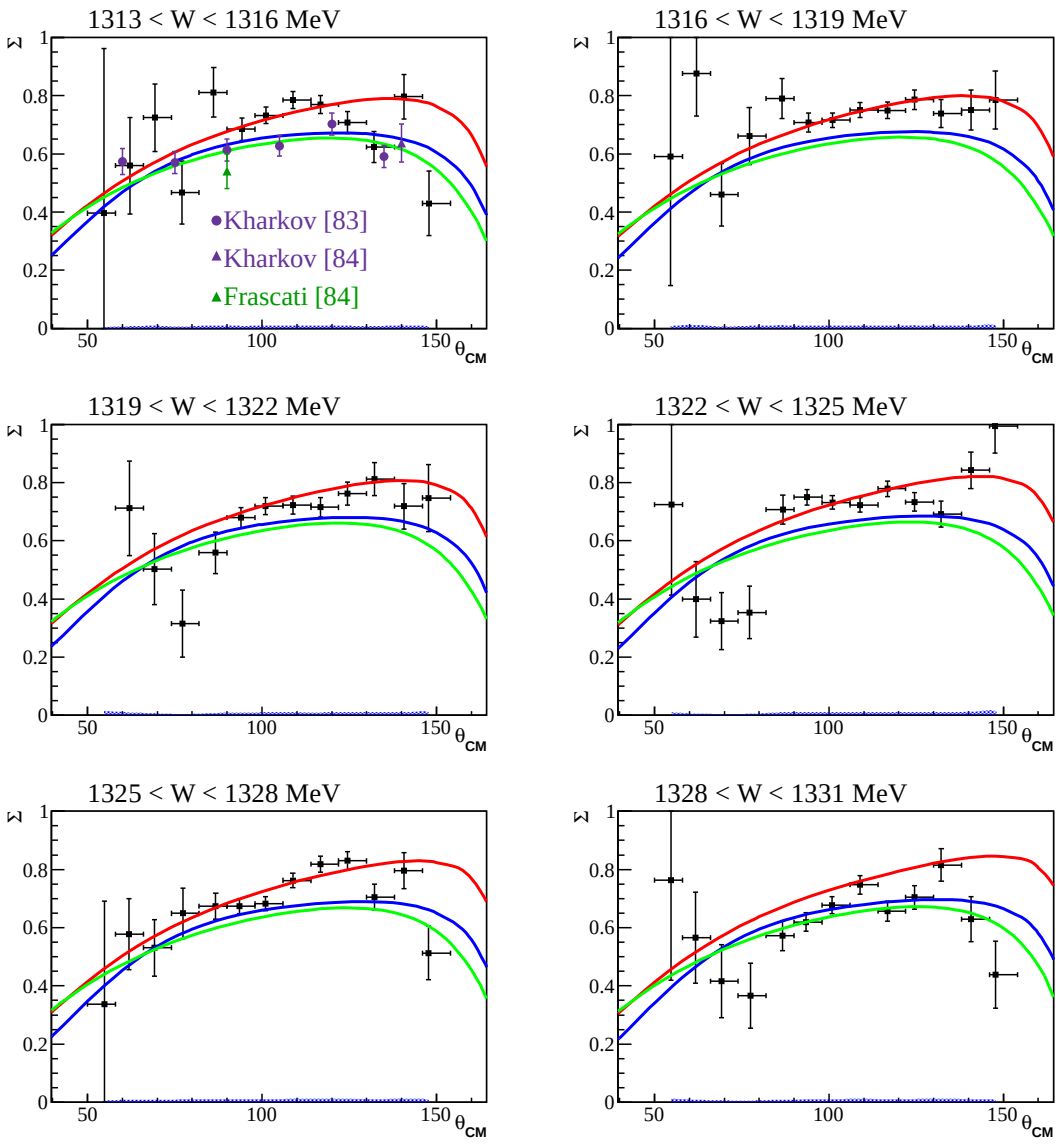

Figure 6.1: Σ binned in θ_{CM}. Each plot is an individual Tagger Channel ranging from 1313 to 1340 MeV in centre of mass energy. The Blue line represents the SAID model, Red the MAID model and Green the Bonn-Gatchina Model. The blue bands at the base of each plot show the variation of systematic uncertainties.

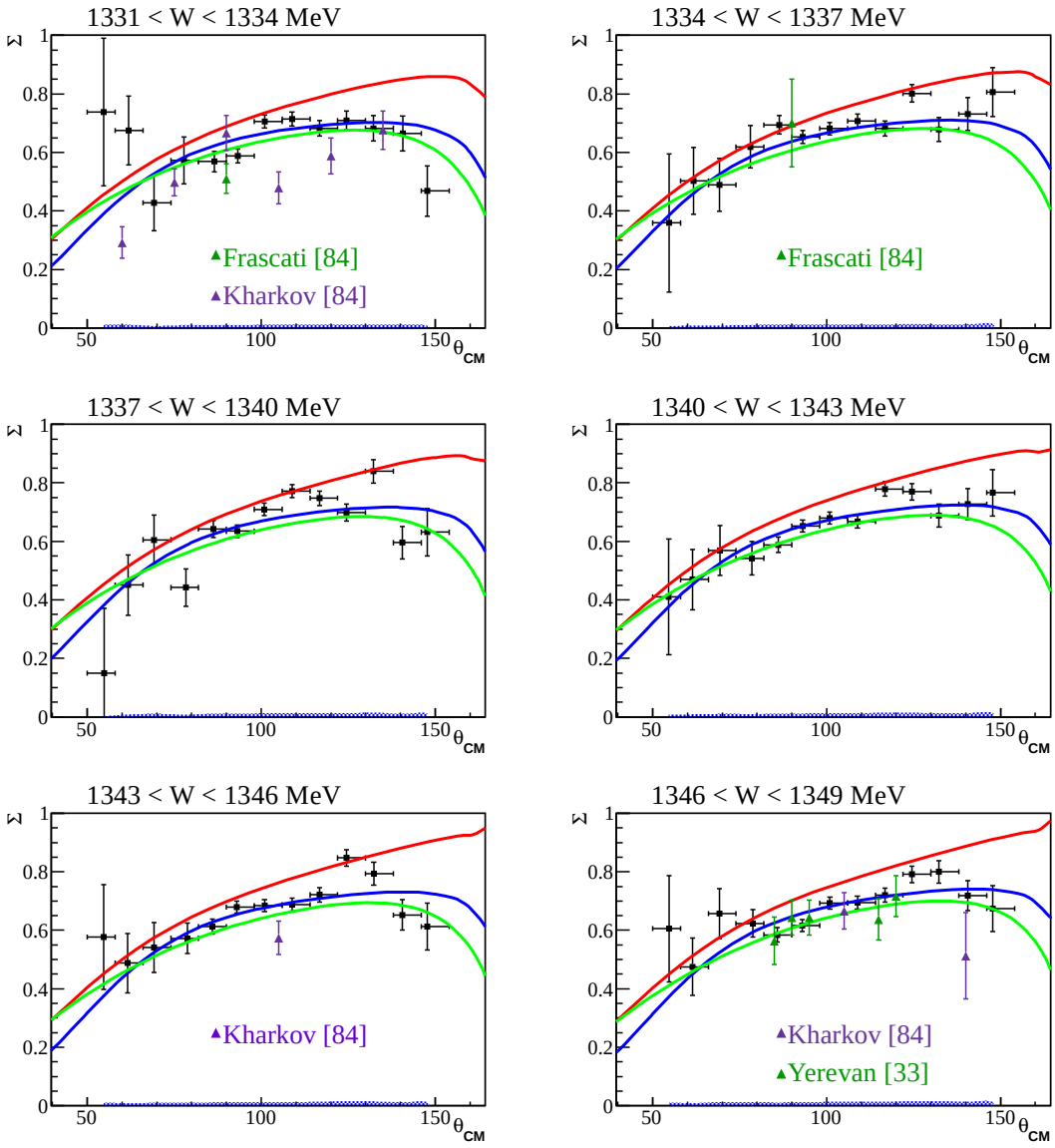

Figure 6.2: Σ binned in θ_{CM}. Each plot is an individual Tagger Channel ranging from 1340 to 1367 MeV in centre of mass energy. The Blue line represents the SAID model, Red the MAID model and Green the Bonn-Gatchina Model. The blue bands at the base of each plot show the variation of systematic uncertainties.

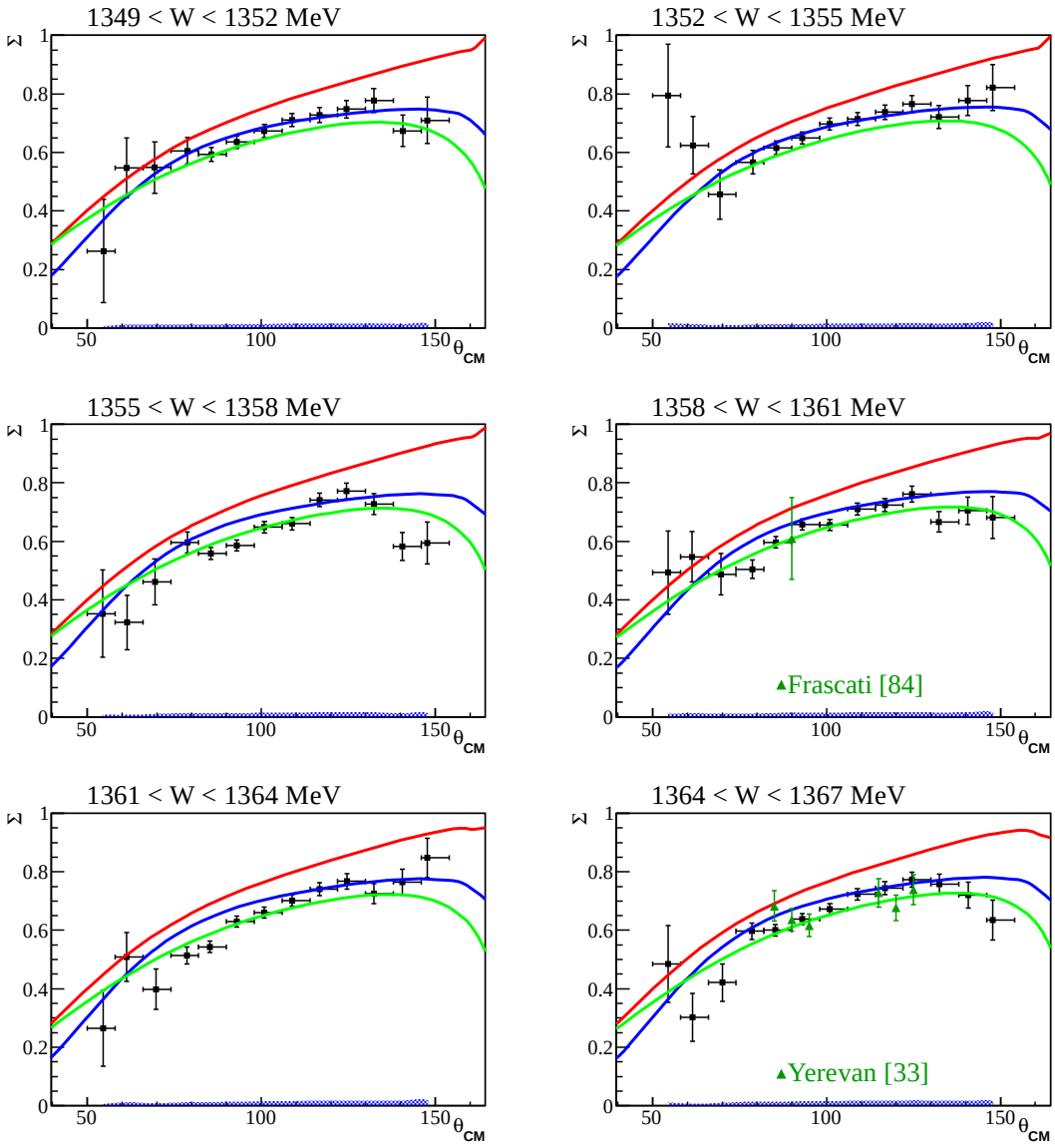

Figure 6.3: Σ binned in θ_{CM}. Each plot is an individual Tagger Channel ranging from 1367 to 1393 MeV in centre of mass energy. The Blue line represents the SAID model, Red the MAID model and Green the Bonn-Gatchina Model. The blue bands at the base of each plot show the variation of systematic uncertainties.

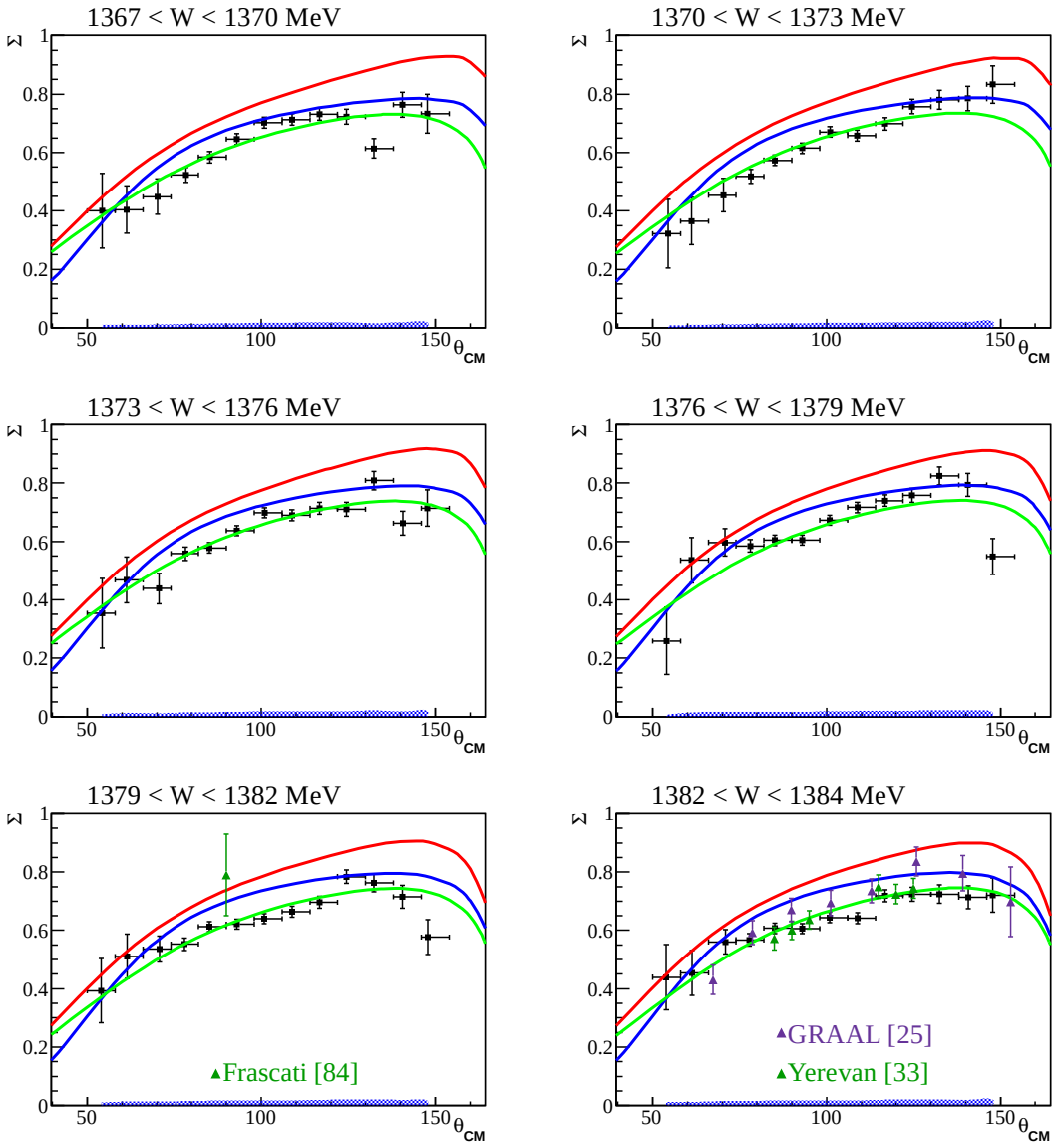

Figure 6.4: Σ binned in θ_{CM}. Each plot is an individual Tagger Channel ranging from 1393 to 1419 MeV in centre of mass energy. The Blue line represents the SAID model, Red the MAID model and Green the Bonn-Gatchina Model. The blue bands at the base of each plot show the variation of systematic uncertainties.

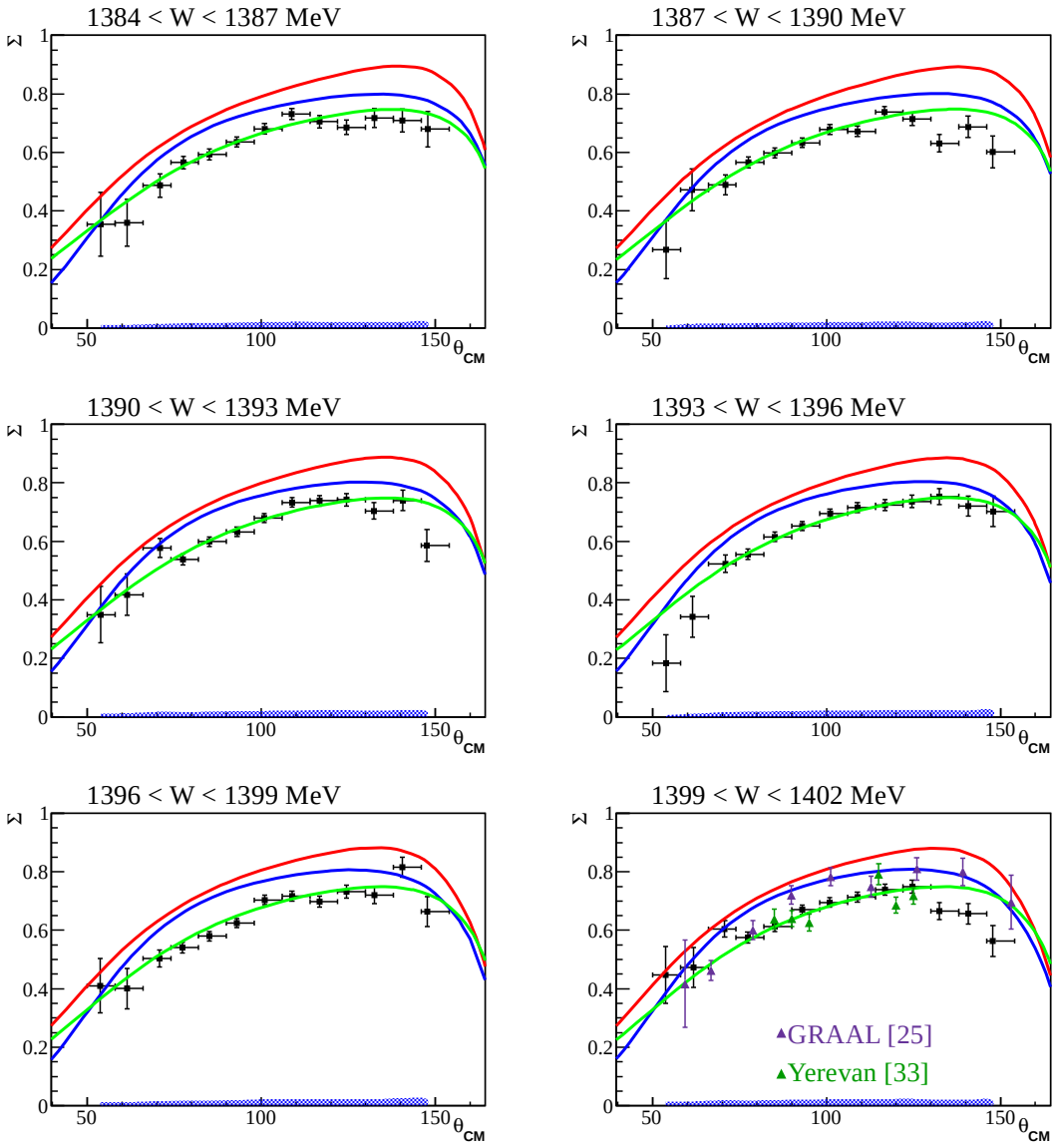

Figure 6.5: Σ binned in θ_{CM}. Each plot is an individual Tagger Channel ranging from 1419 to 1435 MeV in centre of mass energy. The Blue line represents the SAID model, Red the MAID model and Green the Bonn-Gatchina Model. The blue bands at the base of each plot show the variation of systematic uncertainties.

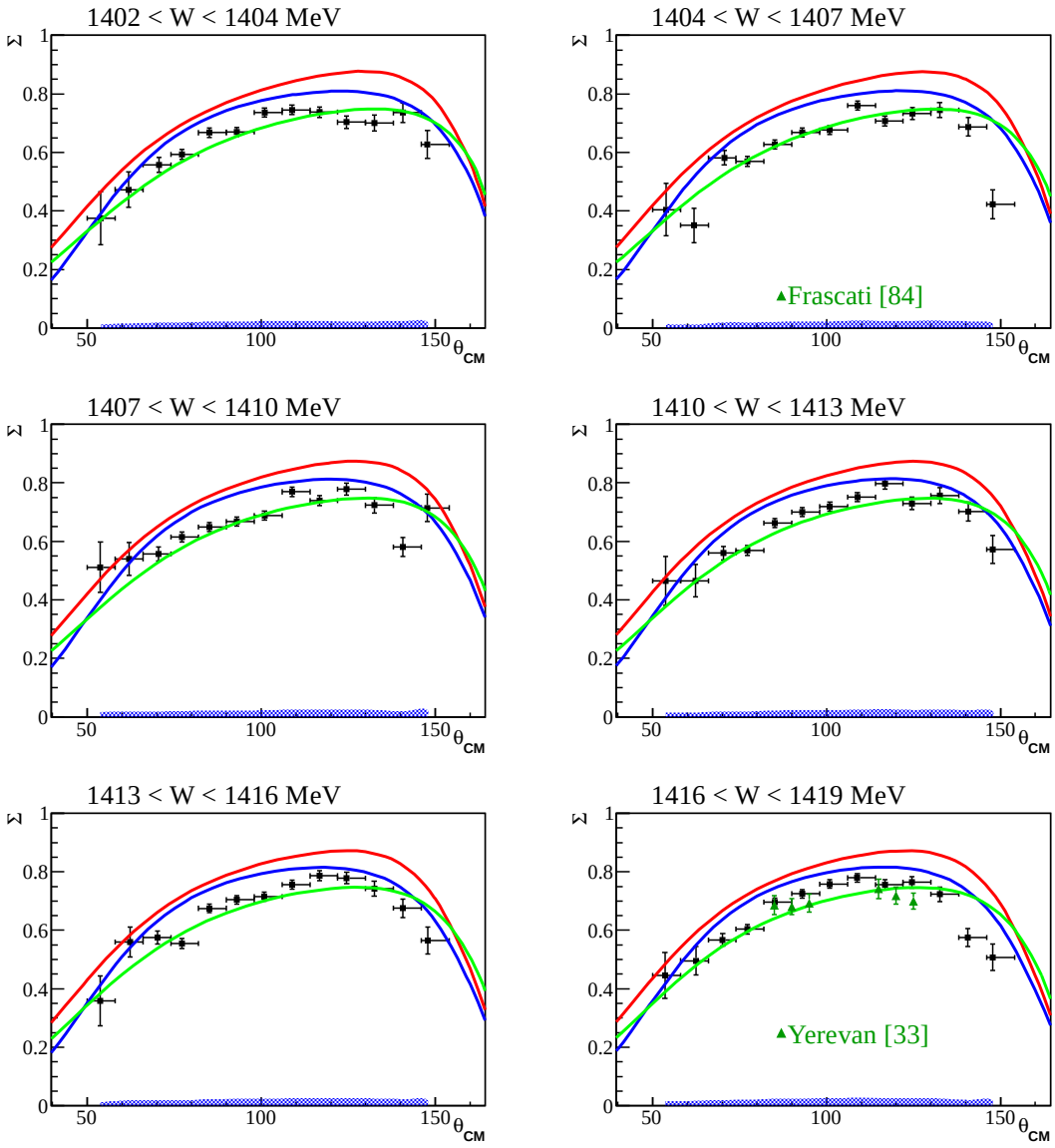

Figure 6.6: Σ binned in θ_{CM}. Each plot is an individual Tagger Channel ranging from 1419 to 1435 MeV in centre of mass energy. The Blue line represents the SAID model, Red the MAID model and Green the Bonn-Gatchina Model. The blue bands at the base of each plot show the variation of systematic uncertainties.

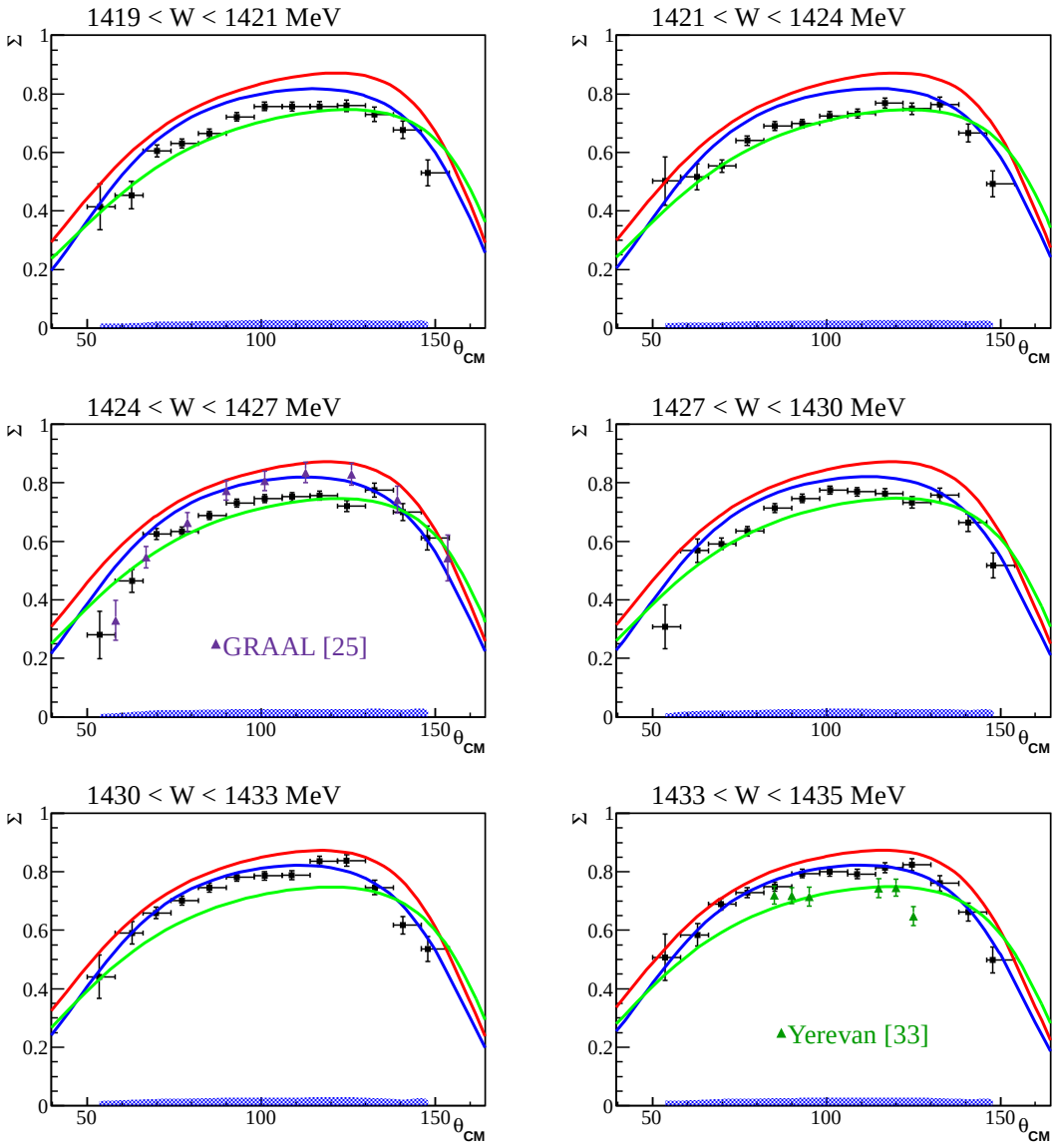

Figure 6.7: Σ binned in θ_{CM}. Each plot is an individual Tagger Channel ranging from 1419 to 1435 MeV in centre of mass energy. The Blue line represents the SAID model, Red the MAID model and Green the Bonn-Gatchina Model. The blue bands at the base of each plot show the variation of systematic uncertainties.

Σ value. Instead, estimating and quantifying this effect as a systematic uncertainty is a more appropriate approach.

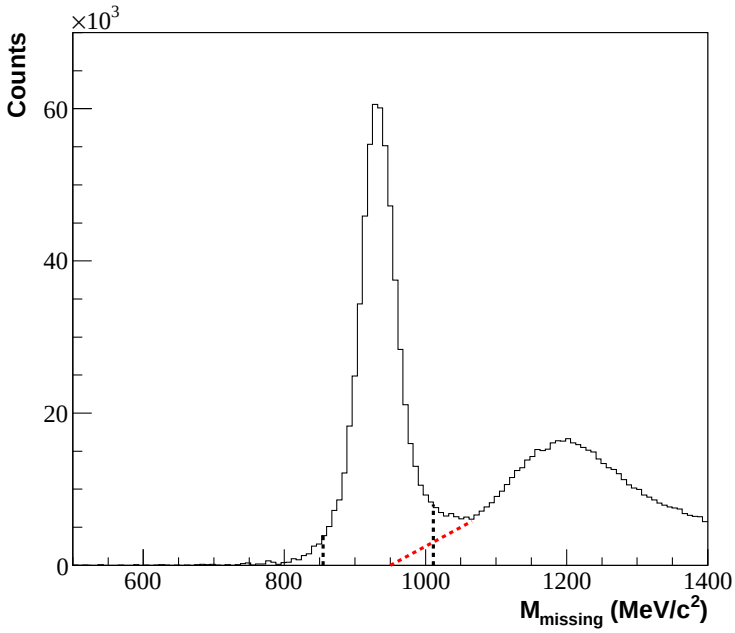

Figure 6.8: Example of background under a 3-σ cut region on the reaction missing mass. The black dashed lines show the limits of the cut and the red dashed line shows the potential level of background under the peak.

In order to estimate the dilution of Σ due to these background events, it was remeasured for a data sample which included more of these background events. In practice this was achieved by applying a 4-σ cut to the reaction missing mass, as shown in figure 6.9. The difference between the original and remeasured Σ values was used to estimate the systematic uncertainty. This uncertainty due to background dilution varies across the bins with a mean value of $\sigma^{syst}_{dilution} = 2.6\%$. A linear sum of the two separate errors gives an average total systematic uncertainty on Σ of $\sigma^{syst} = 7.6\%$. The systematic bars at the bottom of figures 6.1, 6.2, 6.3, 6.4, 6.5, 6.6 and 6.7 show the variation of σ^{syst}.

6.2 O_x and T measurement

Following the exclusive analysis procedure detailed in section 4.2.4, in which the proton scattering angles in the polarimeter were reconstructed, it was possible to

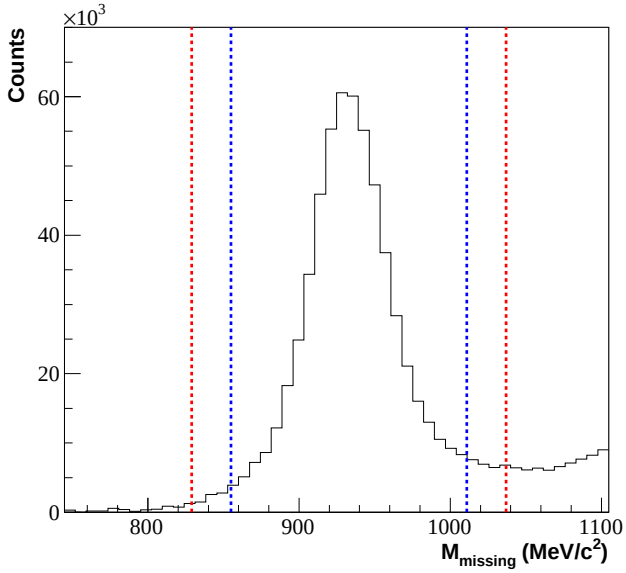

Figure 6.9: Example of the cuts applied to the missing mass in order to estimate the effect of the background dilution. The blue dashed lines shows the 3-σ cut, red shows the 4-σ cut.

extract the observables O_x and T. As a result of the correlation between the proton azimuthal scattering angle and the π^0 azimuthal angle in the centre of mass system, the 2-dimensional fit technique outlined previously was used to extract these observables. This extraction was performed for one photon beam energy bin over the entire range of the coherent peak ($450 < E_\gamma < 650$ MeV), which corresponds to $1313 < W < 1449$ MeV in centre of mass energy. Because of the loss of statistical precision associated with the low efficiency of the recoil polarimeter, it was only possible to divide the data into four θ_{CM} bins across the entire range ($0° < \theta_{CM} < 180°$). This binning scheme in photon energy and polar angle was selected to expand the kinematic range as far as possible without sacrificing the statistical uncertainty.

6.2.1 Results

Figure 6.10 shows the results for O_x and T as a function of θ_{CM}, with the black points showing the measured values of the recoil observables and their associated statistical uncertainties. The two lines on the plot show the MAID [18] and SAID [20] model

predictions respectively. Unfortunately there is currently no published prediction from the Bonn-Gatchina model [82] for these observables, and as such predictions for this model could not be included in the figure. As before, the systematic uncertainties are represented by the blue bands at the base of both plots in the figure.

The results do not follow a particular trend in either the case of O_x or T. The statistical uncertainties for both O_x and T are large at both the polar angle extremes, similar to the previous Σ results. The best statistical results are clearly seen for central polar angles. For the O_x observable, it is difficult to draw any rigorous conclusions concerning agreement between previous results and model prediction as a result of the statistical accuracy of the new measurement and the limited kinematic range of the previous measurement shown on the figure [35]. This is true for the majority of results shown in figure 6.10 with perhaps the exception of the the high statistics results for T which are in reasonable agreement with the trend of both models and the most recent previous measurement shown in the figure [39].

6.2.2 Systematic Uncertainty

The first obvious systematic uncertainties on the measurements of O_x and T are those that are common to the Σ measurement and were covered previously in section 6.1.2. These are the uncertainties from the determination of the degree of linear photon polarisation and the dilution from the inclusion of unwanted background events. When performing the O_x and T observables extraction, there is an additional systematic uncertainty, that associated with the parametrization of the effective analyzing power. As before, the systematic uncertainty from the photon polarisation has been estimated and found to be $\sigma_{pol}^{syst} = 5\%$. Based on the assumption that the background dilution to O_x and T is similar to that of Σ, the systematic uncertainty from this effect has been estimated to be $\sigma_{dilution}^{syst} = 2.6\%$.

An additional systematic uncertainty comes from the extraction of the effective analysing power. This is due to the fact that there is no direct measurement of the analysing power for the polarimeter used in the current experiment. Instead, a

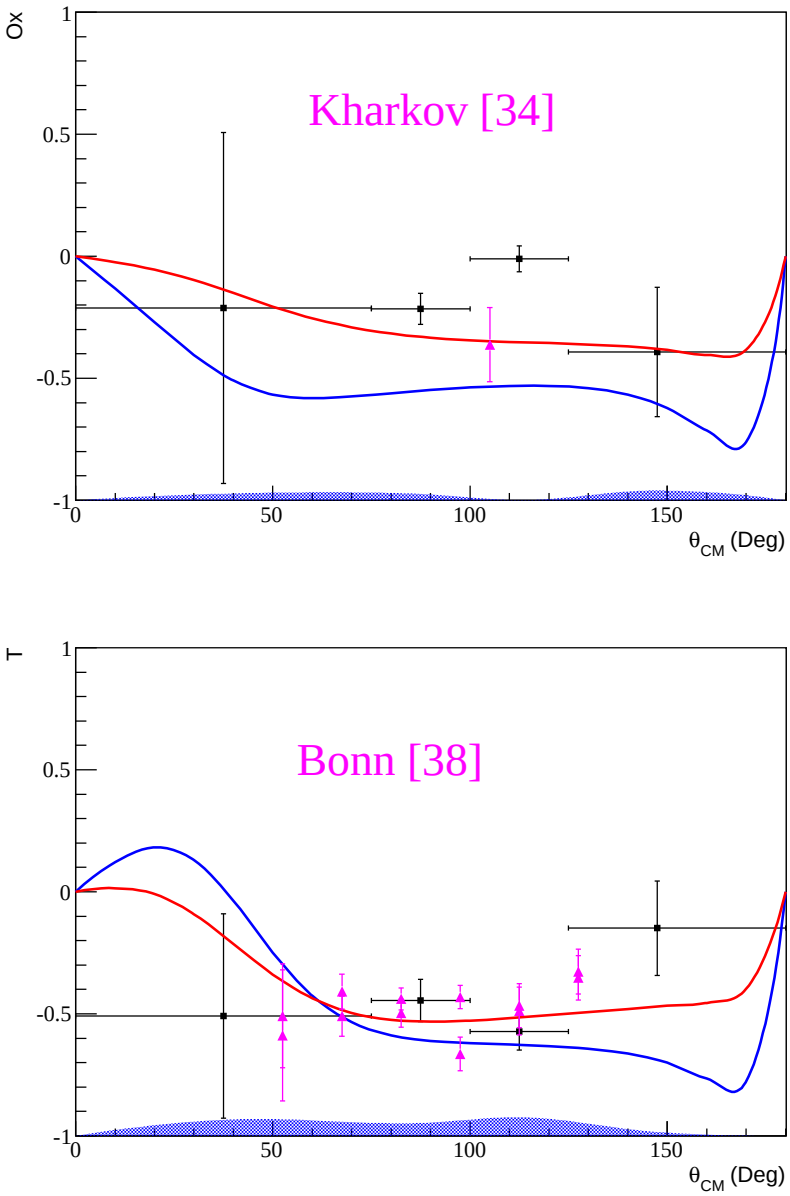

Figure 6.10: O_x and T Observables binned in θ_{CM}. Each plot was extracted over the entire range of the coherent peak, ranging from 1313 to 1449 MeV in centre of mass energy. The blue line represents the SAID model and red the MAID model. The blue bands at the base of each plot show the variation of systematic uncertainties.

combination of the A2 Geant4 simulation and the McNaughton parametrization [81] have been employed to calculate A_{eff}, as discussed in section 5.3.2. However, the A2 simulation does not take into account quasi-free inelastic nucleon-nucleon scattering, which will contribute to the overall analysing power to varying degrees as a function of proton kinetic energy. While it is possible to evaluate such processes from models, they are not particularly well-understood at low proton energies, and are therefore not included in the simulation. A detailed study of the potential effects of neglecting these quasi-free processes has been undertaken [38, 77]. For proton energies in the region of interest for the extraction of O_x and T, the absolute discrepancy between calculated values of A_{eff} with and without quasi-free scattering has been found to be 0.009. The systematic uncertainty arising from this effect has been estimated to be $\sigma^{syst}_{Aeff} = 5.6\%$. Adding the three separate errors gives an average total systematic uncertainty on O_x and T of $\sigma^{syst} = 13.2\%$. The uncertainty bars at the base of the plots on figure 6.10 show how these errors vary.

6.3 Conclusion

Measurements of the Σ, O_x and T polarisation observables on the $\gamma p \rightarrow \pi^0 p$ reaction have been performed at the MAMI A2 facility over the photon beam energy range $450 < E_\gamma < 650$ MeV and over a wide range of polar angles in the centre of mass system. The Σ measurement fills a significant gap at low photon energies in the world dataset, and greatly expands the kinematic coverage for this observable. The data obtained from the present measurement has good agreement with previous measurements from the GRAAL and Yerevan facilities, as well as broad agreement with other overlapping measurements, and generally support the SAID partial-wave analysis. Over the majority of the kinematic range, the measurement presented strongly agrees with the Bonn-Gatchina partial wave analysis. The data however has a relatively consistently poor agreement with the MAID isobar model. These data will be used to further constrain the parameters used in the three models, and greatly enhance the study of the Σ polarisation observable for the ongoing research into the complete measurement of polarisation observables.

The preliminary measurements of the O_x and T polarisation observables, although lacking the same degree of statistical accuracy of the Σ results, significantly expand on the world dataset in this energy regime. This is particularly true for the O_x result as the new results are in general agreement with previous results and model predictions. However, a dedicated measurement of the effective analysing power, as opposed to a parameterised simulation, would greatly enhance the significance of these and future measurements. This measurement itself is a proof of principle that large acceptance calorimeters can be used in the future for measurements involving recoil polarisation, as opposed to relying only on small acceptance magnetic spectrometers as has hitherto been the case.

The results presented in this thesis greatly expand the study of polarisation observables in the first resonance region, and enhance the ongoing search for a complete understanding of the nucleon's excitation spectrum. Furthermore, the results clearly demonstrate the potential impact of a new approach to performing simultaneous recoil polarimetry measurements over a wide kinematic range.

Appendix A

Tabulated Results

The results for Σ are tabulated in this appendix, showing the theta distributions in the centre of mass for each energy, as well as their associated statistical and systematic error.

$449 < E_\gamma < 454 MeV$			
$\theta_{CM} Range$	Σ	σ_{stat}	σ_{syst}
$50° < \theta_{CM} < 58°$	0.396	± 0.566	± 0.005
$58° < \theta_{CM} < 66°$	0.535	± 0.159	± 0.007
$66° < \theta_{CM} < 74°$	0.693	± 0.111	± 0.009
$74° < \theta_{CM} < 82°$	0.447	± 0.104	± 0.006
$82° < \theta_{CM} < 90°$	0.776	± 0.082	± 0.010
$90° < \theta_{CM} < 98°$	0.655	± 0.038	± 0.009
$98° < \theta_{CM} < 106°$	0.701	± 0.027	± 0.009
$106° < \theta_{CM} < 114°$	0.751	± 0.027	± 0.010
$114° < \theta_{CM} < 122°$	0.736	± 0.030	± 0.010
$122° < \theta_{CM} < 130°$	0.677	± 0.036	± 0.009
$130° < \theta_{CM} < 138°$	0.596	± 0.051	± 0.008
$138° < \theta_{CM} < 146°$	0.762	± 0.073	± 0.010
$146° < \theta_{CM} < 154°$	0.411	± 0.106	± 0.006
$454 < E_\gamma < 458 MeV$			
$\theta_{CM} Range$	Σ	σ_{stat}	σ_{syst}
$50° < \theta_{CM} < 58°$	0.591	± 0.443	± 0.008
$58° < \theta_{CM} < 66°$	0.839	± 0.139	± 0.012
$66° < \theta_{CM} < 74°$	0.441	± 0.103	± 0.006
$74° < \theta_{CM} < 82°$	0.634	± 0.094	± 0.009
$82° < \theta_{CM} < 90°$	0.757	± 0.066	± 0.011
$90° < \theta_{CM} < 98°$	0.678	± 0.031	± 0.010
$98° < \theta_{CM} < 106°$	0.686	± 0.024	± 0.010
$106° < \theta_{CM} < 114°$	0.719	± 0.025	± 0.010
$114° < \theta_{CM} < 122°$	0.718	± 0.028	± 0.010
$122° < \theta_{CM} < 130°$	0.753	± 0.033	± 0.011
$130° < \theta_{CM} < 138°$	0.708	± 0.046	± 0.010
$138° < \theta_{CM} < 146°$	0.719	± 0.066	± 0.010
$146° < \theta_{CM} < 154°$	0.752	± 0.096	± 0.011
$458 < E_\gamma < 462 MeV$			
$\theta_{CM} Range$	Σ	σ_{stat}	σ_{syst}
$50° < \theta_{CM} < 58°$	1.140	± 0.559	± 0.016
$58° < \theta_{CM} < 66°$	0.683	± 0.156	± 0.010
$66° < \theta_{CM} < 74°$	0.482	± 0.117	± 0.007
$74° < \theta_{CM} < 82°$	0.302	± 0.111	± 0.004
$82° < \theta_{CM} < 90°$	0.536	± 0.068	± 0.008
$90° < \theta_{CM} < 98°$	0.651	± 0.034	± 0.010
$98° < \theta_{CM} < 106°$	0.690	± 0.028	± 0.010
$106° < \theta_{CM} < 114°$	0.693	± 0.029	± 0.010
$114° < \theta_{CM} < 122°$	0.686	± 0.032	± 0.010
$122° < \theta_{CM} < 130°$	0.731	± 0.038	± 0.011
$130° < \theta_{CM} < 138°$	0.779	± 0.054	± 0.011
$138° < \theta_{CM} < 146°$	0.689	± 0.075	± 0.010
$146° < \theta_{CM} < 154°$	0.717	± 0.111	± 0.011

$462 < E_\gamma < 466 MeV$			
$\theta_{CM} Range$	Σ	σ_{stat}	σ_{syst}
$50° < \theta_{CM} < 58°$	0.724	± 0.311	± 0.011
$58° < \theta_{CM} < 66°$	0.383	± 0.124	± 0.006
$66° < \theta_{CM} < 74°$	0.311	± 0.094	± 0.005
$74° < \theta_{CM} < 82°$	0.340	± 0.087	± 0.005
$82° < \theta_{CM} < 90°$	0.678	± 0.048	± 0.010
$90° < \theta_{CM} < 98°$	0.720	± 0.026	± 0.011
$98° < \theta_{CM} < 106°$	0.702	± 0.022	± 0.011
$106° < \theta_{CM} < 114°$	0.694	± 0.024	± 0.011
$114° < \theta_{CM} < 122°$	0.748	± 0.026	± 0.011
$122° < \theta_{CM} < 130°$	0.704	± 0.031	± 0.011
$130° < \theta_{CM} < 138°$	0.664	± 0.043	± 0.010
$138° < \theta_{CM} < 146°$	0.809	± 0.060	± 0.012
$146° < \theta_{CM} < 154°$	0.954	± 0.088	± 0.015
$466 < E_\gamma < 471 MeV$			
$\theta_{CM} Range$	Σ	σ_{stat}	σ_{syst}
$50° < \theta_{CM} < 58°$	0.337	± 0.354	± 0.005
$58° < \theta_{CM} < 66°$	0.555	± 0.118	± 0.009
$66° < \theta_{CM} < 74°$	0.510	± 0.094	± 0.008
$74° < \theta_{CM} < 82°$	0.624	± 0.084	± 0.010
$82° < \theta_{CM} < 90°$	0.647	± 0.042	± 0.010
$90° < \theta_{CM} < 98°$	0.648	± 0.024	± 0.010
$98° < \theta_{CM} < 106°$	0.656	± 0.022	± 0.010
$106° < \theta_{CM} < 114°$	0.732	± 0.024	± 0.012
$114° < \theta_{CM} < 122°$	0.787	± 0.026	± 0.012
$122° < \theta_{CM} < 130°$	0.797	± 0.031	± 0.013
$130° < \theta_{CM} < 138°$	0.677	± 0.043	± 0.011
$138° < \theta_{CM} < 146°$	0.764	± 0.060	± 0.012
$146° < \theta_{CM} < 154°$	0.493	± 0.089	± 0.008
$471 < E_\gamma < 475 MeV$			
$\theta_{CM} Range$	Σ	σ_{stat}	σ_{syst}
$50° < \theta_{CM} < 58°$	0.763	± 0.343	± 0.012
$58° < \theta_{CM} < 66°$	0.544	± 0.150	± 0.009
$66° < \theta_{CM} < 74°$	0.400	± 0.120	± 0.007
$74° < \theta_{CM} < 82°$	0.353	± 0.107	± 0.006
$82° < \theta_{CM} < 90°$	0.550	± 0.049	± 0.009
$90° < \theta_{CM} < 98°$	0.596	± 0.030	± 0.010
$98° < \theta_{CM} < 106°$	0.652	± 0.029	± 0.011
$106° < \theta_{CM} < 114°$	0.719	± 0.030	± 0.012
$114° < \theta_{CM} < 122°$	0.632	± 0.033	± 0.010
$122° < \theta_{CM} < 130°$	0.678	± 0.039	± 0.011
$130° < \theta_{CM} < 138°$	0.784	± 0.054	± 0.013
$138° < \theta_{CM} < 146°$	0.606	± 0.074	± 0.010
$146° < \theta_{CM} < 154°$	0.422	± 0.111	± 0.007

$475 < E_\gamma < 479 MeV$			
$\theta_{CM} Range$	Σ	σ_{stat}	σ_{syst}
$50° < \theta_{CM} < 58°$	0.738	± 0.253	± 0.012
$58° < \theta_{CM} < 66°$	0.650	± 0.114	± 0.011
$66° < \theta_{CM} < 74°$	0.412	± 0.092	± 0.007
$74° < \theta_{CM} < 82°$	0.551	± 0.077	± 0.009
$82° < \theta_{CM} < 90°$	0.547	± 0.034	± 0.009
$90° < \theta_{CM} < 98°$	0.566	± 0.022	± 0.010
$98° < \theta_{CM} < 106°$	0.680	± 0.022	± 0.012
$106° < \theta_{CM} < 114°$	0.688	± 0.023	± 0.012
$114° < \theta_{CM} < 122°$	0.657	± 0.025	± 0.011
$122° < \theta_{CM} < 130°$	0.683	± 0.030	± 0.012
$130° < \theta_{CM} < 138°$	0.657	± 0.041	± 0.011
$138° < \theta_{CM} < 146°$	0.640	± 0.057	± 0.011
$146° < \theta_{CM} < 154°$	0.451	± 0.083	± 0.008
$479 < E_\gamma < 483 MeV$			
$\theta_{CM} Range$	Σ	σ_{stat}	σ_{syst}
$50° < \theta_{CM} < 58°$	0.359	± 0.237	± 0.006
$58° < \theta_{CM} < 66°$	0.484	± 0.110	± 0.009
$66° < \theta_{CM} < 74°$	0.472	± 0.088	± 0.008
$74° < \theta_{CM} < 82°$	0.597	± 0.070	± 0.011
$82° < \theta_{CM} < 90°$	0.669	± 0.031	± 0.012
$90° < \theta_{CM} < 98°$	0.629	± 0.021	± 0.011
$98° < \theta_{CM} < 106°$	0.657	± 0.021	± 0.012
$106° < \theta_{CM} < 114°$	0.682	± 0.022	± 0.012
$114° < \theta_{CM} < 122°$	0.657	± 0.025	± 0.012
$122° < \theta_{CM} < 130°$	0.773	± 0.029	± 0.014
$130° < \theta_{CM} < 138°$	0.654	± 0.040	± 0.012
$138° < \theta_{CM} < 146°$	0.705	± 0.055	± 0.013
$146° < \theta_{CM} < 154°$	0.777	± 0.081	± 0.014
$483 < E_\gamma < 488 MeV$			
$\theta_{CM} Range$	Σ	σ_{stat}	σ_{syst}
$50° < \theta_{CM} < 58°$	0.149	± 0.222	± 0.003
$58° < \theta_{CM} < 66°$	0.435	± 0.100	± 0.008
$66° < \theta_{CM} < 74°$	0.584	± 0.082	± 0.011
$74° < \theta_{CM} < 82°$	0.426	± 0.062	± 0.008
$82° < \theta_{CM} < 90°$	0.619	± 0.028	± 0.011
$90° < \theta_{CM} < 98°$	0.612	± 0.021	± 0.011
$98° < \theta_{CM} < 106°$	0.684	± 0.020	± 0.013
$106° < \theta_{CM} < 114°$	0.744	± 0.022	± 0.014
$114° < \theta_{CM} < 122°$	0.721	± 0.024	± 0.013
$122° < \theta_{CM} < 130°$	0.674	± 0.028	± 0.012
$130° < \theta_{CM} < 138°$	0.810	± 0.038	± 0.015
$138° < \theta_{CM} < 146°$	0.574	± 0.053	± 0.011
$146° < \theta_{CM} < 154°$	0.609	± 0.079	± 0.011

$488 < E_\gamma < 492 MeV$			
$\theta_{CM} Range$	Σ	σ_{stat}	σ_{syst}
$50° < \theta_{CM} < 58°$	0.411	± 0.198	± 0.008
$58° < \theta_{CM} < 66°$	0.453	± 0.100	± 0.009
$66° < \theta_{CM} < 74°$	0.549	± 0.082	± 0.010
$74° < \theta_{CM} < 82°$	0.523	± 0.055	± 0.010
$82° < \theta_{CM} < 90°$	0.568	± 0.026	± 0.011
$90° < \theta_{CM} < 98°$	0.630	± 0.020	± 0.012
$98° < \theta_{CM} < 106°$	0.656	± 0.020	± 0.013
$106° < \theta_{CM} < 114°$	0.645	± 0.021	± 0.012
$114° < \theta_{CM} < 122°$	0.752	± 0.023	± 0.014
$122° < \theta_{CM} < 130°$	0.743	± 0.028	± 0.014
$130° < \theta_{CM} < 138°$	0.664	± 0.038	± 0.013
$138° < \theta_{CM} < 146°$	0.702	± 0.051	± 0.013
$146° < \theta_{CM} < 154°$	0.740	± 0.076	± 0.014
$492 < E_\gamma < 496 MeV$			
$\theta_{CM} Range$	Σ	σ_{stat}	σ_{syst}
$50° < \theta_{CM} < 58°$	0.578	± 0.179	± 0.011
$58° < \theta_{CM} < 66°$	0.471	± 0.098	± 0.009
$66° < \theta_{CM} < 74°$	0.523	± 0.083	± 0.010
$74° < \theta_{CM} < 82°$	0.553	± 0.051	± 0.011
$82° < \theta_{CM} < 90°$	0.592	± 0.024	± 0.012
$90° < \theta_{CM} < 98°$	0.657	± 0.020	± 0.013
$98° < \theta_{CM} < 106°$	0.661	± 0.020	± 0.013
$106° < \theta_{CM} < 114°$	0.665	± 0.021	± 0.013
$114° < \theta_{CM} < 122°$	0.697	± 0.024	± 0.014
$122° < \theta_{CM} < 130°$	0.819	± 0.028	± 0.016
$130° < \theta_{CM} < 138°$	0.767	± 0.038	± 0.015
$138° < \theta_{CM} < 146°$	0.631	± 0.050	± 0.012
$146° < \theta_{CM} < 154°$	0.592	± 0.078	± 0.012
$496 < E_\gamma < 501 MeV$			
$\theta_{CM} Range$	Σ	σ_{stat}	σ_{syst}
$50° < \theta_{CM} < 58°$	0.605	± 0.182	± 0.012
$58° < \theta_{CM} < 66°$	0.460	± 0.095	± 0.009
$66° < \theta_{CM} < 74°$	0.636	± 0.083	± 0.013
$74° < \theta_{CM} < 82°$	0.603	± 0.045	± 0.012
$82° < \theta_{CM} < 90°$	0.565	± 0.023	± 0.012
$90° < \theta_{CM} < 98°$	0.596	± 0.020	± 0.012
$98° < \theta_{CM} < 106°$	0.670	± 0.020	± 0.014
$106° < \theta_{CM} < 114°$	0.672	± 0.021	± 0.014
$114° < \theta_{CM} < 122°$	0.696	± 0.023	± 0.014
$122° < \theta_{CM} < 130°$	0.765	± 0.028	± 0.016
$130° < \theta_{CM} < 138°$	0.774	± 0.037	± 0.016
$138° < \theta_{CM} < 146°$	0.695	± 0.050	± 0.014
$146° < \theta_{CM} < 154°$	0.652	± 0.076	± 0.013

$501 < E_\gamma < 505 MeV$			
$\theta_{CM} Range$	Σ	σ_{stat}	σ_{syst}
$50° < \theta_{CM} < 58°$	0.263	± 0.176	± 0.005
$58° < \theta_{CM} < 66°$	0.530	± 0.099	± 0.011
$66° < \theta_{CM} < 74°$	0.530	± 0.084	± 0.011
$74° < \theta_{CM} < 82°$	0.586	± 0.044	± 0.012
$82° < \theta_{CM} < 90°$	0.575	± 0.023	± 0.012
$90° < \theta_{CM} < 98°$	0.615	± 0.021	± 0.013
$98° < \theta_{CM} < 106°$	0.652	± 0.021	± 0.014
$106° < \theta_{CM} < 114°$	0.688	± 0.022	± 0.015
$114° < \theta_{CM} < 122°$	0.705	± 0.024	± 0.015
$122° < \theta_{CM} < 130°$	0.724	± 0.029	± 0.015
$130° < \theta_{CM} < 138°$	0.752	± 0.039	± 0.016
$138° < \theta_{CM} < 146°$	0.653	± 0.052	± 0.014
$146° < \theta_{CM} < 154°$	0.687	± 0.077	± 0.015
$505 < E_\gamma < 509 MeV$			
$\theta_{CM} Range$	Σ	σ_{stat}	σ_{syst}
$50° < \theta_{CM} < 58°$	0.794	± 0.175	± 0.017
$58° < \theta_{CM} < 66°$	0.605	± 0.095	± 0.013
$66° < \theta_{CM} < 74°$	0.442	± 0.081	± 0.010
$74° < \theta_{CM} < 82°$	0.549	± 0.039	± 0.012
$82° < \theta_{CM} < 90°$	0.597	± 0.022	± 0.013
$90° < \theta_{CM} < 98°$	0.629	± 0.020	± 0.014
$98° < \theta_{CM} < 106°$	0.675	± 0.020	± 0.015
$106° < \theta_{CM} < 114°$	0.692	± 0.021	± 0.015
$114° < \theta_{CM} < 122°$	0.715	± 0.024	± 0.016
$122° < \theta_{CM} < 130°$	0.741	± 0.028	± 0.016
$130° < \theta_{CM} < 138°$	0.698	± 0.037	± 0.015
$138° < \theta_{CM} < 146°$	0.753	± 0.049	± 0.016
$146° < \theta_{CM} < 154°$	0.795	± 0.076	± 0.017
$509 < E_\gamma < 513 MeV$			
$\theta_{CM} Range$	Σ	σ_{stat}	σ_{syst}
$50° < \theta_{CM} < 58°$	0.353	± 0.149	± 0.008
$58° < \theta_{CM} < 66°$	0.313	± 0.090	± 0.007
$66° < \theta_{CM} < 74°$	0.447	± 0.076	± 0.010
$74° < \theta_{CM} < 82°$	0.578	± 0.034	± 0.013
$82° < \theta_{CM} < 90°$	0.542	± 0.020	± 0.012
$90° < \theta_{CM} < 98°$	0.568	± 0.019	± 0.013
$98° < \theta_{CM} < 106°$	0.629	± 0.019	± 0.014
$106° < \theta_{CM} < 114°$	0.640	± 0.020	± 0.014
$114° < \theta_{CM} < 122°$	0.719	± 0.022	± 0.016
$122° < \theta_{CM} < 130°$	0.749	± 0.026	± 0.017
$130° < \theta_{CM} < 138°$	0.705	± 0.035	± 0.016
$138° < \theta_{CM} < 146°$	0.565	± 0.046	± 0.013
$146° < \theta_{CM} < 154°$	0.576	± 0.070	± 0.013

$513 < E_\gamma < 518 MeV$			
$\theta_{CM} Range$	Σ	σ_{stat}	σ_{syst}
$50° < \theta_{CM} < 58°$	0.493	± 0.143	± 0.011
$58° < \theta_{CM} < 66°$	0.531	± 0.084	± 0.012
$66° < \theta_{CM} < 74°$	0.473	± 0.069	± 0.011
$74° < \theta_{CM} < 82°$	0.490	± 0.031	± 0.011
$82° < \theta_{CM} < 90°$	0.579	± 0.019	± 0.013
$90° < \theta_{CM} < 98°$	0.638	± 0.018	± 0.015
$98° < \theta_{CM} < 106°$	0.637	± 0.018	± 0.015
$106° < \theta_{CM} < 114°$	0.689	± 0.020	± 0.016
$114° < \theta_{CM} < 122°$	0.702	± 0.022	± 0.016
$122° < \theta_{CM} < 130°$	0.739	± 0.026	± 0.017
$130° < \theta_{CM} < 138°$	0.647	± 0.034	± 0.015
$138° < \theta_{CM} < 146°$	0.683	± 0.045	± 0.016
$146° < \theta_{CM} < 154°$	0.661	± 0.069	± 0.015
$518 < E_\gamma < 522 MeV$			
$\theta_{CM} Range$	Σ	σ_{stat}	σ_{syst}
$50° < \theta_{CM} < 58°$	0.265	± 0.129	± 0.006
$58° < \theta_{CM} < 66°$	0.494	± 0.081	± 0.012
$66° < \theta_{CM} < 74°$	0.387	± 0.067	± 0.009
$74° < \theta_{CM} < 82°$	0.499	± 0.029	± 0.012
$82° < \theta_{CM} < 90°$	0.527	± 0.019	± 0.013
$90° < \theta_{CM} < 98°$	0.612	± 0.018	± 0.015
$98° < \theta_{CM} < 106°$	0.641	± 0.018	± 0.015
$106° < \theta_{CM} < 114°$	0.681	± 0.019	± 0.016
$114° < \theta_{CM} < 122°$	0.719	± 0.021	± 0.017
$122° < \theta_{CM} < 130°$	0.745	± 0.025	± 0.018
$130° < \theta_{CM} < 138°$	0.704	± 0.033	± 0.017
$138° < \theta_{CM} < 146°$	0.743	± 0.043	± 0.018
$146° < \theta_{CM} < 154°$	0.823	± 0.066	± 0.020
$522 < E_\gamma < 526 MeV$			
$\theta_{CM} Range$	Σ	σ_{stat}	σ_{syst}
$50° < \theta_{CM} < 58°$	0.485	± 0.131	± 0.012
$58° < \theta_{CM} < 66°$	0.294	± 0.080	± 0.007
$66° < \theta_{CM} < 74°$	0.409	± 0.062	± 0.010
$74° < \theta_{CM} < 82°$	0.580	± 0.027	± 0.014
$82° < \theta_{CM} < 90°$	0.583	± 0.019	± 0.014
$90° < \theta_{CM} < 98°$	0.621	± 0.018	± 0.015
$98° < \theta_{CM} < 106°$	0.654	± 0.018	± 0.016
$106° < \theta_{CM} < 114°$	0.702	± 0.019	± 0.017
$114° < \theta_{CM} < 122°$	0.723	± 0.021	± 0.018
$122° < \theta_{CM} < 130°$	0.751	± 0.025	± 0.018
$130° < \theta_{CM} < 138°$	0.736	± 0.033	± 0.018
$138° < \theta_{CM} < 146°$	0.700	± 0.043	± 0.017
$146° < \theta_{CM} < 154°$	0.617	± 0.066	± 0.015

$526 < E_\gamma < 530 MeV$			
$\theta_{CM} Range$	Σ	σ_{stat}	σ_{syst}
$50° < \theta_{CM} < 58°$	0.401	± 0.128	± 0.010
$58° < \theta_{CM} < 66°$	0.393	± 0.079	± 0.010
$66° < \theta_{CM} < 74°$	0.436	± 0.059	± 0.011
$74° < \theta_{CM} < 82°$	0.509	± 0.025	± 0.013
$82° < \theta_{CM} < 90°$	0.568	± 0.018	± 0.014
$90° < \theta_{CM} < 98°$	0.628	± 0.018	± 0.016
$98° < \theta_{CM} < 106°$	0.683	± 0.018	± 0.017
$106° < \theta_{CM} < 114°$	0.693	± 0.019	± 0.018
$114° < \theta_{CM} < 122°$	0.712	± 0.021	± 0.018
$122° < \theta_{CM} < 130°$	0.702	± 0.025	± 0.018
$130° < \theta_{CM} < 138°$	0.597	± 0.033	± 0.015
$138° < \theta_{CM} < 146°$	0.743	± 0.042	± 0.019
$146° < \theta_{CM} < 154°$	0.713	± 0.065	± 0.018
$530 < E_\gamma < 535 MeV$			
$\theta_{CM} Range$	Σ	σ_{stat}	σ_{syst}
$50° < \theta_{CM} < 58°$	0.322	± 0.118	± 0.008
$58° < \theta_{CM} < 66°$	0.355	± 0.079	± 0.009
$66° < \theta_{CM} < 74°$	0.442	± 0.056	± 0.011
$74° < \theta_{CM} < 82°$	0.504	± 0.024	± 0.013
$82° < \theta_{CM} < 90°$	0.558	± 0.018	± 0.014
$90° < \theta_{CM} < 98°$	0.598	± 0.017	± 0.016
$98° < \theta_{CM} < 106°$	0.652	± 0.018	± 0.017
$106° < \theta_{CM} < 114°$	0.640	± 0.019	± 0.017
$114° < \theta_{CM} < 122°$	0.680	± 0.020	± 0.018
$122° < \theta_{CM} < 130°$	0.737	± 0.024	± 0.019
$130° < \theta_{CM} < 138°$	0.760	± 0.032	± 0.020
$138° < \theta_{CM} < 146°$	0.764	± 0.041	± 0.020
$146° < \theta_{CM} < 154°$	0.811	± 0.062	± 0.021
$535 < E_\gamma < 539 MeV$			
$\theta_{CM} Range$	Σ	σ_{stat}	σ_{syst}
$50° < \theta_{CM} < 58°$	0.353	± 0.119	± 0.009
$58° < \theta_{CM} < 66°$	0.456	± 0.076	± 0.012
$66° < \theta_{CM} < 74°$	0.427	± 0.050	± 0.011
$74° < \theta_{CM} < 82°$	0.543	± 0.023	± 0.014
$82° < \theta_{CM} < 90°$	0.563	± 0.017	± 0.015
$90° < \theta_{CM} < 98°$	0.620	± 0.017	± 0.017
$98° < \theta_{CM} < 106°$	0.680	± 0.017	± 0.018
$106° < \theta_{CM} < 114°$	0.671	± 0.018	± 0.018
$114° < \theta_{CM} < 122°$	0.694	± 0.020	± 0.019
$122° < \theta_{CM} < 130°$	0.691	± 0.024	± 0.018
$130° < \theta_{CM} < 138°$	0.787	± 0.031	± 0.021
$138° < \theta_{CM} < 146°$	0.645	± 0.040	± 0.017
$146° < \theta_{CM} < 154°$	0.695	± 0.061	± 0.019

$539 < E_\gamma < 543 MeV$			
$\theta_{CM} Range$	Σ	σ_{stat}	σ_{syst}
$50° < \theta_{CM} < 58°$	0.259	± 0.115	± 0.007
$58° < \theta_{CM} < 66°$	0.522	± 0.076	± 0.014
$66° < \theta_{CM} < 74°$	0.581	± 0.046	± 0.016
$74° < \theta_{CM} < 82°$	0.570	± 0.021	± 0.016
$82° < \theta_{CM} < 90°$	0.588	± 0.017	± 0.016
$90° < \theta_{CM} < 98°$	0.589	± 0.016	± 0.016
$98° < \theta_{CM} < 106°$	0.656	± 0.017	± 0.018
$106° < \theta_{CM} < 114°$	0.698	± 0.018	± 0.019
$114° < \theta_{CM} < 122°$	0.721	± 0.019	± 0.020
$122° < \theta_{CM} < 130°$	0.739	± 0.023	± 0.020
$130° < \theta_{CM} < 138°$	0.804	± 0.030	± 0.022
$138° < \theta_{CM} < 146°$	0.774	± 0.038	± 0.021
$146° < \theta_{CM} < 154°$	0.534	± 0.059	± 0.015
$543 < E_\gamma < 547 MeV$			
$\theta_{CM} Range$	Σ	σ_{stat}	σ_{syst}
$50° < \theta_{CM} < 58°$	0.393	± 0.110	± 0.011
$58° < \theta_{CM} < 66°$	0.498	± 0.074	± 0.014
$66° < \theta_{CM} < 74°$	0.522	± 0.043	± 0.015
$74° < \theta_{CM} < 82°$	0.539	± 0.021	± 0.015
$82° < \theta_{CM} < 90°$	0.598	± 0.017	± 0.017
$90° < \theta_{CM} < 98°$	0.606	± 0.016	± 0.017
$98° < \theta_{CM} < 106°$	0.625	± 0.017	± 0.018
$106° < \theta_{CM} < 114°$	0.647	± 0.018	± 0.018
$114° < \theta_{CM} < 122°$	0.679	± 0.019	± 0.019
$122° < \theta_{CM} < 130°$	0.764	± 0.023	± 0.021
$130° < \theta_{CM} < 138°$	0.744	± 0.030	± 0.021
$138° < \theta_{CM} < 146°$	0.698	± 0.038	± 0.020
$146° < \theta_{CM} < 154°$	0.563	± 0.058	± 0.016
$547 < E_\gamma < 552 MeV$			
$\theta_{CM} Range$	Σ	σ_{stat}	σ_{syst}
$50° < \theta_{CM} < 58°$	0.440	± 0.111	± 0.012
$58° < \theta_{CM} < 66°$	0.443	± 0.075	± 0.013
$66° < \theta_{CM} < 74°$	0.547	± 0.041	± 0.016
$74° < \theta_{CM} < 82°$	0.554	± 0.020	± 0.016
$82° < \theta_{CM} < 90°$	0.592	± 0.017	± 0.017
$90° < \theta_{CM} < 98°$	0.591	± 0.017	± 0.017
$98° < \theta_{CM} < 106°$	0.628	± 0.017	± 0.018
$106° < \theta_{CM} < 114°$	0.626	± 0.018	± 0.018
$114° < \theta_{CM} < 122°$	0.701	± 0.020	± 0.020
$122° < \theta_{CM} < 130°$	0.706	± 0.024	± 0.020
$130° < \theta_{CM} < 138°$	0.706	± 0.031	± 0.020
$138° < \theta_{CM} < 146°$	0.696	± 0.038	± 0.020
$146° < \theta_{CM} < 154°$	0.703	± 0.058	± 0.020

$552 < E_\gamma < 556 MeV$			
$\theta_{CM} Range$	Σ	σ_{stat}	σ_{syst}
$50° < \theta_{CM} < 58°$	0.355	± 0.109	± 0.010
$58° < \theta_{CM} < 66°$	0.351	± 0.078	± 0.010
$66° < \theta_{CM} < 74°$	0.475	± 0.039	± 0.014
$74° < \theta_{CM} < 82°$	0.552	± 0.021	± 0.016
$82° < \theta_{CM} < 90°$	0.579	± 0.018	± 0.017
$90° < \theta_{CM} < 98°$	0.621	± 0.017	± 0.018
$98° < \theta_{CM} < 106°$	0.665	± 0.017	± 0.020
$106° < \theta_{CM} < 114°$	0.714	± 0.018	± 0.021
$114° < \theta_{CM} < 122°$	0.688	± 0.020	± 0.020
$122° < \theta_{CM} < 130°$	0.670	± 0.024	± 0.020
$130° < \theta_{CM} < 138°$	0.701	± 0.031	± 0.021
$138° < \theta_{CM} < 146°$	0.692	± 0.038	± 0.020
$146° < \theta_{CM} < 154°$	0.663	± 0.059	± 0.020
$556 < E_\gamma < 560 MeV$			
$\theta_{CM} Range$	Σ	σ_{stat}	σ_{syst}
$50° < \theta_{CM} < 58°$	0.267	± 0.099	± 0.008
$58° < \theta_{CM} < 66°$	0.461	± 0.070	± 0.014
$66° < \theta_{CM} < 74°$	0.478	± 0.034	± 0.014
$74° < \theta_{CM} < 82°$	0.553	± 0.019	± 0.017
$82° < \theta_{CM} < 90°$	0.585	± 0.016	± 0.018
$90° < \theta_{CM} < 98°$	0.618	± 0.016	± 0.019
$98° < \theta_{CM} < 106°$	0.663	± 0.016	± 0.020
$106° < \theta_{CM} < 114°$	0.657	± 0.017	± 0.020
$114° < \theta_{CM} < 122°$	0.722	± 0.019	± 0.022
$122° < \theta_{CM} < 130°$	0.698	± 0.022	± 0.021
$130° < \theta_{CM} < 138°$	0.617	± 0.029	± 0.019
$138° < \theta_{CM} < 146°$	0.672	± 0.036	± 0.020
$146° < \theta_{CM} < 154°$	0.587	± 0.053	± 0.018
$560 < E_\gamma < 564 MeV$			
$\theta_{CM} Range$	Σ	σ_{stat}	σ_{syst}
$50° < \theta_{CM} < 58°$	0.350	± 0.096	± 0.011
$58° < \theta_{CM} < 66°$	0.408	± 0.069	± 0.013
$66° < \theta_{CM} < 74°$	0.565	± 0.031	± 0.017
$74° < \theta_{CM} < 82°$	0.526	± 0.018	± 0.016
$82° < \theta_{CM} < 90°$	0.585	± 0.016	± 0.018
$90° < \theta_{CM} < 98°$	0.618	± 0.015	± 0.019
$98° < \theta_{CM} < 106°$	0.664	± 0.015	± 0.021
$106° < \theta_{CM} < 114°$	0.716	± 0.016	± 0.022
$114° < \theta_{CM} < 122°$	0.722	± 0.018	± 0.022
$122° < \theta_{CM} < 130°$	0.725	± 0.021	± 0.022
$130° < \theta_{CM} < 138°$	0.688	± 0.027	± 0.021
$138° < \theta_{CM} < 146°$	0.723	± 0.034	± 0.022
$146° < \theta_{CM} < 154°$	0.573	± 0.053	± 0.018

$564 < E_\gamma < 569 MeV$			
$\theta_{CM} Range$	Σ	σ_{stat}	σ_{syst}
$50° < \theta_{CM} < 58°$	0.183	± 0.097	± 0.006
$58° < \theta_{CM} < 66°$	0.334	± 0.068	± 0.011
$66° < \theta_{CM} < 74°$	0.512	± 0.029	± 0.016
$74° < \theta_{CM} < 82°$	0.544	± 0.017	± 0.017
$82° < \theta_{CM} < 90°$	0.602	± 0.015	± 0.019
$90° < \theta_{CM} < 98°$	0.638	± 0.015	± 0.020
$98° < \theta_{CM} < 106°$	0.680	± 0.015	± 0.022
$106° < \theta_{CM} < 114°$	0.700	± 0.016	± 0.022
$114° < \theta_{CM} < 122°$	0.708	± 0.018	± 0.022
$122° < \theta_{CM} < 130°$	0.720	± 0.021	± 0.023
$130° < \theta_{CM} < 138°$	0.737	± 0.027	± 0.023
$138° < \theta_{CM} < 146°$	0.705	± 0.033	± 0.022
$146° < \theta_{CM} < 154°$	0.687	± 0.051	± 0.022
$569 < E_\gamma < 573 MeV$			
$\theta_{CM} Range$	Σ	σ_{stat}	σ_{syst}
$50° < \theta_{CM} < 58°$	0.410	± 0.093	± 0.013
$58° < \theta_{CM} < 66°$	0.402	± 0.070	± 0.013
$66° < \theta_{CM} < 74°$	0.505	± 0.029	± 0.016
$74° < \theta_{CM} < 82°$	0.542	± 0.018	± 0.017
$82° < \theta_{CM} < 90°$	0.581	± 0.016	± 0.018
$90° < \theta_{CM} < 98°$	0.626	± 0.016	± 0.020
$98° < \theta_{CM} < 106°$	0.705	± 0.016	± 0.022
$106° < \theta_{CM} < 114°$	0.719	± 0.017	± 0.023
$114° < \theta_{CM} < 122°$	0.700	± 0.019	± 0.022
$122° < \theta_{CM} < 130°$	0.733	± 0.022	± 0.023
$130° < \theta_{CM} < 138°$	0.722	± 0.029	± 0.023
$138° < \theta_{CM} < 146°$	0.817	± 0.035	± 0.026
$146° < \theta_{CM} < 154°$	0.665	± 0.052	± 0.021
$573 < E_\gamma < 577 MeV$			
$\theta_{CM} Range$	Σ	σ_{stat}	σ_{syst}
$50° < \theta_{CM} < 58°$	0.447	± 0.097	± 0.014
$58° < \theta_{CM} < 66°$	0.463	± 0.067	± 0.015
$66° < \theta_{CM} < 74°$	0.592	± 0.028	± 0.019
$74° < \theta_{CM} < 82°$	0.563	± 0.018	± 0.018
$82° < \theta_{CM} < 90°$	0.599	± 0.016	± 0.019
$90° < \theta_{CM} < 98°$	0.656	± 0.016	± 0.021
$98° < \theta_{CM} < 106°$	0.680	± 0.016	± 0.022
$106° < \theta_{CM} < 114°$	0.697	± 0.017	± 0.022
$114° < \theta_{CM} < 122°$	0.722	± 0.018	± 0.023
$122° < \theta_{CM} < 130°$	0.732	± 0.022	± 0.024
$130° < \theta_{CM} < 138°$	0.652	± 0.028	± 0.021
$138° < \theta_{CM} < 146°$	0.642	± 0.035	± 0.021
$146° < \theta_{CM} < 154°$	0.551	± 0.052	± 0.018

$577 < E_\gamma < 582 MeV$			
$\theta_{CM} Range$	Σ	σ_{stat}	σ_{syst}
$50° < \theta_{CM} < 58°$	0.375	± 0.090	± 0.012
$58° < \theta_{CM} < 66°$	0.463	± 0.060	± 0.015
$66° < \theta_{CM} < 74°$	0.546	± 0.025	± 0.018
$74° < \theta_{CM} < 82°$	0.581	± 0.017	± 0.019
$82° < \theta_{CM} < 90°$	0.654	± 0.015	± 0.022
$90° < \theta_{CM} < 98°$	0.656	± 0.015	± 0.022
$98° < \theta_{CM} < 106°$	0.721	± 0.015	± 0.024
$106° < \theta_{CM} < 114°$	0.730	± 0.016	± 0.024
$114° < \theta_{CM} < 122°$	0.722	± 0.017	± 0.024
$122° < \theta_{CM} < 130°$	0.689	± 0.021	± 0.023
$130° < \theta_{CM} < 138°$	0.686	± 0.026	± 0.023
$138° < \theta_{CM} < 146°$	0.720	± 0.032	± 0.024
$146° < \theta_{CM} < 154°$	0.615	± 0.047	± 0.020
$582 < E_\gamma < 586 MeV$			
$\theta_{CM} Range$	Σ	σ_{stat}	σ_{syst}
$50° < \theta_{CM} < 58°$	0.405	± 0.090	± 0.013
$58° < \theta_{CM} < 66°$	0.352	± 0.059	± 0.012
$66° < \theta_{CM} < 74°$	0.583	± 0.024	± 0.019
$74° < \theta_{CM} < 82°$	0.571	± 0.017	± 0.019
$82° < \theta_{CM} < 90°$	0.629	± 0.016	± 0.021
$90° < \theta_{CM} < 98°$	0.670	± 0.015	± 0.022
$98° < \theta_{CM} < 106°$	0.679	± 0.015	± 0.022
$106° < \theta_{CM} < 114°$	0.763	± 0.016	± 0.025
$114° < \theta_{CM} < 122°$	0.709	± 0.018	± 0.023
$122° < \theta_{CM} < 130°$	0.736	± 0.021	± 0.024
$130° < \theta_{CM} < 138°$	0.747	± 0.026	± 0.025
$138° < \theta_{CM} < 146°$	0.689	± 0.032	± 0.023
$146° < \theta_{CM} < 154°$	0.423	± 0.049	± 0.014
$586 < E_\gamma < 590 MeV$			
$\theta_{CM} Range$	Σ	σ_{stat}	σ_{syst}
$50° < \theta_{CM} < 58°$	0.511	± 0.086	± 0.017
$58° < \theta_{CM} < 66°$	0.541	± 0.057	± 0.018
$66° < \theta_{CM} < 74°$	0.558	± 0.024	± 0.018
$74° < \theta_{CM} < 82°$	0.617	± 0.017	± 0.020
$82° < \theta_{CM} < 90°$	0.651	± 0.016	± 0.021
$90° < \theta_{CM} < 98°$	0.669	± 0.015	± 0.022
$98° < \theta_{CM} < 106°$	0.690	± 0.015	± 0.023
$106° < \theta_{CM} < 114°$	0.771	± 0.016	± 0.025
$114° < \theta_{CM} < 122°$	0.742	± 0.018	± 0.024
$122° < \theta_{CM} < 130°$	0.781	± 0.021	± 0.026
$130° < \theta_{CM} < 138°$	0.725	± 0.027	± 0.024
$138° < \theta_{CM} < 146°$	0.583	± 0.032	± 0.019
$146° < \theta_{CM} < 154°$	0.716	± 0.048	± 0.023

$590 < E_\gamma < 594 MeV$			
$\theta_{CM} Range$	Σ	σ_{stat}	σ_{syst}
$50° < \theta_{CM} < 58°$	0.465	± 0.084	± 0.015
$58° < \theta_{CM} < 66°$	0.451	± 0.054	± 0.015
$66° < \theta_{CM} < 74°$	0.543	± 0.023	± 0.018
$74° < \theta_{CM} < 82°$	0.552	± 0.017	± 0.019
$82° < \theta_{CM} < 90°$	0.642	± 0.015	± 0.022
$90° < \theta_{CM} < 98°$	0.678	± 0.015	± 0.023
$98° < \theta_{CM} < 106°$	0.697	± 0.015	± 0.024
$106° < \theta_{CM} < 114°$	0.728	± 0.015	± 0.025
$114° < \theta_{CM} < 122°$	0.772	± 0.017	± 0.026
$122° < \theta_{CM} < 130°$	0.708	± 0.020	± 0.024
$130° < \theta_{CM} < 138°$	0.733	± 0.026	± 0.025
$138° < \theta_{CM} < 146°$	0.681	± 0.032	± 0.023
$146° < \theta_{CM} < 154°$	0.554	± 0.046	± 0.019
$594 < E_\gamma < 599 MeV$			
$\theta_{CM} Range$	Σ	σ_{stat}	σ_{syst}
$50° < \theta_{CM} < 58°$	0.359	± 0.085	± 0.012
$58° < \theta_{CM} < 66°$	0.544	± 0.050	± 0.019
$66° < \theta_{CM} < 74°$	0.559	± 0.021	± 0.019
$74° < \theta_{CM} < 82°$	0.538	± 0.016	± 0.019
$82° < \theta_{CM} < 90°$	0.655	± 0.015	± 0.023
$90° < \theta_{CM} < 98°$	0.683	± 0.014	± 0.024
$98° < \theta_{CM} < 106°$	0.694	± 0.014	± 0.024
$106° < \theta_{CM} < 114°$	0.734	± 0.015	± 0.026
$114° < \theta_{CM} < 122°$	0.763	± 0.017	± 0.027
$122° < \theta_{CM} < 130°$	0.756	± 0.019	± 0.026
$130° < \theta_{CM} < 138°$	0.721	± 0.025	± 0.025
$138° < \theta_{CM} < 146°$	0.656	± 0.031	± 0.023
$146° < \theta_{CM} < 154°$	0.548	± 0.045	± 0.019
$599 < E_\gamma < 603 MeV$			
$\theta_{CM} Range$	Σ	σ_{stat}	σ_{syst}
$50° < \theta_{CM} < 58°$	0.446	± 0.079	± 0.016
$58° < \theta_{CM} < 66°$	0.488	± 0.047	± 0.017
$66° < \theta_{CM} < 74°$	0.558	± 0.021	± 0.020
$74° < \theta_{CM} < 82°$	0.594	± 0.016	± 0.021
$82° < \theta_{CM} < 90°$	0.685	± 0.015	± 0.024
$90° < \theta_{CM} < 98°$	0.714	± 0.014	± 0.025
$98° < \theta_{CM} < 106°$	0.747	± 0.014	± 0.026
$106° < \theta_{CM} < 114°$	0.767	± 0.015	± 0.027
$114° < \theta_{CM} < 122°$	0.745	± 0.017	± 0.026
$122° < \theta_{CM} < 130°$	0.752	± 0.019	± 0.027
$130° < \theta_{CM} < 138°$	0.712	± 0.024	± 0.025
$138° < \theta_{CM} < 146°$	0.566	± 0.030	± 0.020
$146° < \theta_{CM} < 154°$	0.500	± 0.044	± 0.018

$603 < E_\gamma < 607 MeV$			
$\theta_{CM} Range$	Σ	σ_{stat}	σ_{syst}
$50° < \theta_{CM} < 58°$	0.415	± 0.078	± 0.015
$58° < \theta_{CM} < 66°$	0.458	± 0.047	± 0.016
$66° < \theta_{CM} < 74°$	0.610	± 0.021	± 0.021
$74° < \theta_{CM} < 82°$	0.637	± 0.016	± 0.022
$82° < \theta_{CM} < 90°$	0.671	± 0.015	± 0.023
$90° < \theta_{CM} < 98°$	0.729	± 0.014	± 0.026
$98° < \theta_{CM} < 106°$	0.765	± 0.015	± 0.027
$106° < \theta_{CM} < 114°$	0.764	± 0.015	± 0.027
$114° < \theta_{CM} < 122°$	0.765	± 0.017	± 0.027
$122° < \theta_{CM} < 130°$	0.767	± 0.020	± 0.027
$130° < \theta_{CM} < 138°$	0.737	± 0.025	± 0.026
$138° < \theta_{CM} < 146°$	0.684	± 0.030	± 0.024
$146° < \theta_{CM} < 154°$	0.535	± 0.044	± 0.019
$607 < E_\gamma < 611 MeV$			
$\theta_{CM} Range$	Σ	σ_{stat}	σ_{syst}
$50° < \theta_{CM} < 58°$	0.502	± 0.082	± 0.018
$58° < \theta_{CM} < 66°$	0.506	± 0.044	± 0.018
$66° < \theta_{CM} < 74°$	0.542	± 0.021	± 0.019
$74° < \theta_{CM} < 82°$	0.627	± 0.016	± 0.022
$82° < \theta_{CM} < 90°$	0.677	± 0.015	± 0.024
$90° < \theta_{CM} < 98°$	0.685	± 0.014	± 0.024
$98° < \theta_{CM} < 106°$	0.710	± 0.015	± 0.025
$106° < \theta_{CM} < 114°$	0.718	± 0.015	± 0.026
$114° < \theta_{CM} < 122°$	0.753	± 0.017	± 0.027
$122° < \theta_{CM} < 130°$	0.734	± 0.020	± 0.026
$130° < \theta_{CM} < 138°$	0.748	± 0.025	± 0.027
$138° < \theta_{CM} < 146°$	0.654	± 0.030	± 0.023
$146° < \theta_{CM} < 154°$	0.483	± 0.043	± 0.017
$611 < E_\gamma < 615 MeV$			
$\theta_{CM} Range$	Σ	σ_{stat}	σ_{syst}
$50° < \theta_{CM} < 58°$	0.280	± 0.081	± 0.010
$58° < \theta_{CM} < 66°$	0.465	± 0.039	± 0.017
$66° < \theta_{CM} < 74°$	0.627	± 0.019	± 0.022
$74° < \theta_{CM} < 82°$	0.635	± 0.015	± 0.023
$82° < \theta_{CM} < 90°$	0.690	± 0.014	± 0.025
$90° < \theta_{CM} < 98°$	0.732	± 0.014	± 0.026
$98° < \theta_{CM} < 106°$	0.747	± 0.014	± 0.027
$106° < \theta_{CM} < 114°$	0.754	± 0.014	± 0.027
$114° < \theta_{CM} < 122°$	0.758	± 0.016	± 0.027
$122° < \theta_{CM} < 130°$	0.723	± 0.019	± 0.026
$130° < \theta_{CM} < 138°$	0.777	± 0.024	± 0.028
$138° < \theta_{CM} < 146°$	0.702	± 0.028	± 0.025
$146° < \theta_{CM} < 154°$	0.613	± 0.041	± 0.022

$615 < E_\gamma < 620 MeV$			
$\theta_{CM} Range$	Σ	σ_{stat}	σ_{syst}
$50° < \theta_{CM} < 58°$	0.308	± 0.075	± 0.011
$58° < \theta_{CM} < 66°$	0.576	± 0.040	± 0.020
$66° < \theta_{CM} < 74°$	0.600	± 0.020	± 0.021
$74° < \theta_{CM} < 82°$	0.644	± 0.016	± 0.023
$82° < \theta_{CM} < 90°$	0.724	± 0.015	± 0.025
$90° < \theta_{CM} < 98°$	0.758	± 0.014	± 0.027
$98° < \theta_{CM} < 106°$	0.786	± 0.014	± 0.028
$106° < \theta_{CM} < 114°$	0.781	± 0.015	± 0.027
$114° < \theta_{CM} < 122°$	0.775	± 0.017	± 0.027
$122° < \theta_{CM} < 130°$	0.744	± 0.020	± 0.026
$130° < \theta_{CM} < 138°$	0.770	± 0.025	± 0.027
$138° < \theta_{CM} < 146°$	0.674	± 0.030	± 0.024
$146° < \theta_{CM} < 154°$	0.526	± 0.043	± 0.018
$620 < E_\gamma < 624 MeV$			
$\theta_{CM} Range$	Σ	σ_{stat}	σ_{syst}
$50° < \theta_{CM} < 58°$	0.441	± 0.074	± 0.015
$58° < \theta_{CM} < 66°$	0.610	± 0.039	± 0.021
$66° < \theta_{CM} < 74°$	0.681	± 0.020	± 0.023
$74° < \theta_{CM} < 82°$	0.724	± 0.017	± 0.025
$82° < \theta_{CM} < 90°$	0.770	± 0.015	± 0.026
$90° < \theta_{CM} < 98°$	0.807	± 0.015	± 0.027
$98° < \theta_{CM} < 106°$	0.812	± 0.015	± 0.028
$106° < \theta_{CM} < 114°$	0.814	± 0.015	± 0.028
$114° < \theta_{CM} < 122°$	0.863	± 0.017	± 0.029
$122° < \theta_{CM} < 130°$	0.865	± 0.020	± 0.029
$130° < \theta_{CM} < 138°$	0.770	± 0.026	± 0.026
$138° < \theta_{CM} < 146°$	0.638	± 0.031	± 0.022
$146° < \theta_{CM} < 154°$	0.554	± 0.044	± 0.019
$624 < E_\gamma < 628 MeV$			
$\theta_{CM} Range$	Σ	σ_{stat}	σ_{syst}
$50° < \theta_{CM} < 58°$	0.507	± 0.079	± 0.017
$58° < \theta_{CM} < 66°$	0.288	± 0.019	± 0.020
$66° < \theta_{CM} < 74°$	0.340	± 0.010	± 0.023
$74° < \theta_{CM} < 82°$	0.360	± 0.008	± 0.025
$82° < \theta_{CM} < 90°$	0.370	± 0.008	± 0.026
$90° < \theta_{CM} < 98°$	0.392	± 0.007	± 0.027
$98° < \theta_{CM} < 106°$	0.395	± 0.007	± 0.027
$106° < \theta_{CM} < 114°$	0.391	± 0.008	± 0.027
$114° < \theta_{CM} < 122°$	0.402	± 0.009	± 0.028
$122° < \theta_{CM} < 130°$	0.407	± 0.010	± 0.028
$130° < \theta_{CM} < 138°$	0.375	± 0.013	± 0.026
$138° < \theta_{CM} < 146°$	0.327	± 0.015	± 0.023
$146° < \theta_{CM} < 154°$	0.246	± 0.022	± 0.017

Bibliography

[1] V.D. Burkert. *The European Physical Journal A-Hadrons and Nuclei*, 17(3):303–310, 2003.

[2] A.M. Sandorfi, S. Hoblit, H. Kamano, and T.S. Lee. *Journal of Physics G: Nuclear and Particle Physics*, 38:053001, 2011.

[3] S. Schadmand. In *Proceedings of the first workshop on quark-hadron duality and the transition to pQCD*, 2005.

[4] M.K. Gaillard, P.D. Grannis, and F.J. Sciulli. *Reviews of Modern Physics*, 71(2):96–111, 1999.

[5] M. Gell-Mann and Y. Ne'eman. *The Eightfold Way*. W.A. Benjamin New York, 1964.

[6] V.E. Barnes, P.L. Connolly, D.J. Crennell, et al. *Physical Review Letters*, 12(8):204–206, 1964.

[7] F.E. Close and G. Shaw. *Electromagnetic Interactions and Hadronic Structure*, volume 25. Cambridge Univ Pr, 2007.

[8] K.G. Wilson. *Physical Review D*, 10(8):2445, 1974.

[9] A.W. Thomas, W. Weise, and J. Wiley. *The Structure of the Nucleon*. Wiley Online Library, 2001.

[10] R.G. Edwards, J.J. Dudek, D.G. Richards, and S.J. Wallace. *Arxiv preprint arXiv:1104.5152*, 2011.

[11] S. Capstick and W. Roberts. *Progress in Particle and Nuclear Physics*, 45:S241–S331, 2000.

[12] W.M. Yao, C. Amsler, D. Asner, et al. *Journal of Physics G*, 33(1):164, 2006.

[13] M. Anselmino, E. Predazzi, S. Ekelin, S. Fredriksson, and DB Lichtenberg. *Reviews of Modern Physics*, 65(4):1199, 1993.

[14] C.P. Forsyth and R.E. Cutkosky. *Nuclear Physics B*, 178(1):35–44, 1981.

[15] V.A. Nikonov, A.V. Anisovich, E. Klempt, A.V. Sarantsev, and U. Thoma. *Physics Letters B*, 662(3):245–251, 2008.

[16] G.Y. Chen, S. Kamalov, S.N. Yang, D. Drechsel, and L. Tiator. *Nuclear Physics A*, 723(3-4):447–463, 2003.

[17] I.S. Barker, A. Donnachie, and J.K. Storrow. *Nuclear Physics B*, 95(2):347–356, 1975.

[18] D. Drechsel, O. Hanstein, SS Kamalov, and L. Tiator. *Nuclear Physics A*, 645(1):145–174, 1999.

[19] L. Tiator, D. Drechsel, S. Kamalov, et al. *The European Physical Journal A-Hadrons and Nuclei*, 19:55–60, 2004.

[20] R.A. Arndt, I.I. Strakovsky, and R.L. Workman. *International Journal of Modern Physics A*, 18(3):449–456, 2003.

[21] A.V. Anisovich, E. Klempt, V.A. Nikonov, et al. *The European Physical Journal A-Hadrons and Nuclei*, 44(2):203–220, 2010.

[22] M. Fuchs, J. Ahrens, G. Anton, et al. *Physics Letters B*, 368(1-2):20–25, 1996.

[23] J. Ahrens, S. Altieri, J. R. M. Annand, et al. *Physical Review Letters*, 88:232002, 2002. GDH and A2 Collaboration.

[24] J. Ahrens, S. Altieri, J. Annand, et al. *The European Physical Journal A - Hadrons and Nuclei*, 21:323–333, 2004.

[25] O. Bartalini, V. Bellini, J.P. Bocquet, et al. *The European Physical Journal A-Hadrons and Nuclei*, 26(3):399–419, 2005.

[26] O. Bartholomy, V. Credé, H. van Pee, et al. *Physical Review Letters*, 94(1):12003, 2005.

[27] H. van Pee, O. Bartholomy, V. Crede, et al. *The European Physical Journal A - Hadrons and Nuclei*, 31:61–77, 2007.

[28] M. Dugger, B. Ritchie, J.P. Ball, and P. Collins. *Physical Review C*, 76:025211, 2007.

[29] R. Beck, H. P. Krahn, J. Ahrens, et al. *Physical Review Letters*, 78:606–609, 1997.

[30] R. Beck. *The European Physical Journal A - Hadrons and Nuclei*, 28:173–183, 2006.

[31] D. Elsner, B. Bantes, O. Bartholomy, and D. Bayadilov. *The European Physical Journal A - Hadrons and Nuclei*, 39:373–381, 2009.

[32] N. Sparks, V. Crede, A. V. Anisovich, et al. *Physical Review C*, 81:065210, 2010.

[33] F.V. Adamian, A. Buniatian, G.S. Frangulian, et al. *Physical Review C*, 63:054606, 2001.

[34] D.J. Hamilton, V.H. Mamyan, K.A. Aniol, J.R.M. Annand, et al. *Physical Review Letters*, 94(24):242001, 2005.

[35] A.S. Bratashevskij, V.G. Gorbenko, A.I. Derebchinskij, et al. *Nuclear Physics B*, 166(3):525–533, 1980.

[36] R.O. Avakyan, O. Avakyan, A. Avetisyan, et al. *Soviet Journal of Nuclear Physics (English Translation: United States)*, 37(2), 1983.

[37] K. Wijesooriya, A. Afanasev, M. Amarian, et al. *Physical Review C*, 66:034614, 2002.

[38] M.H. Sikora. PhD thesis, University of Edinburgh, United Kingdom, 2011. Unpublished.

[39] A. Bock, G. Anton, W. Beulertz, et al. *Physical Review Letters*, 81:534–537, 1998.

[40] J. Alcorn, B.D. Anderson, K.A. Aniol, J.R.M. Annand, et al. *Nuclear Instruments and Methods in Physics Research Section A: Accelerators, Spectrometers, Detectors and Associated Equipment*, 522(3):294–346, 2004.

[41] W. Luo, E.J. Brash, and R. Gilman. *Arxiv Preprint arXiv:1109.4650v2*, 2011.

[42] S. Goertz, W. Meyer, and G. Reicherz. *Progress in Particle and Nuclear Physics*, 49(2):403–489, 2002.

[43] A. Jankowiak. *The European Physical Journal A*, 28(Supplement 1):1–1, 2006.

[44] Y.M. Tsipenyuk and S.P. Kapitza. *The Microtron: Development and Applications*. Taylor & Francis, 2002.

[45] K.H. Kaiser, K. Aulenbacher, O. Chubarov, et al. *Nuclear Instruments and Methods in Physics Research Section A: Accelerators, Spectrometers, Detectors and Associated Equipment*, 593(3):159–170, 2008.

[46] I. Anthony, J.D. Kellie, S.J. Hall, G.J. Miller, and J. Ahrens. *Nuclear Instruments and Methods in Physics Research Section A: Accelerators, Spectrometers, Detectors and Associated Equipment*, 301(2):230–240, 1991.

[47] B.R. Martin and G. Shaw. *Particle Physics*. Wiley, 2006.

[48] J.C. McGeorge, J.D. Kellie, J.R.M. Annand, J. Ahrens, I. Anthony, A. Clarkson, DJ Hamilton, PS Lumsden, EF McNicoll, RO Owens, et al. *The European Physical Journal A-Hadrons and Nuclei*, 37(1):129–137, 2008.

[49] S.J. Hall, G.J. Miller, R. Beck, and P. Jennewein. *Nuclear Instruments and Methods in Physics Research Section A: Accelerators, Spectrometers, Detectors and Associated Equipment*, 368(3):698–708, 1996.

[50] U. Timm. *Fortschritte der Physik*, 17(12):765–808, 1969.

[51] D. Lohmann, J. Peise, J. Ahrens, et al. *Nuclear Instruments and Methods in Physics Research Section A: Accelerators, Spectrometers, Detectors and Associated Equipment*, 343(2-3):494–507, 1994.

[52] H. Bilokon, G. Bologna, F. Celani, et al. *Nuclear Instruments and Methods in Physics Research*, 204(2-3):299–310, 1983.

[53] J.D. Kellie, P.J.M. Clive, G.L. Yang, et al. *Nuclear Instruments and Methods in Physics Research Section A: Accelerators, Spectrometers, Detectors and Associated Equipment*, 545(1-2):164–180, 2005.

[54] F.A. Natter, P. Grabmayr, T. Hehl, R. Owens, and S. Wunderlich. *Nuclear Instruments and Methods in Physics Research Section B: Beam Interactions with Materials and Atoms*, 211(4):465–486, 2003.

[55] H. Überall. *Physical Review*, 103(4):1055–1067, 1956.

[56] K. Livingston. *Nuclear Instruments and Methods in Physics Research Section A: Accelerators, Spectrometers, Detectors and Associated Equipment*, 603(3):205–213, 2009.

[57] F. Rambo, J. Ahrens, H.J. Arends, et al. *Physical Review C*, 58(1):489–501, 1998.

[58] S. Agostinelli, J. Allison, K. Amako, et al. *Nuclear Instruments and Methods in Physics Research-Section A Only*, 506(3):250–303, 2003.

[59] E.D. Bloom and C.W. Peck. *Annual Review of Nuclear and Particle Science*, 33(1):143–198, 1983.

[60] A. Starostin, B.M.K. Nefkens, E. Berger, et al. *Physical Review C*, 64(5):055205, 2001.

[61] M. Oreglia, E. Bloom, F. Bulos, et al. *Physical Review D*, 25(9):2259–2277, 1982.

[62] R. Novotny. *Nuclear Science, IEEE Transactions on*, 38(2):379–385, 2002.

[63] P. Drexler, U. Thoring, W. Bonn, et al. *Nuclear Science, IEEE Transactions on*, 50(4):969–973, 2003.

[64] J.R.M. Annand, 2005. http://www.nuclear.gla.ac.uk/∼acqusys/doc/AcquRoot.11.08.pdf.

[65] R. Brun and F. Rademakers. *Nuclear Instruments and Methods in Physics Research Section A: Accelerators, Spectrometers, Detectors and Associated Equipment*, 389(1-2):81–86, 1997.

[66] J. Brudvik. PhD thesis, University of California, UCLA, 2007. Unpublished.

[67] T. Jude. PhD thesis, University of Edinburgh, United Kingdom, 2010. Unpublished.

[68] H. Berghäuser. PhD thesis, Justus-Liebig-Universität, Gießen, 2010. Unpublished.

[69] K. Livingston. Technical report, University of Glasgow, 2011. http://www.nuclear.gla.ac.uk/∼kl/g8b/CbremJlab/makePolTablesLatest2.pdf.

[70] C.M. Tarbet. PhD thesis, University of Edinburgh, United Kingdom, 2007.

[71] J. Robinson. PhD thesis, University of Glasgow, United Kingdom, 2010. Unpublished.

[72] R.A. Adelseck and B. Saghai. *Physical Review C*, 42(1):108, 1990.

[73] R. Wilson. *The Nucleon-nucleon Interaction: Experimental and Phenomenological*. Interscience, 1963.

[74] R.B. Wiringa, R.A. Smith, and T.L. Ainsworth. *Physical Review C*, 29(4):1207, 1984.

[75] R.B. Wiringa, V.G.J. Stoks, and R. Schiavilla. *Physical Review C*, 51(1):38, 1995.

[76] K.S. Krane. *Introductory Nuclear Physics*. John Wiley and Sons Inc., New York, NY, 1987.

[77] M.H. Sikora. Private Comminication.

[78] G. Waters, I.M. Blair, G.A. Ludgate, et al. *Nuclear Instruments and Methods*, 153(2-3):401–408, 1978.

[79] E. Aprile-Giboni, R. Hausammann, E. Heer, et al. *Nuclear Instruments and Methods in Physics Research*, 215(1-2):147–157, 1983.

[80] J. Glister, G. Ron, B. Lee, et al. *Nuclear Instruments and Methods in Physics Research Section A: Accelerators, Spectrometers, Detectors and Associated Equipment*, 606(3):578–584, 2009.

[81] MW McNaughton, BE Bonner, H. Ohnuma, et al. *Nuclear Instruments and Methods in Physics Research Section A: Accelerators, Spectrometers, Detectors and Associated Equipment*, 241(2-3):435–440, 1985.

[82] A. Sarantsev. *Chinese Physics C*, 33:1085, 2009.

[83] A.A. Belyaev, V.A. Get'man, V.G. Gorbenko, et al. *Nuclear Physics B*, 213(2):201–222, 1983.

[84] R.A. Arndt, I.I. Strakovsky, and R.L. Workman. http://gwdac.phys.gwu.edu/.